ABSTRACT

Title of Dissertation: TURBULENCE AND SUPERFLUIDITY
IN THE ATOMIC BOSE-EINSTEIN CONDENSATE

Mingshu Zhao
Doctor of Philosophy, 2024

Dissertation Directed by: Professor Ian Spielman
Joint Quantum Institute,
National Institute of Standards and Technology,
and Department of Physics, University of Maryland College Park

In this dissertation I investigate turbulence in atomic Bose-Einstein condensates (BECs), focusing on the challenge of quantifying velocity field measurements in quantum fluids. Turbulence, a universal phenomenon observed across various scales and mediums – from classical systems like Earth's oceans and atmosphere to quantum fluids including neutron stars, superfluid helium, and atomic BECs – exhibits complex fluid motion patterns spanning a wide range of length scales. While classical turbulence has been extensively studied, quantum systems present many open questions, particularly regarding the existence of an inertial scale and the applicability of Kolmogorov scaling laws.

I introduce a novel velocimetry technique, analogous to particle image velocimetry (PIV), using spinor impurities as tracer particles. This method enables the direct measurement of the velocity field and thereby the velocity structure functions (VSFs) in turbulent atomic BECs. The technique overcomes limitations of existing experimental approaches that rely on time of

flight (TOF) measurements, offering a clearer connection to VSFs and enabling a more direct comparison of turbulence in atomic gases with other fluids.

The cold-atom PIV technique enables directly measuring the velocity field, leading to a detailed analysis of both VSFs and the velocity increment probability density functions (VI-PDF). Key findings include the observation of superfluid turbulence conforming to Kolmogorov theory from VSFs, and intermittency from high order of VSFs and the non-Gaussian fat tail in the VI-PDF.

TURBULENCE AND SUPERFLUIDITY IN THE ATOMIC BOSE-EINSTEIN CONDENSATE

by

Mingshu Zhao

Dissertation submitted to the Faculty of the Graduate School of the
University of Maryland, College Park in partial fulfillment
of the requirements for the degree of
Doctor of Philosophy
2024

Advisory Committee:
Professor Daniel Lathrop, Chair
Professor Ian Spielman, Advisor
Professor Nathan Schine
Professor Thomas Antonsen
Professor Johan Larsson

Preface

In this thesis, I aim to present a comprehensive and accessible exploration of turbulence in atomic gases, particularly through the lens of cold atom Particle Image Velocimetry (PIV).

The inception of this technique came from an unlikely source: a longstanding issue with the bipolar current servo used for magnetic field control in our lab. This defect, when combined with high-power radiofrequency (RF) signals, led to an uncontrolled DC offset, impacting the lab's RF controls. My advisor, Ian, once suggested using two-tone copropagating Raman beams as an RF alternative, which, while effective, was not widely adopted.

The breakthrough came when I considered the use of a spatial light modulator (SLM) to control the spatial pattern of the Raman beam. This would allow for spatially-dependent RF coupling and, consequently, spatially-dependent spinor transfers. This concept paralleled the principles of Particle Imaging Velocimetry (PIV) in classical fluids, with spatially-dependent spinor transfers acting as tracer particles.

I am hopeful that this innovative technique will reinvigorate interest in hydrodynamic studies within the experimental physics community. By enabling direct measurements of velocity fields in cold atom experiments, we open new doors to understanding and exploring the rich dynamics of quantum fluids.

Acknowledgments

I want to start by thanking my advisor, Ian Spielman, for his support and encouragement, especially when I was exploring the idea of measuring velocity fields, even though it was a tough challenge.

A big thanks goes to Alessandro Restelli for helping me build the servo and all the other electronic parts we needed. My lab mate, Junheng Tao, deserves a special mention for all the hard work in setting up our lab and making our equipment work better.

I'm also grateful to Dimitris Trypogeorgos, Ana Valdés Curiel, and Qiyu Liang for showing me how to use the RbLi apparatus. Ana was really helpful with fixing our coils and getting our optics and lasers right. Qiyu helped a lot with our microscope system and inspired us with her drive. Thanks to Francisco Salces Cárcoba and Chris Billington for designing our new setup and teaching us about baking the system.

I want to acknowledge my friends from other labs in the PSC basement - Peter Elgee, Ananya Sitaram, Yanda Geng, Shouvik Mukherjee, Hector Sosa Martínez, Monica Gutierrez Galan, Swarnav Banik, Madison Anderson, Sarthak Subhankar, Tsz-Chun Tsui, Kevin Weber, Patrick Banner, Deniz Kurdak, Yaxin Li and James Maslek - for lending me equipment and giving advice whenever I was stuck.

A shoutout to the folks from NIST - Graham Reid, Alina Pineiro, Amilson Fritsch, Mingwu Lu and Emmanuel Mercdo, Emine Altuntas, Shangjie Guo, Yuchen Yue, Micheal Doris, Dario

D'Amato, João Braz and Davis Garwood - for their helpful advice in our group meetings.

Mental health is really important, so I'm incredibly thankful for my friends Zhiyu Yin, Yihang Wang, Shuyang Wang, Xiangyu Li, Yalun Yu, Wance Wang, Haonan Xiong, Tianyu Li, Ziyue Zou, Gong Cheng, Yixu Wang, Jingnan Cai, Haoying Dai, Haining Pan and Kaixin Huang and others for being there for me.

And lastly, none of this would have been possible without the support from my family.

Table of Contents

List of Tables

List of Figures

List of Abbreviations

BEC	Bose-Einstein condensate
VSF	Velocity Structure Function
PIV	Particle Image Velocimetry
VI	Velocity Increments
PDF	Probability Density Function
ARP	Adiabatic Rapid Passage
AC	Alternating Current
DC	Direct Current
RF	Radio Frequency
RWA	Rotating Wave Approximation
OD	Optical Depth
ToF	Time of Flight
GPE	Gross–Pitaevskii Equation
BdG	Bogoliubov-de-Gennes
MOT	Magneto-Optical Trap
PGC	Polarization Gradient Cooling
AOM	Acousto-optic Modulator
TTL	Transistor-Transistor Logic
Re	Reynolds Number
RANS	Reynolds-averaged Navier-Stokes Equations
LHS	Left hand side
RHS	Right hand side
LIA	Local Induction Approximation
LDV	Laser Doppler Velocimetry
UHV	Ultrahigh Vacuum
TEC	Thermoelectric Cooler
UV	Ultraviolet
CMOT	Compressed Magneto-Optical Trap
SatAbs	Saturated Absorption
FM	Frequency modulation
DDS	Direct Digital Synthesis
PLL	Phase Lock Loop
UMD	University of Maryland
MOSFET	Metal-Oxide-Semiconductor Field Effect Transistor
NMOS	N-Channel MOSFET
PMOS	P-Channel MOSFET
DMD	Digital Micromirror Device
LED	Light-emitting Diode
EM	Electromagnetic

PBS	Polarizing Beam Splitter
PTAI	Partial Transfer Absorption Imaging
NA	Numerical Aperture
K41	Kolmogorov 1941
K62	Kolmogorov 1962
COM	Center of Mass
ROI	Region of Interest
QP	Quadratic Programming
JB	Jarque-Bera
SF	Superfluid
UC	Unit Cell

Chapter 1: Introduction

Bose-Einstein condensates (BECs) represent one of the most intriguing states of matter in quantum physics. First predicted by Satyendra Nath Bose and Albert Einstein in the early twentieth century, BECs are formed when particles known as bosons are cooled to temperatures near absolute zero. Under these extreme conditions, a significant fraction of the bosons occupy the lowest quantum state, leading to the emergence of quantum phenomena on a macroscopic scale. This unique state of matter provides an unparalleled platform for exploring a range of quantum phenomena.

One of the most fascinating aspects of BECs is their behavior as quantum fluids. Unlike classical fluids, where the flow is governed by the Newtonian mechanics, quantum fluids exhibit collective behavior governed by quantum mechanics. The particles in a BEC act coherently, displaying properties such as superfluidity, a flow with zero viscosity, and quantized vortices. These characteristics make BECs an ideal system for studying fluid dynamics in a regime where classical intuition that circulation of a vortex can vary continuously gives way to quantum behavior. Despite the extensive research on BECs, the study of turbulence within these quantum fluids remains relatively unexplored territory.

Turbulence is a fundamental phenomenon encountered in a wide range of fluids and at all scales: from classical systems such as the earth's oceans and atmosphere [4, 5]; confined and solar

plasmas [6, 7]; and the self-gravitating media of the large-scale universe [8] to quantum fluids such as neutron stars [9], superfluid ^{4}He [10] and atomic Bose-Einstein condensates (BECs) [11, 12]. All of these are characterized by complex patterns of fluid motion that span a wide range of length scales. While the understanding of classical turbulence has matured in the past century [13], that of quantum systems has many open questions [14]. For example, in BECs does there exist a range of length scales—often termed the inertial scale—in which kinetic energy cascades from large to small scale in accordance with a Kolmogorov scaling law? Although this scaling was predicted only for incompressible fluids, it has been observed in virtually all turbulent fluids [13]. Kolmogorov scaling is generally quantified in terms of velocity structure functions (VSFs) that require knowledge of the fluid velocity field, which is difficult to measure in quantum gas experiments. In this dissertation I present a velocimetry technique, analogous to particle image velocimetry (PIV) [15, 16] employing spinor impurities as tracer particles, and thereby obtain VSFs in turbulent atomic BECs in agreement with the Kolmogorov scaling.

Existing experimental evidence for turbulence in atomic BECs relies on time-of-flight (TOF) measurements that have contributions from interaction-driven expansion [11] and the momentum distribution [17]. This has no clear connection to VSFs, where the order-p VSF is defined as $S_p(l) = \langle |\delta v_{\mathbf{l}}(\mathbf{x})|^p \rangle$ as a function of displacement $\mathbf{l}$ which describes the typical change in velocity

$$\delta v_{\mathbf{l}}(\mathbf{x}) = [\mathbf{v}(\mathbf{x}+\mathbf{l}) - \mathbf{v}(\mathbf{x})] \cdot \mathbf{e}_l \tag{1.1}$$

along the direction of the displacement $\mathbf{e}_l$ [1]. Without access to the VSF, the turbulence in

[1] The average $\langle \cdots \rangle$ is the ensemble (and ergodic for classical fluids) average over all positions $\mathbf{x}$ and displacement directions $\mathbf{e}_l$. Since the longitudinal and transverse VSFs are expected to be equal in isotropic systems such as ours,

atomic gases lacks a direct point of comparison with other fluids.

Unlike classical fluid flow, superfluid flow is strictly irrotational with a velocity field governed by the phase of the superfluid order parameter ϕ via $\mathbf{v} = \hbar\boldsymbol{\nabla}\phi/m$. Despite this, it is generally believed that superfluid turbulence obeys the same scaling $S_p(l) \propto l^{(p/3)}$ as classical fluids, described by the initial K41 Kolmogorov theory [18, 19, 20]; in the case of ^{4}He this has been experimentally verified [21, 22] for $p \leq 3$. The more complete K62 theory [23] adds an intermittency exponent that becomes important for large p and also predicts that the ensemble probability density function of velocity increments (VI-PDF) is non-Gaussian, with "fat-tails." Power-law scaling behavior and the energy cascade have been observed in the momentum distribution of homogeneously trapped BECs undergoing relaxation [12]; while this was interpreted in the context of Kolmogorov-type scaling for order $p = 2$, the observed exponent departed from the prediction of K41 theory and was instead interpreted using a wave turbulence model.

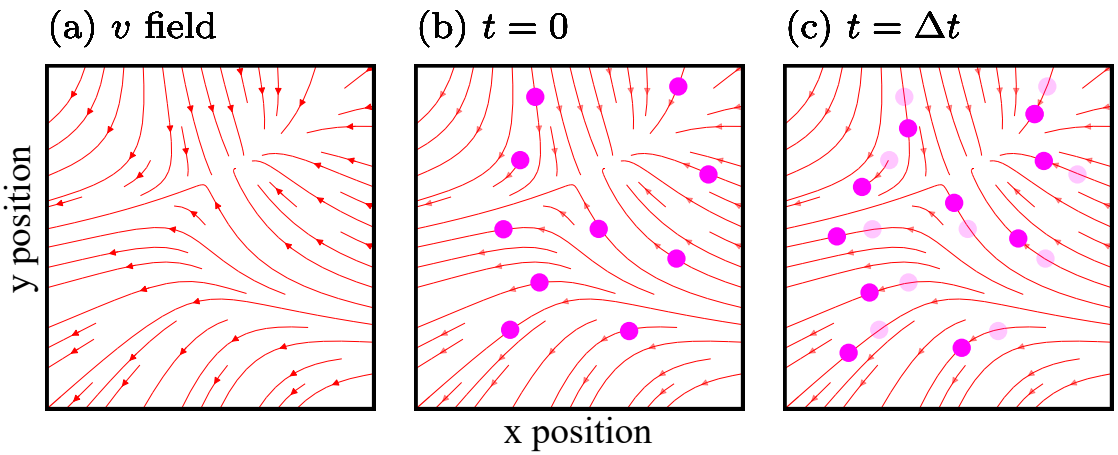

Figure 1.1: (a) An example of velocity field. (b) Tracer particles (bright pink) are injected into the system at $t = 0$. (c) At $t = \Delta t$, tracer particles (bright pink) move from their initial position (dark pink).

The cold-atom PIV technique, developed in our group, schematically illustrated in Fig. 1.1(a)-

we focus our exposition on the longitudinal VSF.

(c), enables directly measuring the velocity field and thereby both $S_p(l)$ and the VI-PDF. In this technique we prepare an initial velocity distribution [representative depiction in Fig. 1.1(a)], then create localized "tracer particles" consisting of atoms in a different hyperfine state using a spatially resolved technique [Fig. 1.1(b)], and, after a Δt delay, measure the displacement of the tracers [Fig. 1.1(c)]. This then leads directly to the local fluid velocity. The detail of this technique is introduced in the Chap. 5.

1.1 Thesis overview

This thesis covers three broad topic areas: the first is background, including topics from atomic physics that form the basis for our experimental techniques and turbulence theory that is related to the science studied in the context. The second area is technical details, including some details of our experimental apparatus, as well as how we use it to implement the cold atom PIV technique. The final category is scientific results, including our measurement of VSFs from VI which agrees well for low order of VSFs and intermittency is observed from high order of VSFs and scale-dependent VI-PDF in a turbulent condensate.

Chapter 2 introduces important tools from atomic physics, including the light matter interactions in which the tensor light shift is discussed in detail since it is directly related to the way we generate the tracer particles in the system. I also discuss the laser cooling and evaporative cooling techniques we apply to produce BEC in the lab.

Chapter 3 introduces the basic theory of classical and quantum turbulence, including the Kolmogorov theory in classical incompressible turbulence, and classical compressible turbulence using coarse graining, and finally the theoretical models and key experimental findings of quantum

turbulence. Velocimetry techniques are also discussed in this chapter. For readers who are only interested in the atomic physics, this chapter can be skipped.

Chapter 4 describes the apparatus for producing $^{87}\mathrm{Rb}$ BEC, including the vacuum system, magnetic field control, and optical control. Readers who are not interested in experimental details can skip this chapter.

Chapter 5 presents the implementation of cold-atom PIV in velocity field measurement. Benchmark examples include dipole mode and scissors mode in the harmonic trap and the quadrupular irrotational flow field in a rotating harmonic trap.

Chapter 6 introduces the application of the cold-atom PIV in a turbulent condensate. The velocity structure function is measured and agreed well with the Kolmogorov scaling. The intermittency is also observed from the fat tail of the velocity increments probability distribution function. Numerical simulation from a dissipation Gross Pitaevskii equation is also discussed.

Chapter 7 introduces a strange behavior in superfluid hydrodynamics, in which by imprinting anisotropic spatial-dependent potential, the superfluid density becomes a tensor related to the speed of sound. The theory and experimental details are discussed.

Chapter 2: Atom Light Interaction and Bose-Einstein Condensate

In this chapter, I will discuss the basic light atom interaction formalism used in the ultracold gas community, from two-level atoms to the coherent transfers, in which the light shift is discussed in detail. Then we discuss its application of laser cooling and evaporative cooling. The realization in the lab is introduced in Chap. 4. Please note that the ultracold gas is considered as a single particle in the first four sections of this chapter, which means that the scattering between atoms is neglected. In the last section, we will add the interaction when we discuss the Bose-Einstein condensate.

2.1 Two-level systems

A two-level atom is the simplest configuration for quantum mechanics, where the Hamiltonian can be expressed by

$$H_{\text{atom}} = \hbar\omega|e\rangle\langle e|. \tag{2.1}$$

Here, the energy of the ground state $|g\rangle$ is set to 0 for simplicity, and the energy difference between the excited state $|e\rangle$ and the ground state $|g\rangle$ is $\hbar\omega$. Now we introduce the light to the system. In a semi-classical picture, the light can be expressed by its electrical field.

$$\mathbf{E}(\mathbf{r},t) = \boldsymbol{\epsilon}(\mathbf{r},t)\exp\left(i\nu t - i\mathbf{k}\cdot\mathbf{r}\right) + \text{C.C}, \tag{2.2}$$

where $\boldsymbol{\epsilon}$ is a slowly varing amplitude compared to the spatial frequency $\mathbf{k}$, and $\mathrm{C.C}$ is the complex conjugate. In atomic physics, under dipole approximation, we write the atom-light interaction as a perturbative term $-\boldsymbol{d} \cdot \mathbf{E}(\mathbf{r} = \mathbf{r_0}, \mathbf{t})$, where $\boldsymbol{d} = q_e \mathbf{r}$ is the dipole moment of the atom with charge q_e, and $\mathbf{r_0}$ is the position of the atom. A rigorous derivation can be obtained from the Hamiltonian of an electron with charge q_e and mass m moving in an electromagnetic (EM) field.

$$H = \frac{1}{2m}[\mathbf{p_e} - q_e \mathbf{A}(\mathbf{r}, t)]^2 + q_e \phi(\mathbf{r}, t) + V(\mathbf{r}, t) - \boldsymbol{\mu} \cdot \mathbf{B}(\mathbf{r}, \mathbf{t}), \tag{2.3}$$

where $\mathbf{A}$ and ϕ are the vector and scalar potential of the EM field, $\mathbf{B}$ is the magnetic field, $\boldsymbol{\mu}$ is the magnetic dipole moment, and V is the core Coulomb potential. Using the Coulomb gauge, that is, $\nabla \cdot \mathbf{A} = 0$; $\phi = 0$, the vector potential satisfies the wave equation and can be decomposed as $\mathbf{A}(\mathbf{r}, t) = \mathbf{A}(t) \exp(i\mathbf{k} \cdot \mathbf{r})$. Expand the vector potential around the position of the atom $\mathbf{r_0}$,

$$\mathbf{A} = \mathbf{A}(t) e^{i\mathbf{k} \cdot \mathbf{r}_0}[1 + i\mathbf{k} \cdot \delta\mathbf{r}]. \tag{2.4}$$

Under the dipole approximation $\mathbf{k} \cdot \delta\mathbf{r} \ll 1$, the vector potential becomes spatially independent, that is, $\mathbf{A} \approx \mathbf{A}(t) e^{i\mathbf{k} \cdot \mathbf{r}_0}$. Since the position dependence of $\mathbf{A}$ is gone, thereby $\mathbf{A}$ commutes to $\mathbf{p_e}$. So we basically treat the EM field as a classical field and the Hamiltonian becomes the following.

$$H = \frac{1}{2m}[\mathbf{p_e}^2 - 2q_e \mathbf{p_e} \cdot \mathbf{A} + q_e^2 \mathbf{A}^2] + V - \boldsymbol{\mu} \cdot \mathbf{B}. \tag{2.5}$$

The vector potential coupled to the momentum can be transferred away by a unitary transformation

$$|\psi'\rangle = R|\psi\rangle = \exp[-iq_e \frac{\mathbf{r} \cdot \mathbf{A}(t)}{\hbar}]|\psi\rangle, \tag{2.6}$$

and the Hamiltonian becomes

$$H' = RHR^\dagger + i\hbar\frac{\partial R}{\partial t}R^\dagger = \frac{\mathbf{p_e}^2}{2m} + i\hbar(\frac{-iq_e\mathbf{r}}{\hbar}\cdot\frac{\partial \mathbf{A}}{\partial t}) + V(\mathbf{r}) - \boldsymbol{\mu}\cdot\mathbf{B}, \tag{2.7}$$

where $R\mathbf{p_e}R^\dagger = \mathbf{p_e} + q_e\mathbf{A}$ is used. The second term on the right-hand side (RHS) is exactly the interaction term $H_{int} = -\boldsymbol{d}\cdot\mathbf{E}(\mathbf{r}_0, t)$. So, we can decompose the Hamiltonian into two terms.

$$H_{\text{atom}} = \frac{\mathbf{p_e}^2}{2m} + V(\mathbf{r}), \qquad H_{int} = -\boldsymbol{d}\cdot\mathbf{E}(\mathbf{r}_0, t) - \boldsymbol{\mu}\cdot\mathbf{B}(\mathbf{r}_0, t) \tag{2.8}$$

The atom-light interaction consists of the electrical dipole interaction $\mathbf{d}\cdot\mathbf{E}(\mathbf{r}_0, t)$ and the magnetic dipole interaction $-\boldsymbol{\mu}\cdot\mathbf{B}(\mathbf{r}_0, t)$. Electric dipole transitions only have a non-vanishing matrix element between quantum states with different parity. Magnetic dipole transitions in contrast couple states with the same parity. The response of the magnetic dipole transition is much weaker than that of electric dipole transitions, so normally we consider only the electric dipole interaction unless it is forbidden by selection rules.

2.2 Coherent transfer between two levels

Rabi oscillations [24] and adiabatic rapid passage (ARP) [25] are two frequently used methods for transferring atoms between different states. In this section, the rotating wave approximation (RWA) [26] is applied to obtain an effective Hamiltonian without a fast oscillation in the optical frequency, from which we discuss Rabi flopping and ARP.

2.2.1 Rotating Wave Approximation

For a two-level atom, the electric dipole moment $\boldsymbol{d}$ can be decomposed under the eigenbasis of H_{atom}

$$\boldsymbol{d} = \mathbf{d_{ge}}|g\rangle\langle e| + \mathbf{d_{eg}}|e\rangle\langle g|, \tag{2.9}$$

where for spherical symmetric atoms $d_{gg} = d_{ee} = 0$. Under the dipole approximation $\mathbf{E}(t) = \boldsymbol{\epsilon}(t)e^{-i\nu t} + \text{C.C}$. So, the Hamiltonian becomes

$$H = \hbar\omega|e\rangle\langle e| - (\mathbf{d_{ge}}|g\rangle\langle e| + \mathbf{d_{eg}}|e\rangle\langle g|) \cdot (\boldsymbol{\epsilon}(t)e^{-i\nu t} + \boldsymbol{\epsilon}^*(t)e^{i\nu t}). \tag{2.10}$$

To obtain an effective Hamiltonian without the fast oscillating frequency ν, we go to the rotating frame by applying $U = |g\rangle\langle g| + e^{-i\nu t}|e\rangle\langle e|$. The effective Hamiltonian then becomes

$$H_{eff} = U^\dagger H U - i\hbar(\frac{d}{dt}U)U^\dagger = \hbar(\omega - \nu)|e\rangle\langle e| + \mathbf{d_{eg}} \cdot \boldsymbol{\epsilon}(t)|e\rangle\langle g| + \mathbf{d_{ge}} \cdot \boldsymbol{\epsilon}^*(t)|g\rangle\langle e|, \tag{2.11}$$

where the fast oscillation with frequency 2ν is ignored under RWA.

2.2.2 Rabi Oscillation and Adiabatic Rapid Passage

When the excitation is on resonance ($\nu = \omega$), and the atom is initially on the ground state, the atom population will oscillate between the ground and excites states by $\cos^2\frac{\Omega t}{2}$, where $\Omega = 2\frac{\mathbf{d_{eg}}\cdot\boldsymbol{\epsilon}}{\hbar}$ is the Rabi frequency. Introducing the detuning $\delta = \omega - \nu$, the effective Hamiltonian

is

$$H_{eff} = \hbar \begin{bmatrix} 0 & -\frac{\Omega^*}{2} \\ -\frac{\Omega}{2} & \delta \end{bmatrix}. \tag{2.12}$$

with eigenenergies $\epsilon_\pm = \frac{\hbar\delta}{2} \mp \frac{\hbar}{2}\sqrt{|\Omega|^2 + \delta^2}$ and eigenstates which often called dressed states

$$|\phi_\pm\rangle = \frac{1}{N_\pm}\left(\Omega^*|g\rangle + (-\delta \pm \sqrt{|\Omega|^2 + \delta^2})|e\rangle\right). \tag{2.13}$$

Note that $|g\rangle$ and $|e\rangle$ are already rotated; for convenience, I use the same label. The normalized factors are $N_\pm^2 = |\Omega|^2 + \left(-\delta \pm \sqrt{|\Omega|^2 + \delta^2}\right)$.

When the excitation is far off-resonant ($|\delta| \gg \|\Omega|$), the dressed state reduces to the bare state without the coupling, i.e., for the blue-detuned case

$$|\phi_+\rangle \approx \frac{\Omega^*}{2\delta}|g\rangle + |e\rangle \approx |e\rangle, \qquad |\phi_-\rangle \approx |g\rangle - \frac{\Omega}{2\delta}|e\rangle \approx |g\rangle. \tag{2.14}$$

$$\epsilon_+ \approx \hbar(\delta + \frac{|\Omega|^2}{4\delta}), \qquad \epsilon_- \approx -\hbar\frac{|\Omega|^2}{4\delta}. \tag{2.15}$$

We see that the eigenenergy of the ground and excited states shifts by $\hbar\frac{|\Omega|^2}{4\delta}$ in opposite directions; this effect is called the AC stark shift. If Ω is inhomogeneous, it can be used to create a trapping potential for optical tweezers and dipole trap.

Consider the case that we turn on the coupling when the atoms are initially in the ground state; then the detuning is swept adiabatically from far blue detuned to far red detuned, where the Landau-Zener transition is negligible if the swept is slow compared to the Rabi frequency, and we transfer the state from $|g\rangle$ along the channel $|\phi_-\rangle$ to the case $\delta \approx +\infty$ where $|\phi_-\rangle$ reduces to $|e\rangle$. Finally, if we turn off the coupling, the atoms will end up in the bare state $|e\rangle$. The above

process is called an adiabatic rapid passage.

2.3 Optical Stark shift

In the last section, we have seen the effect of the AC stark shift when the excitation is far from resonant. In principle this light shift can be derived from the second-order time-dependent perturbation theory without RWA, i.e.,

$$\Delta E_\alpha = -\sum_{\beta\neq\alpha} \frac{2\omega_{\beta\alpha}|\langle\alpha|\mathbf{d}\cdot\hat{\boldsymbol{\epsilon}}|\beta\rangle|^2|\epsilon|^2}{\hbar(\omega_{\beta\alpha}^2-\omega^2)}, \tag{2.16}$$

where $\omega_{\beta\alpha} = (E_\beta - E_\alpha)/\hbar$. For the large detuning and two-level case, this reduces to the AC Stark shift in the previous section, and the $\omega_{\beta\alpha}$ on the numerator shows the opposite shift for the ground and excited states. We can obtain the polarizability $\alpha(\omega)$ of the system by $-\Delta E/|\epsilon|^2$, and the result

$$\alpha(\omega) = \sum_{\beta\neq\alpha} \frac{2\omega_{\beta\alpha}|\langle\alpha|\mathbf{d}\cdot\hat{\boldsymbol{\epsilon}}|\beta\rangle|^2}{\hbar(\omega_{\beta\alpha}^2-\omega^2)} \tag{2.17}$$

is Kramers-Heisenberg formula for the polarizability.

However, since the electric field is a vector, the polarizability should be a tensor which satisfies $d_\mu(\omega) = \alpha_{\mu\nu}(\omega)\epsilon_\nu$, so the light shift in general should be written in the form $\Delta E = -\alpha_{\mu\nu}(\omega)\epsilon_\mu\epsilon_\nu$ with

$$\alpha_{\mu\nu}(\omega) = \sum_{\beta\neq\alpha} \frac{2\omega_{\beta\alpha}\langle\alpha|d_\mu|\beta\rangle\langle\beta|d_\nu|\alpha\rangle}{\hbar(\omega_{\beta\alpha}^2-\omega^2)}. \tag{2.18}$$

Note that the above expression assumes linear polarization, if the light is circularly polarized the $\omega_{\beta\alpha}$ in the numerator should be replaced by ω.

Since the state in the atomic BEC is typically described under the hyperfine basis $|F, m_F\rangle$,

we will rewrite the polarizability tensor for the state $|F, m_F\rangle$

$$\alpha_{\mu\nu}(\omega) = \sum_{F', m'_F} \frac{2\omega_{F'F}\langle F, m_F|d_\mu|F', m'_F\rangle\langle F', m'_F|d_\nu|F, m_F\rangle}{\hbar(\omega_{F'F}^2 - \omega^2)} \equiv \sum_{F'} \frac{2\omega_{F'F}T_{\mu\nu}}{\hbar(\omega_{F'F}^2 - \omega^2)}, \quad (2.19)$$

where the angle dependence is merely on the dipole product tensor

$$T_{\mu\nu} = \sum_{m'_F} \langle F, m_F|d_\mu|F', m'_F\rangle\langle F', m'_F|d_\nu|F, m_F\rangle. \quad (2.20)$$

It is straightforward to decompose the rank-2 tensor into scalar $T^{(0)}$, vector $T^{(1)}$, and tensor parts $T^{(2)}$ using the irreducible tensor formalism, that is,

$$T_{\mu\nu} = \frac{1}{3}T^{(0)}\delta_{\mu\nu} + \frac{1}{4}T^{(1)}_\sigma \epsilon_{\sigma\mu\nu} + T^{(2)}_{\mu\nu}. \quad (2.21)$$

$T^{(0)}$ is the trace of $T_{\mu\nu}$, that is,

$$T^{(0)} = T_{\mu\mu} \quad (2.22)$$

$T^{(1)}$ is the anti-symmetric part of the tensor, i.e.,

$$T^{(1)}_\sigma = (T_{\mu\nu} - T_{\nu\mu})\epsilon_{\sigma\mu\nu}. \quad (2.23)$$

$T^{(2)}$ is the rest part.

We now try to express the scalar and vector part by the inner product and cross product of

two vectors $\mathbf{A}$ and $\mathbf{B}$, i.e.,

$$T_0^{(0)} = -\frac{1}{\sqrt{3}}\mathbf{A}\cdot\mathbf{B}, \quad T_q^{(1)} = \frac{i}{\sqrt{2}}\mathbf{A}\times\mathbf{B}, \tag{2.24}$$

where the prefactors are given from the $\langle 1, q; 1, -q|0, 0\rangle = -(-1)^q/\sqrt{3}$ and $|\langle 1, q'; 1, q-q'|1, q\rangle| = 1/\sqrt{2}$ unless $q = q' = 0$. So $T^{(0)}$ becomes

$$\begin{aligned}
T^{(0)} &= \sum_{m'_F}\langle F, m_F|d_\mu|F', m'_F\rangle\langle F', m'_F|d_\mu|F, m_F\rangle \\
&= -\sqrt{3}\langle F, m_F|\left(\sum_{m'_F}\mathbf{d}|F', m'_F\rangle\langle F', m'_F|\mathbf{d}\right)^{(0)}|F, m_F\rangle \\
&= -\sqrt{3}\langle F||\left(\sum_{m'_F}\mathbf{d}|F', m'_F\rangle\langle F', m'_F|\mathbf{d}\right)^{(0)}||F\rangle\,\langle F, m_F|F, m_F; 0, 0\rangle \\
&= -\sqrt{3}(-1)^{2F}\sqrt{2F'+1}\begin{Bmatrix} 1 & 1 & 0 \\ F & F & F' \end{Bmatrix}\langle F||\mathbf{d}||F'\rangle\langle F'||\mathbf{d}||F\rangle \\
&= -\sqrt{3}(-1)^{F+F'}\sqrt{2F+1}\begin{Bmatrix} 1 & 1 & 0 \\ F & F & F' \end{Bmatrix}|\langle F||\mathbf{d}||F'\rangle|^2 \\
&= |\langle F||\mathbf{d}||F'\rangle|^2.
\end{aligned} \tag{2.25}$$

We used the Wigner-Eckert theorem in the third row, and further express the reduced matrix

elements by Wigner-6j symbol using

$$\begin{aligned}
&\langle F||\left(\sum_{m_F''}\mathbf{d}|F'',m_F''\rangle\langle F'',m_F''|\mathbf{d}\right)^{(k)}||F'\rangle \\
=&(-1)^{k+F+F'}\sqrt{(2F''+1)(2k+1)}\begin{Bmatrix}1 & 1 & k\\ F' & F & F''\end{Bmatrix}\langle F||\mathbf{d}||F''\rangle\langle F''||\mathbf{d}||F\rangle.
\end{aligned} \tag{2.26}$$

The proof can be found in chapter 7 of [27], where the 1 in the Wigner-6j indicates the rank of the dipole operator, and the Wigner-6j value is $(-1)^{-F-F'-1}/\sqrt{3(2F+1)}$. In the second last row of Eq. (2.25) we also used the conjugate of the reduced matrix elements

$$\langle F'||T^{(k)}||F\rangle = (-1)^{F'-F}\sqrt{\frac{2F+1}{2F'+1}}\langle F||T^{(k)}||F'\rangle^*. \tag{2.27}$$

Similarly, we can express the vector part

$$\begin{aligned}
T_q^{(1)} &= 2\sum_{m_F'}\langle F,m_F|\mathbf{d}|F',m_F'\rangle\times\langle F',m_F'|\mathbf{d}|F,m_F\rangle \\
&= -i2\sqrt{2}\langle F,m_F|\left(\sum_{m_F'}\mathbf{d}|F',m_F'\rangle\times\langle F',m_F'|\mathbf{d}\right)_q^{(1)}|F,m_F\rangle \\
&= -i2\sqrt{2}\langle F||\left(\sum_{m_F'}\mathbf{d}|F',m_F'\rangle\times\langle F',m_F'|\mathbf{d}\right)^{(1)}||F\rangle\,\langle F,m_F|F,m_F;1,q\rangle \\
&= -i2\sqrt{2}(-1)^{2F+1}\sqrt{3(2F'+1)}\begin{Bmatrix}1 & 1 & 1\\ F & F & F'\end{Bmatrix}\langle F||\mathbf{d}||F'\rangle\langle F'||\mathbf{d}||F\rangle\frac{m_F\delta_{q0}}{F(F+1)} \\
&= i2\sqrt{2}(-1)^{F+F'}\sqrt{3(2F+1)}\begin{Bmatrix}1 & 1 & 1\\ F & F & F'\end{Bmatrix}|\langle F||\mathbf{d}||F'\rangle|^2\frac{m_F\delta_{q0}}{F(F+1)}.
\end{aligned} \tag{2.28}$$

Note that the vector part is linear to m_F, and the only non-vanishing part is $T_0^{(1)}$, thereby the electric field vector should be $\sim (\boldsymbol{\epsilon} \times \boldsymbol{\epsilon}^*)_0^{(1)}$ to contract the polarizabiity.

Finally, following the similar procedure, the tensor part can be expressed as

$$T_q^{(2)} = (-1)^{F+F'} \sqrt{\frac{5(2F+1)}{F(F+1)(2F-1)(2F+3)}} \begin{Bmatrix} 1 & 1 & 2 \\ F & F & F' \end{Bmatrix} |\langle F||\mathbf{d}||F'\rangle|^2 [m_F^2 - F(F+1)]\delta_{q0} \tag{2.29}$$

Notice that all non-vanishing irreducible components $T_q^{(k)}$ should satisfy $q = 0$ to preserve m_F, and thereby contract the $T_q^{(k)}$ to a rank-0 energy shift, the corresponding electric field tensor $(\mathbf{EE})_{q'}^{(k')}$ should satisfy $k' = k$ and $q' = 0$. So, the total energy shift can be expressed by

$$\begin{aligned} &\Delta E(F, m_F, \omega) \\ &= -\sum_{F'} \frac{2}{\hbar(\omega_{F'F}^2 - \omega^2)} \left[\frac{\omega_{F'F}}{3} T^{(0)} |\epsilon|^2 + \frac{\omega}{4} T_0^{(1)} (\boldsymbol{\epsilon}^* \times \boldsymbol{\epsilon})_z + \frac{\omega_{F'F}}{\sqrt{6}} T_0^{(2)} (3|\epsilon_z|^2 - |\epsilon|^2) \right]. \end{aligned} \tag{2.30}$$

We note that the first term in the square bracket is independent of the polarization of the electric field, so it is called the scalar light shift, and we will show below that it reduces to the familiar AC Stark shift for large detunings. The second term is called the vector light shift, since the rank of the tensor is 1, where ω in the second term indicates that the vector light shift comes from the circular polarized light. The last term is related to the rank-2 tensor, so we call it tensor light shift.

Writing out the m_F dependence, we have

$$\begin{aligned} \delta E(F, m_F, \omega) = &- \alpha^{(0)}(F, \omega)|\epsilon|^2 - \alpha^{(1)}(F, \omega)(i\boldsymbol{\epsilon}^* \times \boldsymbol{\epsilon})_z \frac{m_F}{F} \\ &- \alpha^{(2)}(F, \omega) \frac{3|\epsilon_z|^2 - |\epsilon|^2}{2} \frac{3m_F^2 - F(F+1)}{F(2F-1)}, \end{aligned} \tag{2.31}$$

where the scalar, vector and tensor polarizabilities are

$$\begin{aligned}
\alpha^{(0)}(F,\omega) &= \sum_{F'} \frac{2\omega_{F'F}|\langle F||\mathbf{d}||F'\rangle|^2}{3\hbar(\omega_{F'F}^2-\omega^2)}, \\
\alpha^{(1)}(F,\omega) &= \sum_{F'} (-1)^{F'+F+1}\sqrt{\frac{6F(2F+1)}{F+1}} \begin{Bmatrix} 1 & 1 & 1 \\ F & F & F' \end{Bmatrix} \frac{\omega|\langle F||\mathbf{d}||F'\rangle|^2}{\hbar(\omega_{F'F}^2-\omega^2)}, \\
\alpha^{(2)}(F,\omega) &= \sum_{F'} (-1)^{F'+F}\sqrt{\frac{40F(2F+1)(2F-1)}{3(F+1)(2F+3)}} \begin{Bmatrix} 1 & 1 & 2 \\ F & F & F' \end{Bmatrix} \frac{\omega_{F'F}|\langle F||\mathbf{d}||F'\rangle|^2}{\hbar(\omega_{F'F}^2-\omega^2)}.
\end{aligned} \tag{2.32}$$

It is worth noting that the vector light shift is linear to m_F, thereby it is similar to the weak field Zeeman shift, and we can view the AC electric field as an effective magnetic field, i.e. $\mathbf{B}_{eff} \sim (i\boldsymbol{\epsilon}^* \times \boldsymbol{\epsilon})_z$. Clearly, only a circularly polarized light contributes to the vector light shift; for the case $\hat{\boldsymbol{\epsilon}} = (\hat{e}_x + i\hat{e}_y)/\sqrt{2}$, the effective B field is along $(i\hat{\boldsymbol{\epsilon}}^* \times \hat{\boldsymbol{\epsilon}})_z = -\hat{e}_z$.

2.3.1 Tune-out (magic) Wavelength

In this section, we will focus on the case of large detuning, where the detuning is much greater than the hyperfine splitting ($\sim$GHz) so we can ignore the hyperfine structure. In this case the light shift can be calculated from the two-level AC Stark shift $-\hbar|\Omega|^2/4\delta$, but if more energy levels are involved, it is possible to cancel out the scalar light shift, and the wavelength of the incident light is referred to as the tune-out (magic) wavelength. To see this, we first decompose the hyperfine structure reduced matrix elements into fine structure reduced matrix

elements. Using

$$\begin{aligned}\langle F||\mathbf{d}||F'\rangle &\equiv \langle J, I; F||\mathbf{d}||J', I'; F'\rangle \\ &= \langle J||\mathbf{d}||J'\rangle(-1)^{F'+J+I+1}\sqrt{(2F'+1)(2J+1)}\begin{Bmatrix} J & J' & 1 \\ F' & F & I \end{Bmatrix},\end{aligned} \tag{2.33}$$

and Biedenharn—Elliott sum rule [27], the polarizabilities become

$$\begin{aligned}\alpha^{(0)}(F,\omega) &\approx \sum_{J'}\frac{2\omega_{J'J}|\langle J||\mathbf{d}||J'\rangle|^2}{3\hbar(\omega_{J'J}^2-\omega^2)}, \\ \alpha^{(1)}(F,\omega) &\approx \sum_{J'}(-1)^{-2J-J'-F-I+1}\sqrt{\frac{6F(2F+1)}{F+1}}(2J+1)\frac{\omega|\langle J||\mathbf{d}||J'\rangle|^2}{\hbar(\omega_{J'J}^2-\omega^2)}\begin{Bmatrix} 1 & 1 & 1 \\ J & J & J' \end{Bmatrix}\begin{Bmatrix} J & J & 1 \\ F & F & I \end{Bmatrix}, \\ \alpha^{(2)}(F,\omega) &\approx \sum_{J'}(-1)^{-2J-J'-F-I}\sqrt{\frac{40F(2F+1)(2F-1)}{3(F+1)(2F+3)}}(2J+1) \\ &\quad \frac{\omega_{J'J}|\langle J||\mathbf{d}||J'\rangle|^2}{\hbar(\omega_{J'J}^2-\omega^2)}\begin{Bmatrix} 1 & 1 & 2 \\ J & J & J' \end{Bmatrix}\begin{Bmatrix} J & J & 2 \\ F & F & I \end{Bmatrix},\end{aligned} \tag{2.34}$$

where the $\omega_{F'F}$ is replaced by $\omega_{J'J}$ due to large detuning.

Now we apply this to the atom we are interested, i.e., ^{87}Rb. The energy level of the ground state and D line is shown in Fig. 2.1. The dashed level corresponds to the tune-out wavelength which makes the $\alpha^{(0)}(F,\omega)$ vanishing.

From large detuning we have $2\omega_{J'J}/(\omega_{J'J}^2-\omega^2)\approx 1/\delta$, thereby

$$\alpha^{(0)}(F,\omega) \approx \frac{|\langle J=\frac{1}{2}||\mathbf{d}||J'=\frac{1}{2}\rangle|^2}{3\hbar\delta_1}+\frac{|\langle J=\frac{1}{2}||\mathbf{d}||J'=\frac{3}{2}\rangle|^2}{3\hbar\delta_2}, \tag{2.35}$$

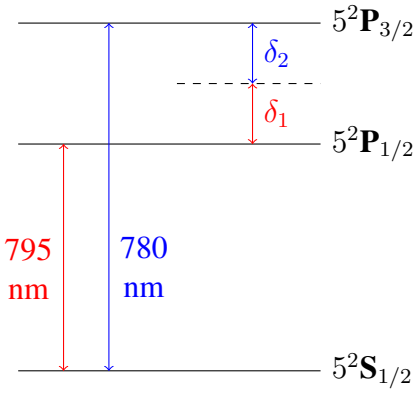

Figure 2.1: ^{87}Rb D line.

where $\langle J = \frac{1}{2}||\mathbf{d}||J' = \frac{1}{2}\rangle = 2.992ea_0$, $\langle J = \frac{1}{2}||\mathbf{d}||J' = \frac{3}{2}\rangle = 4.227ea_0$ [28]. Here, a_0 is the Bohr radius. Note that the ratio of the reduced matrix element is approximately $\sqrt{2}$. Therefore, at the tune-out wavelength λ_{magic}, the $\delta_2 + 2\delta_1 = 0$, that is,$(1/780 - 1/\lambda_{\text{magic}}) + 2(1/795 - 1/\lambda_{\text{magic}}) = 0$. So, the tune-out wavelength is $\lambda_{\text{magic}} \approx 790\,\text{nm}$.

Normally we don't need to consider the effect of the vector light shift and tensor light shift because the scalar light shift dominates, however, around the tune-out wavelength the higher rank light shift is not negligible.

It is interesting to see that the tensor polarizability $\alpha^{(2)}(F,\omega)$ is also vanishing around λ_{magic} for the ground state of the ^{87}Rb, owing to the vanishing Wigner-6j, i.e., $\begin{Bmatrix} 1 & 1 & 2 \\ \frac{1}{2} & \frac{1}{2} & \frac{1}{2} \end{Bmatrix} = \begin{Bmatrix} 1 & 1 & 2 \\ \frac{1}{2} & \frac{1}{2} & \frac{3}{2} \end{Bmatrix} = 0$. So at the tune-out wavelength, if the incident light is not purely linear polarized, the only nonvanishing light shift comes from the vector light shift, and its effect is analogous to an effective magnetic field.

2.3.2 AC vector light shift as RF

In the previous section, we have seen that the vector light shift can be analogous to a DC effective magnetic field. Can we make it an AC effective magnetic field so that it can drive the magnetic dipole transition? The time dependence can be introduced from the two-tone circularly polarized light $\mathbf{E} = \boldsymbol{\epsilon}[(\hat{e}_x + i\hat{e}_y)/\sqrt{2}](e^{-i(\omega+\Delta\omega)t} + e^{-i(\omega-\Delta\omega)t}) + \text{C.C.}$, where ω can be selected to tune out the scalar light shift and $\Delta\omega$ is the modulation frequency that can be easily added in the experiments by an acousto-optic modulator (AOM). Consequently we have an effective B field $\mathbf{B}_{eff} \sim -2[\cos(2\Delta\omega t) + 1]\hat{e}_z$, thereby apart from the DC effective magnetic field along the light propagation, we also obtain an effective AC magnetic field with angular frequency $2\Delta\omega$ along the same direction. We can view it as an effective RF field, which is capable of driving the magnetic dipole transition between different m_F states in the $5^2\text{S}_{1/2}$ manifold of ^{87}Rb, where the electric dipole transition is forbidden due to $J = J' = 0$.

2.4 Laser Cooling

Previous sections neglect spontaneous emission and dissipation in the system. In this section, we add the dissipation into the system and discuss the laser cooling techniques from the optical Bloch equation.

2.4.1 Optical Molasses

With the spontaneous emission, the pure state decoheres to a mixed state typically described by a density matrix ρ satisfying

$$\begin{aligned}
\partial_t \rho_{ee} &= i\frac{\Omega}{2}(\rho_{eg} - \rho_{ge}) - \Gamma\rho_{ee}, \\
\partial_t \rho_{gg} &= -i\frac{\Omega}{2}(\rho_{eg} - \rho_{ge}) + \Gamma\rho_{ee}, \\
\partial_t \rho_{ge} &= -(\frac{\Gamma}{2} - i\delta)\rho_{ge} - i\frac{\Omega}{2}(\rho_{ee} - \rho_{gg}), \\
\partial_t \rho_{eg} &= -(\frac{\Gamma}{2} + i\delta)\rho_{eg} + i\frac{\Omega}{2}(\rho_{ee} - \rho_{gg}),
\end{aligned} \tag{2.36}$$

where Ω and δ are the Rabi frequency and the detuning, and Γ is the excited state decay rate [29]. The force on an atom can be derived using Heisenberg equation of motion, i.e.,

$$\mathbf{F} = \frac{d}{dt}\langle \mathbf{p} \rangle = \frac{i}{\hbar}\langle [H, \mathbf{p}] \rangle = -\langle \boldsymbol{\nabla} H \rangle = -\mathrm{Tr}(\rho \boldsymbol{\nabla} H). \tag{2.37}$$

Since we are interested in the force induced by the laser-atom interaction, and under dipole approximation the force becomes

$$\mathbf{F} = -\frac{\hbar}{2}(\rho_{eg}^* \boldsymbol{\nabla}\Omega + \rho_{eg} \boldsymbol{\nabla}\Omega^*). \tag{2.38}$$

We know that one part of the force is related to the scalar light shift, which only depends on the magnitude of Rabi frequency; thus we decompose it to be a phase irrelevant and a phase relevant

term using $\Omega = |\Omega| e^{i\phi}$, i.e.,

$$\boldsymbol{\nabla}\Omega = \Omega\left(\frac{\boldsymbol{\nabla}|\Omega|}{|\Omega|} + i\boldsymbol{\nabla}\phi\right) \quad \Rightarrow \quad \boldsymbol{\nabla}(\ln\Omega) = \boldsymbol{\nabla}(\ln|\Omega|) + i\boldsymbol{\nabla}\phi. \tag{2.39}$$

We then use the steady-state solution of Eq. (2.36)

$$\rho_{eg} = \frac{-i\Omega}{2(\frac{\Gamma}{2} + i\delta)(1+s)}, \quad s = \frac{|\Omega|^2}{2[(\frac{\Gamma}{2})^2 + \delta^2]} \tag{2.40}$$

to replace the ρ_{eg} in Eq. (2.38), where s is the saturation parameter. We then obtain the following.

$$\mathbf{F} = \frac{\hbar s}{1+s}(\delta\boldsymbol{\nabla}\ln|\Omega| + \frac{\Gamma}{2}\boldsymbol{\nabla}\phi). \tag{2.41}$$

The first term, phase irrelevant, is the dipole force used to trap atoms; the second term, phase relevant, is the radiation-pressure force.

The previous argument assumes the atom is at rest; now we add velocity into the expression. Suppose that the atom is moving with velocity $\mathbf{v}$, the Rabi frequency Ω now becomes time dependent, that is,

$$\frac{\partial\Omega}{\partial t} = \mathbf{v}\cdot\nabla\Omega. \tag{2.42}$$

The steady-state solution of the optical Bloch equations has to change due to this time dependence. Treating the change as a perturbation and keeping the terms to linear order of $\mathbf{v}$, we have

$$\frac{\partial\rho_{eg}}{\partial t} = \rho_{eg}\left(\frac{1}{\Omega}\frac{\partial\Omega}{\partial t} - \frac{1}{1+s}\frac{\partial s}{\partial t}\right), \quad \frac{\partial(\rho_{ee}-\rho_{gg})}{\partial t} = -(\rho_{ee}-\rho_{gg})\frac{1}{1+s}\frac{\partial s}{\partial t}. \tag{2.43}$$

The final steady-state solution becomes

$$\rho_{eg} = \frac{-i\Omega\Gamma\gamma_v^*/2}{\Gamma_v|\gamma_v|^2 + |\Omega|^2 \mathrm{Re}[\gamma_v]}, \tag{2.44}$$

where Re stands for the real part and

$$\Gamma_v = \Gamma - \frac{s}{1+s}\mathbf{v}\cdot\left(\frac{\boldsymbol{\nabla} s}{s}\right), \quad \gamma_v = \frac{\Gamma}{2} + i\delta + \frac{1-s}{1+s}\mathbf{v}\cdot\frac{\boldsymbol{\nabla} s}{2s} + i\mathbf{v}\cdot\boldsymbol{\nabla}\phi. \tag{2.45}$$

We can obtain the total force on the moving atom by putting this in Eq. (2.38). Now we study the case that the incident light is a plane wave with wavenumber $\mathbf{k}$, so the $\boldsymbol{\nabla} s = \boldsymbol{\nabla}|\Omega| = 0$ and $\boldsymbol{\nabla}\phi = \mathbf{k}$. We then obtain

$$\rho_{eg} = \frac{-i\Omega}{2[\Gamma/2 + i\delta(\mathbf{v})](1+s(\mathbf{v}))}, \quad s(\mathbf{v}) = \frac{|\Omega|^2}{2[(\frac{\Gamma}{2})^2 + \delta(v)^2]} \tag{2.46}$$

where $\delta(\mathbf{v}) = \delta + \mathbf{k}\cdot\mathbf{v}$. We notice that the only difference between Eq. (2.46) and Eq. (2.40) is a Doppler shift added to the detuning. And the radiation-pressure force becomes

$$\mathbf{F}_{rad} = \frac{\hbar\mathbf{k}\Gamma}{2}\frac{s(\mathbf{v})}{1+s(\mathbf{v})}. \tag{2.47}$$

For a red-detuned light ($\delta > 0$), the force is frictional, as can be seen from Fig. 2.2. And if two red detuned beams with wave vector $\mathbf{k}$ and $-\mathbf{k}$ are involved, the deceleration effect is symmetric and can be used to slow the motion of the atomic gas along the direction of $\mathbf{k}$. Furthermore, if three orthogonal pairs of these Doppler cooling beams are added to the system, the atom's deceleration will be along every direction, and the temperature of the gas can be largely decreased. This

technique is typically referred to as optical molasses [30]. The limit of this cooling is $T =$

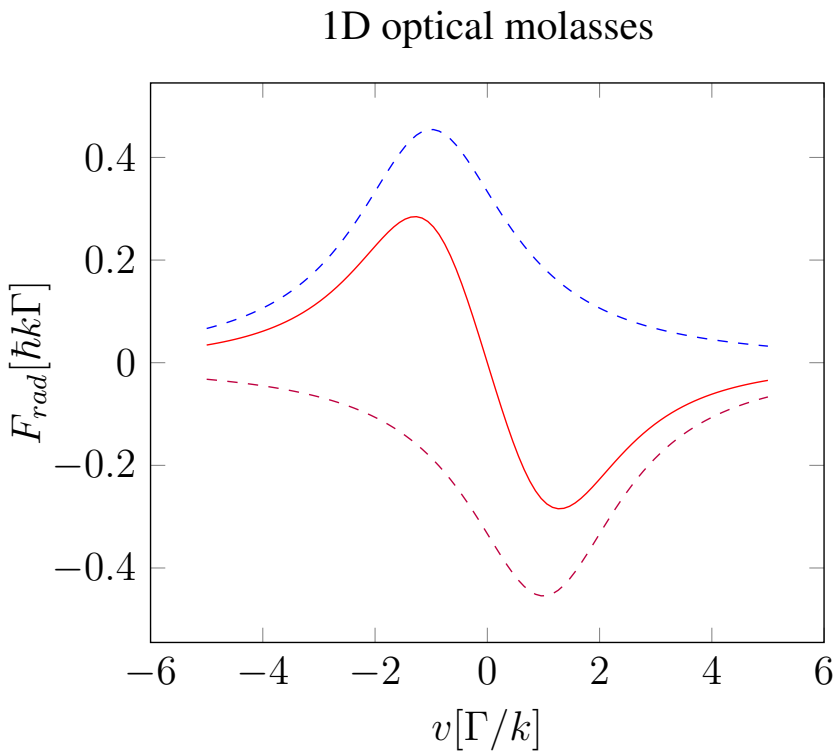

Figure 2.2: Frictional force of Doppler cooling when $s(0) = 2$ and $\delta = \Gamma$. The blue (purple) dashed line is when $\mathbf{k}$ and $\mathbf{v}$ have the same (opposite) direction, and the red solid line is the sum of the two.

$\hbar\Gamma/2k_B$, which is called the Doppler limit.

2.4.2 Magneto-optical Trap

The optical molasses can cool the temperature of the gas, but is unable to trap the atoms. In this section, I will introduce a technique that trapping and cooling can be simultaneously achieved by using circular polarized red-detuned light with anti-Helmholtz coil pairs, and the trap is referred to as the magneto-optical trap (MOT) [31].

For an anti-Helmoholtz pair with the symmetry axis along $\mathbf{z}$, around the center of the trap, the magnetic field produced can be expressed by $\mathbf{B}(x, y, z) = B_{xx}\mathbf{x} + B_{yy}\mathbf{y} + B_{zz}\mathbf{z}$, and due to

symmetry $B_{xx} = B_{yy}$ and $B_{zz} = -2B_{xx}$ derived from $\boldsymbol{\nabla} \cdot \mathbf{B} = 0$.

Now let us consider the cooling along the z direction. The magnetic gradient along z gives a spatially dependent Zeeman shift as shown in Fig. 2.3, where for simplicity the ground and excited states are $|F = 0\rangle$ and $|F = 1\rangle$, so we only need to consider the Zeeman shift on the excited states. Meanwhile, a pair of red-detuned circular-polarized counter-propogating beams propogates along the z direction. The polarizations of the two beams are opposite compared to the quantization axis $\hat{e}_z$.[1]

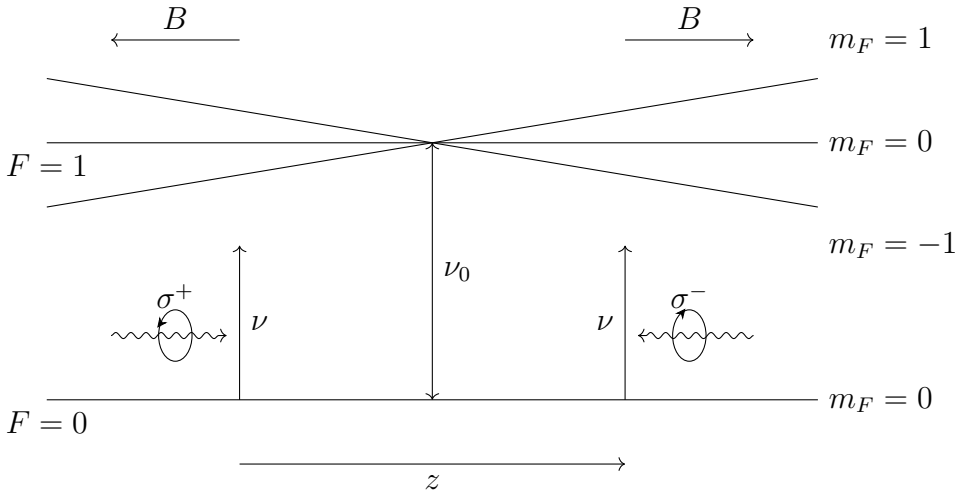

Figure 2.3: MOT scheme.

We now calculate the radiation force for an atom located at z with velocity v along $\hat{e}_z$. The detuning for the σ_- and σ_+ light can be expressed by

$$\delta^{(-)}(z, v) = -\nu + (\nu_0 - \Delta_B(z)) - kv, \quad \delta^{(+)}(z, v) = -\nu + (\nu_0 + \Delta_B(z)) + kv, \tag{2.48}$$

where $\hbar\Delta_B(z) = g\mu_B B_{zz} z$ is the Zeeman splitting at z. We can obtain the radiation-pressure force by plugging this into Eq. (2.47), and the only difference compared to the optical molasses is

[1] But the polarization is the same in the optical reference frame, i.e., if we ride on the beam the polarization would be the same.

the kv should be replaced by $kv + \Delta_B(z)$, therefore the radiation-pressure force can be expressed by

$$F_{rad}(v, z) = -\alpha(v + \Delta_B(z)/k), \tag{2.49}$$

where α is the damping coefficient. In addition to the cooling force $-\alpha v$, the velocity-independent term $-\alpha\Delta_B(z)/k$ is the trapping force that pushes the atoms back to $z = 0$. So if we have this setup in 3 orthogonal directions, we can obtain the 3D optical molasses and a 3D trap simultaneously, and it is called 3D MOT.

2.4.3 Polarization gradient cooling

The MOT and optical molasses cannot beat the Doppler limit because of random heating from the spontaneous emission. In this section, I will introduce a sub-Doppler cooling scheme which exploits the internal structure of atoms and the fact that light can exert forces on atoms beyond the simple Doppler effect. The force comes from the spatial dependence of the polarization; thus, it is also called polarization gradient cooling (PGC) [32]. Generally speaking, the PGC requires two red-detuned counterpropogating beams with orthogonal polarization. In this section, I will discuss two cases: (i) the orthogonal linear polarized configuration and (ii) the orthogonal circular polarized configuration.

2.4.3.1 Linear polarization configuration

In the section. 2.3, we have seen that the AC Stark shift can be decomposed to the scalar, vector, and tensor parts. Here, we will use the vector light shift that lifts the degeneracy of ground and excited states of the atom analogous to the Zeeman effect under a spatial-dependent

polarization setup.

Consider the two counter-propogating beams are polarized along $\hat{e}_x$ and $\hat{e}_y$, i.e.,

$$\begin{aligned}\mathbf{E}(z,t) &= E_0 e^{ikz-i\omega t}\hat{e}_x + E_0 e^{-ikz-i\omega t}\hat{e}_y + \text{C.C.} \\ &= E_0 e^{-i\omega t}[e^{ikz}\hat{e}_x + e^{-ikz}\hat{e}_y] + \text{C.C.}\end{aligned} \tag{2.50}$$

Note that the $|E|$ is spatial independent, but the polarization is spatial independent, thereby the scalar light shift cannot break the degeneracy and the vector light shift will lift the degeneracy if the effective magnetic field is non-vanishing.

Using Eq. (2.31) the effective magnetic field becomes

$$\mathbf{B}_{eff}(z) \sim (i\boldsymbol{\epsilon}^* \times \boldsymbol{\epsilon})_z \hat{e}_z = -2E_0^2 \sin(2kz)\hat{e}_z, \tag{2.51}$$

where $\boldsymbol{\epsilon} = E_0[e^{ikz}\hat{e}_x + e^{-ikz}\hat{e}_y]$.

For simplicity, we assume that the ground state is $|F = 1\rangle$, and the spatial-dependent shift can be seen in Fig. 2.4.

Here, we will explain the cooling process qualitatively. Due to the optical pumping effect, the steady-state solution at $z = (\frac{1}{8} + \frac{n}{2})(2\pi/k)$ would be $|1,-1\rangle$ where the light is σ_-. When the $|1,-1\rangle$ atom moves by $\frac{1}{4}(2\pi/k)$, it reaches the valley of $|1,1\rangle$, where the light is σ_+, then again due to optical pumping, the atom will be transferred to $|1,1\rangle$ in an anti-stokes process which reduces the kinetic energy of the system. This argument is similar to the Greek mythology of Sisyphus who rolling a stone upward to the peak of a mountain but it rolls off to the valley "spontaneously", and this process repeats over and over, so we typically refer to it as Sisyphus cooling. A more rigorous derivation using the optical Bloch equation is given in [33].

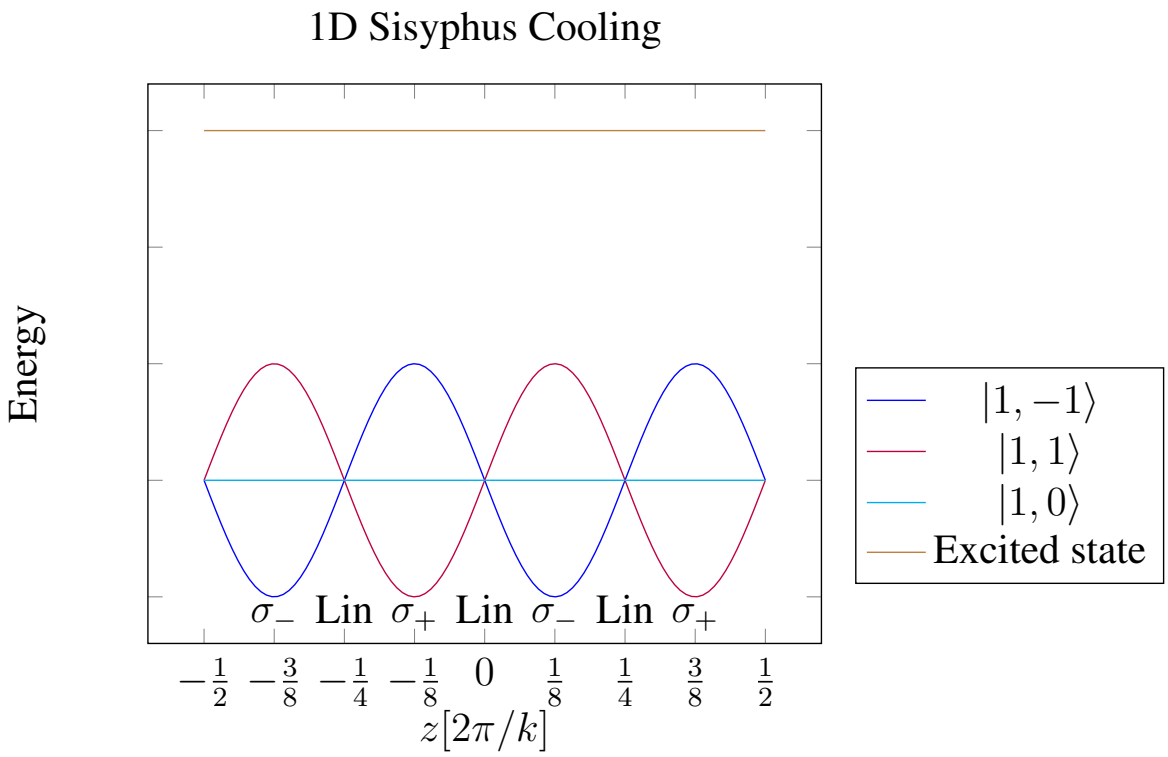

Figure 2.4: Sisyphus cooling scheme.

2.4.3.2 Circular polarzation configuration

Consider the light is incident the same as the MOT scheme but without any external magnetic field, then the electric field can be written as

$$\begin{aligned}\mathbf{E}(z,t) &= E_0 e^{ikz-i\omega t}(\hat{e}_x + i\hat{e}_y) + E_0 e^{-ikz-i\omega t}(\hat{e}_x - i\hat{e}_y) + \text{C.C.} \\ &= 2E_0 e^{-i\omega t}[\cos(kz)\hat{e}_x - \sin(kz)\hat{e}_y] + \text{C.C.}\end{aligned} \tag{2.52}$$

The $|E|$ is spatial-independent, thereby the scalar light shift does not lift the degeneracy. Note that the vector light shift is also 0 since $\boldsymbol{\epsilon} = \boldsymbol{\epsilon}^*$, so the AC Stark shift does not break the degeneracy, thereby the cooling doesn't come from the Sisyphus effect.

The polarization of the electric field at each point is linear. Consider an atom moving

along $\hat{e}_z$ with velocity v, then if we go to the frame rotating with $-kv$ about $\hat{e}_z$, the polarization is fixed. If the atom's initial position is $z = 0$, then in the rotating frame the electric field is constantly along $\hat{e}_x$. In the rotating frame, an additional gauge transformation term would modify the Hamiltonian by $\Delta H = kvF_z$, which breaks the degeneracy by a purely motion-induced effect. Again consider the $|F = 1\rangle$ atoms, for the steady state the $|1, -1\rangle$ atoms tend to move along $\hat{e}_z$, while the $|1, 1\rangle$ tends to move along $-\hat{e}_z$. If the excited state has cyclic transitions with the $|F = 1\rangle$ manifold, then the atom tends to absorb more photons from the cyclic transition because of the greater Clebsch-Gordon coefficient. In this case, the $|1, -1\rangle$ ($|1, 1\rangle$) tends to absorb more photons from $\sigma_-(\sigma_+)$ light which propagates along $-\hat{e}_z$ ($\hat{e}_z$). Thus, an atom moving right (left) tends to absorb photons moving left (right), which results in a cooling effect. A rigourous derivation is given in [33].

Note that the above argument relies on a zero external magnetic field. A nonzero magnetic field results in a nonzero shift v_B in the radiation-pressure force $F_{rad} = -\alpha(v - v_B)$, where α is the damping coefficient. Under a zero external magnetic field, the temperature limit of the PGC is the recoil limit T_r, i.e., $k_B T_r = \frac{\hbar k^2}{m}$, where m is the mass of the atom and k is the wavenumber of the light.

2.4.4 Evaporative Cooling

The laser cooling technique has a temperature limit close to the recoil limit, but still not cold enough to reach the Bose-Einstein condensation. To lower the temperature, one has to sacrifice the number of atoms using evaporation which is similar to the evaporation of hot water, where the steam with high kinetic energy goes away and the remaining water molecules with

less kinetic energy stay in the cup. This process does not conserve the number of particles, so to reach a high phase-space density one cannot evaporate too aggressively. Atomic physicists apply this evaporative cooling technique to the cold atoms [34]. In this section, I will introduce two commonly used evaporative cooling techniques: (i) RF evaporation in the magnetic trap and (ii) dipole evaporation in optical dipole trap.

2.4.4.1 RF Evaporation

Consider atoms loaded in the quadrupole magnetic trap, where the atoms with high energy are further away from the trap center. Using ^{87}Rb as an example, in the $|F = 1\rangle$ manifold only the state $|1, -1\rangle$ is magnetic trappable. So, evaporation can be realized by pumping the atoms with high kinetic energy into magnetic untrappable states, that is, $|1, 0\rangle$ and $|1, 1\rangle$. These states can be coupled by the RF field, and we can understand it using the dressed state picture. The coupled RF transition to the untrapped state is prominent when the detuning is within the Rabi frequency, that is, $|\delta| \sim |\Omega|$.

Again we only study the 1D case, the energy level of a magnetic trap along $(0, 0, z)$ is $H = gm_z\mu_B B_{zz} z$, so the energy splitting is $\delta\omega = g\mu_B B_{zz} z/\hbar$. Then given the RF frequency ω_{RF}, some of the atoms in the spatial range $\frac{\hbar}{g\mu_B B_{zz}}(\omega_{RF} \pm \Omega)$ will become untrappable. Then atoms with less energy that are located closer to the trap center will collide with the remaining trappable atoms and rethermalize to a lower temperature. This RF effect is sometimes called the "RF knife". If we continuously (adiabatically) reduce the ω_{RF}, we placed the RF knife close to the center of the trap, and the temperature will be much lower at the cost of fewer atoms.

2.4.4.2 Dipole Evaporation

Apart from the magnetic trap, the atoms can be loaded into optical dipole trap which typically uses the dipole force (scalar light shift) from a red-detuned Gaussian beam. Around the center of the trap, it can be approximated to a harmonic trap. By reducing the light intensity, the trap depth decreases, so that the atoms away from the trap center with high kinetic energy go out of the trap and become untrappable. If this trap depth reduction is done adiabatically, the atoms can collide and re-thermalize to a lower temperature.

2.5 Atomic Bose-Einstein Condensates

In the context of dilute Bose gases, the interactions between particles, though weak due to the low density of the gas, are crucial for understanding the system's behavior. These interactions are commonly approximated using a pseudo-potential that is characterized by the s-wave scattering length. This approximation is particularly useful because it simplifies the complex nature of interatomic forces into a manageable form, especially at low temperatures where s-wave scattering predominates. In this section, I will introduce the Gross-Pitevskii equation (GPE) [35, 36] to describe the ground state of BEC, and the study the elementary excitation using Bogoliubov-de-Gennes (BdG) formalism [37, 38].

2.5.1 Gross-Pitevskii equation

In a completely condensed system, each particle is in an identical single-particle state, denoted $\psi(r)$, fulfilling the normalized condition $\int d^3r|\psi(r)|^2 = 1$. The many-particle condensate's wavefunction in a mean-field approach is represented as the symmetrized product of these single-

particle wavefunctions due to its bosonic nature, expressed as $\Psi(r_1, r_2, ..., r_N) = \prod_{i=1}^{N} \psi(r_i)$.

This wavefunction is influenced by three key components: kinetic energy, potential energy, and interaction energy. The mean-field interaction energy g is dependent on the s-wave scattering length a in a weakly interaction Bose gas, i.e. $g = \frac{4\pi\hbar^2 a}{m}$. Consequently, the system's Hamiltonian is formulated as:

$$H = \sum_{i=1}^{N} \left(\frac{p_i^2}{2m} + V(r_i) \right) + g \sum_{i<j} \delta(r_i - r_j) \tag{2.53}$$

Solving for the BEC's wavefunction from this Hamiltonian is a challenging task. Thus, a variational approach is employed, where the condensate wavefunction is approximated as $\psi(r) = \sqrt{N}\phi(r)$, and the particle density is $n(r) = |\psi(r)|^2$. For large numbers of atoms, terms on the order of $1/N$ are negligible, leading to the energy functional for the N-particle wavefunction:

$$E(\phi, \phi^*) = N \int d^3r \left(\frac{\hbar^2}{2m} |\nabla\phi(r)|^2 + V(r)|\phi(r)|^2 + \frac{1}{2} N g |\phi(r)|^4 \right) \tag{2.54}$$

The solution of the ground state is obtained by minimizing this energy functional under variations of ϕ with the constraint $\int d^3r |\phi(r)|^2 = 1$, maintaining a constant total number of atoms. This minimization involves a Lagrange multiplier μ:

$$\delta \left[E(\phi, \phi^*) - \mu N \int d^3r |\phi(r)|^2 \right] = 0, \tag{2.55}$$

which leads to the time-independent Gross-Pitaevskii equation (GPE).

$$i\hbar\partial_t \phi(r) = \left[-\frac{\hbar^2}{2m}\nabla^2 + V(r) + gN|\phi(r)|^2 \right] \phi(r) = \mu\phi(r). \tag{2.56}$$

This equation, a type of non-linear Schrödinger equation, incorporates the external potential $V(r)$ and a non-linear term $gN|\phi(r)|^2$ that describes the mean-field potential of other atoms. The eigenvalue μ is the chemical potential, which differs from the mean energy per particle found in a linear Schrödinger equation. Using the condensate wavefunction $\psi(r)$ with normalized condition $\int d^3r|\psi(r)| = N$, the GPE becomes

$$i\hbar\partial_t\psi(r) = \left[-\frac{\hbar^2}{2m}\nabla^2 + V(r) + g|\psi(r)|^2\right]\psi(r) = \mu\psi(r). \tag{2.57}$$

2.5.2 Bogoliubov-de-Gennes excitations

The Bogoliubov-de-Gennes (BdG) equations, while initially formulated for superconductivity [39], are also applicable in the analysis of Bose-Einstein condensates (BECs). In the context of BECs, the BdG framework is utilized to examine the spectrum of elementary excitations. It provides a mathematical structure to describe the behavior of small perturbations from the ground state within the condensate. This application is particularly relevant in discovering the dispersion relations of these excitations and understanding the interactions within the condensate. The BdG equations offer a method for quantifying and analyzing the collective modes and the dynamics of particles in the condensate, contributing to the theoretical understanding of various phenomena observed in BECs, such as superfluidity and the formation of vortices.

From Eq. (2.57) we can obtain the ground state ψ_G and the corresponding chemical potential

$$\mu_G = \int d^3r\ \psi_G^*\left[\frac{-\hbar^2\nabla^2}{2m} + V(r) + g|\psi_G|^2\right]\psi_G. \tag{2.58}$$

For a BEC, the wavefunction ψ with "weak" excitations should also satisfy the GPE, thereby we

can decompose it into $\psi = \psi_G + \delta\psi$. Under the BdG formalism, the excitation is expressed by u and v with frequency ω, i.e.,

$$\psi(r,t) = \exp(-i\mu_G t)\left[\psi_G(r) + u(r)\exp(-i\omega t) - v^*(r)\exp(i\omega^* t)\right]. \tag{2.59}$$

Inserting it into Eq. (2.57) and separating the terms with $\exp(-i\omega t)$ and $\exp(i\omega^* t)$, we obtain the following BdG equations.

$$\omega u = \left[-\frac{\hbar^2}{2m}\nabla^2 + V(r) + 2g|\psi_G|^2 - \mu_G\right] u - g\psi_G^2 v, \tag{2.60}$$

$$-\omega v = \left[-\frac{\hbar^2}{2m}\nabla^2 + V(r) + 2g|\psi_G|^2 - \mu_G\right] v - g\psi_G^{*\,2} u. \tag{2.61}$$

This set of equations is linear and can be solved by diagonalizing.

Chapter 3: Review of Turbulence and Velocimetry

Turbulence, characterized as chaotic and unpredictable flow patterns in fluids, has intrigued scientists for centuries as a result of its complexity and elusive nature. Horace Lamb once said: ”I am an old man now, and when I die and go to heaven there are two matters on which I hope for enlightenment. One is quantum electrodynamics, and the other is the turbulent motion of fluids. And about the former I am rather optimistic.” Werner Heisenberg said something similar afterwards: ”When I meet God, I am going to ask him two questions: Why relativity? And why turbulence? I really believe he will have an answer for the first.” These reflective comments emphasize the mysterious nature of turbulence, illustrating its status as one of the most challenging and unresolved puzzles in the scientific world.

The nonlinearity inherent in turbulent flows is a fundamental aspect that makes turbulence a formidable challenge in fluid dynamics. Similar to all chaotic systems, turbulence is extremely sensitive to the initial condition, making prediction a challenging task. Furthermore, when attempting to model turbulence using mathematical equations, one encounters more unknowns than available equations. This imbalance necessitates the introduction of approximations or models to ”close” the system of equations, a significant challenge that brings uncertainties and limitations to the predictive capabilities of turbulence models. The rich physics also lies in the nonlinearity. The most profound findings in the turbulence are related to energy cascade, which is

vividly described by Lewis Fry Richardson's poetry, "Big whorls have little whorls, Which feed on their velocity; And little whorls have lesser whorls, And so on to viscosity." Energy injected into the system on a large scale by external force such as stirring and shaking, and the kinetic energy transferred from the large scale to small scales in a self-similar manner, as the "big whorls break into small whorls", and finally it is dissipated on the small scale due to viscosity.

Although turbulence is characterized by randomness and unpredictability, there is a fundamental aspect that exhibits statistical regularity: the scaling law for the kinetic energy spectrum. In the subinertial range, where the energy cascade predominantly occurs, this scaling law becomes prominent, standing as one of the most universal and consistent findings in the study of turbulence. In 1941, Andrey Kolmogorov, a prominent mathematician in turbulence research, introduced groundbreaking theories that helped unveil the statistical nature of turbulent flows [18, 19, 20]. Kolmogorov's theories elucidated the multiscale nature of turbulence, shedding light on the energy cascade process and the manifestation of the scaling laws in the kinetic energy spectrum. His work laid a robust foundation for understanding the complexities inherent in turbulent flows, steering subsequent research toward a more profound comprehension of this chaotic yet structured phenomenon.

This chapter gives a review for the turbulence and velocimetry, from incompressible classical turbulence to compressible turbulence as well as quantum turbulence. The Kolomogorov theory for the incompressible turbulence is discussed in detail. Then the compressible turbulence is first introduced under a coarse-grained picture. Finally, the quantum turbulence in both superfluid Helium and atomic BEC is discussed. This chapter also gives a review for the velocimtery techiniques in both classical and quantum fluids.

3.1 Incompressible Turbulence

In this section, the fluid considered is incompressible fluid, so the density of the fluid is constant and the velocity field satisfies $\nabla \cdot \mathbf{v} = 0$ due to continuity equation.

3.1.1 Basic features of turbulence

Before discussing the details of the features, it is necessary to introduce the concept of "eddy", which is defined as the region of significant self-correlation. If we stir a fluid to create turbulence, the largest eddy would be the system size, where it shows the macroscopic flow. In Richardson's poems, this large eddy then breaks into smaller eddies which have smaller correlation length, and finally to a scale that dissipation dominates.

3.1.1.1 Irregular, random and chaotic

The most annoying feature of turbulence is that its velocity field $\mathbf{v}(\mathbf{x}, t)$ varies significantly and irregularly. Suppose that you place a velocity sensor in the fluid and record the velocity. You would obtain a trace as in the Fig. 3.1. And if you repeat the measurement, the traces are unrepeatable even though you set all the experimental parameters the same, which means that at least some of the parameters are not actually under control.

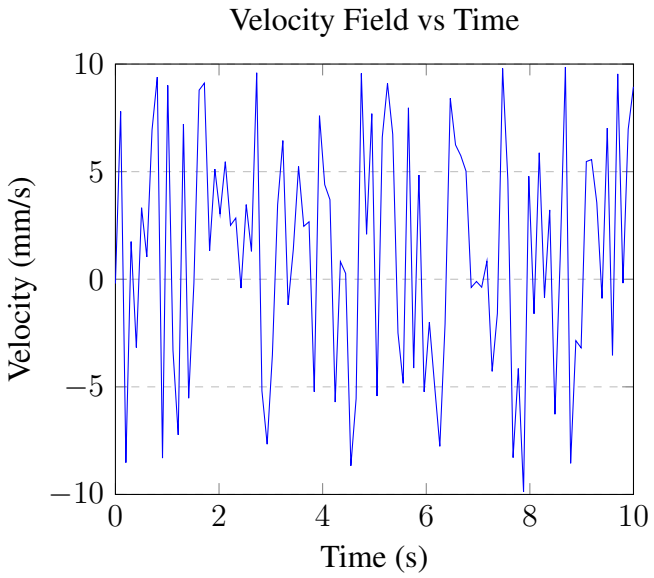

Figure 3.1: A representation of the chaotic and random nature of the velocity field over time.

3.1.1.2 High Reynolds number

The Reynolds number (Re) [40] is a dimensionless quantity that is used to predict flow patterns in fluid mechanics. It is defined as

$$Re = \frac{UL}{\nu}, \tag{3.1}$$

where U is the characteristic velocity, L is the characteristic length, and ν is the kinematic viscosity.

The Reynolds number is actually the ratio of convection to diffusion, or the inertial force to viscous force, which can be seen from the Navier-Stokes equation [41] for incompressible fluid

$$\frac{\partial \mathbf{v}}{\partial t} + (\mathbf{v} \cdot \nabla)\mathbf{v} = -\frac{1}{\rho}\nabla p + \nu \nabla^2 \mathbf{v} + f_{\text{ext}}, \tag{3.2}$$

where ρ is the density, p is the pressure, and f_{ext} is the external force. The term $(\mathbf{v} \cdot \nabla)\mathbf{v}$ is the inertial force, which also describes the convection of the momentum. And $\nu\nabla^2\mathbf{v}$ is the viscous force, also known as the diffusion force. The ratio of these two terms is aprroximately to be $\frac{UL}{\nu}$ in the scale you are interested in. So high Re ($Re \gg 1$) typically stands for the case when the scale is set to the large scale, where the dissipation from the viscous force can be ignored.

3.1.1.3 Dissipation

Dissipation occurs always in the fluid. On a small scale, dissipation dominates ($Re \ll 1$). For the steady state, the energy injection rate must be equal to the dissipation rate

$$\epsilon \approx \frac{u_0^2}{\tau_0} = \frac{u_0^3}{L_0}, \tag{3.3}$$

where u_0, L_0 are the charactersitic velocity and length for the largest eddy, $\tau_0 = \frac{L_0}{u_0}$ is its characteristic time. Note that only in the steady state we can write the dissipation rate in a form independent of ν.

The dissipation range η must be related to the dissipation rate ϵ and the viscosity ν. Dimensional analysis gives $\eta = (\frac{\nu^3}{\epsilon})^{\frac{1}{4}}$.

3.1.1.4 Efficient mixing

For a regular nonturbulent fluid, suppose that at $t = 0$ we have two closely located tracer particles, its relative distance $|\Delta x|$ at time t would satisfy $\langle|\Delta x|^2\rangle \propto Dt$, where D is the diffusion coefficient. This $\sqrt{t}$ diffusion rate can be derived from Fick's second law of diffusion [42].

In turbulence, since dissipation (viscosity) is closely related to diffusion, $|\Delta x|^2$ must be a

function of the dissipation rate ϵ and t. From the dimensional analysis we have $\langle|\Delta x|^2\rangle = \epsilon t^3$. The chaotic motion in the turbulent fluid accelerates diffusion. This $t^{3/2}$ suggests superdiffusion in turbulence, which is called Richardson's law [43].

3.1.1.5 Vortices

A turbulent fluid is always combined with vortices. Vortices in incompressible turbulence are fundamental elements, marking regions where the fluid circulates around a core area. Understanding the dynamics of these vortices is crucial in the study of incompressible turbulence, as they are integral to the energy transfer processes and the overall chaotic motion observed in such fluid flows.

3.1.2 The Reynolds-Averaged Navier–Stokes Equations

Reynolds decomposition [44] involves breaking down the instantaneous flow variables into mean and fluctuating components. Consider a flow variable, such as velocity $\mathbf{u}$, which varies with time and space due to turbulence. It can be decomposed as follows: $\mathbf{u}(\mathbf{x}, \mathbf{t}) = \bar{\mathbf{u}}(\mathbf{x}) + \mathbf{u}'(\mathbf{x}, t)$, where $\bar{\mathbf{u}}(\mathbf{x})$ is the velocity field averaged over time and $\mathbf{u}'(\mathbf{x}, t)$ is the fluctuating part. This decomposition simplifies the equations of motion and aids in understanding and analyzing the turbulent characteristics of the flow. Applying the Reynolds decomposition to the Navier-Stokes equations [Eq. (3.2)] leads to the Reynolds-averaged Navier-Stokes equations (RANS).

$$\frac{\partial(\bar{\mathbf{v}} + \mathbf{v}')}{\partial t} + \left((\bar{\mathbf{v}} + \mathbf{v}') \cdot \nabla\right)(\bar{\mathbf{v}} + \mathbf{v}') = -\frac{1}{\rho}\nabla(\bar{p} + p') + \nu\nabla^2(\bar{\mathbf{v}} + \mathbf{v}') + f_{\text{ext}}, \tag{3.4}$$

Time average to the entire equation, we obtain

$$\bar{\mathbf{v}} \cdot \nabla \bar{\mathbf{v}} + \overline{\mathbf{v} \cdot \nabla \mathbf{v}'} = -\frac{1}{\rho} \nabla \bar{p} + \nu \nabla^2 \bar{\mathbf{v}} + \overline{f_{\text{ext}}}. \tag{3.5}$$

For incompressible fluid, we have $\nabla \cdot \bar{\mathbf{v}} = 0$ and $\nabla \cdot \mathbf{v}' = 0$, so the equation can be written as the RANS form, that is,

$$\nabla \cdot \bar{\mathbf{v}}^2 + \nabla \cdot \overline{\mathbf{v}'^2} = -\frac{1}{\rho} \nabla \bar{p} + \nu \nabla^2 \bar{\mathbf{v}} + \overline{f_{\text{ext}}}, \tag{3.6}$$

where on the left hand side $\mathbf{v}^2$ is a short hand notation for the rank 2 tensor with elements $\mathbf{v}^2_{ij} = v_i v_j$. And the $\mathbf{v}'^2$ is called the Reynolds stress tensor. Note that the above equation contains more unknowns than the number of equations. The equation of Reynolds stress tensor actually introduces a higher-order tensor of $\mathbf{v}'$, and the number of unknowns is always greater than the number of equations. This difficulty is always called the "Turbulence closure problem".

3.1.3 Vortex Stretching

Vorticity is defined by $\omega = \nabla \times \mathbf{v}$. From Eq. (3.2), we have

$$\frac{\partial \mathbf{v}}{\partial t} + \frac{1}{2} \nabla (\mathbf{v} \cdot \mathbf{v}) - \mathbf{v} \times \omega = -\frac{1}{\rho} \nabla p + \nu \nabla^2 \mathbf{v} + f_{\text{ext}}, \tag{3.7}$$

where we have used $\frac{1}{2} \nabla (\mathbf{v} \cdot \mathbf{v}) = (\mathbf{v} \cdot \nabla) \mathbf{v} + \mathbf{v} \times (\nabla \times \mathbf{v})$. Now take the curl of the entire equation

$$\frac{\partial \omega}{\partial t} - \nabla \times (\mathbf{v} \times \omega) = \nu \nabla^2 \omega + \nabla \times \mathbf{f}_{\text{ext}}. \tag{3.8}$$

The second term on the left hand side (LHS) can be expanded

$$\nabla \times (\mathbf{v} \times \omega) = (\omega \cdot \nabla)\mathbf{v} - (\mathbf{v} \cdot \nabla)\omega + \mathbf{v}\nabla \cdot \omega - \omega\nabla \cdot \mathbf{v}, \tag{3.9}$$

where the last two terms on the right hand side (RHS) are 0. We then obtain the vorticity transport equation

$$\frac{\partial \omega}{\partial t} + (\mathbf{v} \cdot \nabla)\omega = (\omega \cdot \nabla)\mathbf{v} + \nu\nabla^2\omega + \nabla \times \mathbf{f}_{\text{ext}}. \tag{3.10}$$

The first term on the RHS represents "vortex streching", i.e., velocity gradient leads to the change in the rate of vorticity. The second term is the diffusion term, and we observe that the kinematic viscosity is actually the diffusion coefficient for the diffusion of vorticity.

The vortex streching is once believed to be the cause of energy cascade from an angular momentum conservation argument; however, it might not be the real cause [45], so I will only briefly state its implication to the cascade here. Consider the fluid element with vorticity ω, the fluid element tends to be more elongated under strain, and the diameter of the fluid element decreases. Assuming that the local angular momentum is conserved, the vorticity has to increase. Thus, the kinetic energy is transported from large-scale to small-scale.

3.1.4 Equilibrium range theories

Kolmogorov's theory assumes homogeneous and isotropic flow, which might be quite different from the real cases, but it is a good starting point and gives us scaling laws agrees well even with some complicated inhomogenous and anisotropic flow.

Much similar to Richardson's poet, Kolmogorov explains the idea more rigorously. It is

built on two similarity hypothesis.

3.1.4.1 Hypothesis of Kolmogorov

Kolmogorov presented a theory in which large anisotropic eddies are the primary energy carriers in turbulent flows, transferring energy across various scales. These eddies gradually lose their distinct shapes and characteristics, transitioning into a state where they are homogenous and isotropic. In this state, the energy of the eddies depends solely on the energy they receive from the larger eddies and the energy dissipation rate due to the smaller eddies.

Kolmogorov's first similarity hypothesis: At large Reynolds numbers, the local average properties of the small-scale components of any turbulent motion are determined entirely by kinematic viscosity and average rate of dissipation per unit mass.

Following his hypothesis, we can derive the characteristic length η, time τ_η and velocity u_η for the "small scale", since it only depends on ϵ and ν, i.e.,

$$\eta = \left(\frac{\nu^3}{\epsilon}\right)^{\frac{1}{4}}, \quad \tau_\eta = \left(\frac{\nu}{\epsilon}\right)^{\frac{1}{2}}, \quad u_\eta = (\epsilon\nu)^{\frac{1}{4}}. \tag{3.11}$$

It is easy to verify that the Reynolds number of the scale η is 1, which suggests a balance of the convection to diffusion.

Kolmogorov's second similarity hypothesis: There is an upper subrange (the inertial subrange) in this bandwidth of small eddies in which the local average properties are determined only by the rate of dissipation per unit mass.

On this scale, both energy injection and dissipation are negligible, and the kinetic energy is transferred from the large scale to the small scale. In steady state, the energy injected rate should be equal to the dissipation rate, and on a large scale, the dissipation is negligible, so it depends only on the energy injected rate ϵ and not on the detail of the dissipation mechanism given by ν.

In the inertial subrange, the energy spectrum depends only on k and ϵ. The kinetic energy has the unit of $L^3\tau^{-2}$. ϵ has the unit of $L^2\tau^{-3}$. From dimensional analysis we obtain $E(k) = C\epsilon^{2/3}k^{-5/3}$, where C is a constant and lies in the range of 1.5 to 2.5 for most fluids.

3.1.4.2 Velocity Structure function

The energy spectrum is not a quantity that can be measured with ease, so realistically it is worth using a more experimental friendly metric, that is, the velocity field structure function $S_p(l)$, which is defined in Eq. (3.12) based on the velocity increments δv_l,

$$\delta v_l(\vec{x}) = \langle|\vec{v}(\vec{x}+\vec{l}) - \vec{v}((\vec{x}))|\rangle \cdot \hat{l}, S_p(l) = \langle|\delta v_l(\vec{x})|^p\rangle; \tag{3.12}$$

where $\vec{l}$ is the positional separation vector of the two velocity field sample points, and $\hat{l}$ is its unit vector, and p is the order of the structure function. Note that the structure function can also be defined without the absolute value, and Kolmogorov's four-fifth law is built upon the S_3 of the longitudinal velocity increments without taking the absolute value. On the experimental side, it is more convenient to use the absolute value, so the gap between the magnitude of the odd and even order of structure function is less prominent.

Historically, experimentalists only use a single velocity sensor to read the streamline velocity

on a single spot, record its readings at different times, and then map the temporal difference to the spatial difference making use of the Galilean invariance. The second-order structure function was found to follow a scaling of $2/3$ over l, i.e. $S_2(l) \propto l^{2/3}$. This empirical law is often called the "two-thirds law", which seems to hold for all turbulent flow, at least approximately.

From Kolmogrov's second similarity hypothesis, the velocity structure function should solely depends on the dissipation rate ϵ if the relative distance l is in the inertial subrange, then using dimensional analysis, S_p has the unit of $L^p\tau^{-p}$, thus

$$S_p(l) \propto (\epsilon l)^{p/3}\,, \tag{3.13}$$

which agrees with the two-thirds law when $p = 2$.

In 1941, Kolmogorov gave an exact result for the third order longitudinal structure function

$$S_3(l) = -\frac{4}{5}\epsilon l, \tag{3.14}$$

which is called the "four-fifths law". I will introduce Kolmogorov's derivation in the following section.

3.1.4.3 Karman-Howarth-Monin relation

Kolmogorov derives the four-fifths law based on the Karman-Howarth-Monin relation [46], i.e.,

$$\partial_t \langle \mathbf{v}(\mathbf{x}) \cdot \mathbf{v}(\mathbf{x}+\mathbf{l}) \rangle = \frac{1}{2} \nabla_{\mathbf{l}} \cdot \langle \delta \mathbf{v}^2 \delta \mathbf{v} \rangle + \langle \mathbf{v}(\mathbf{x}) \cdot (\mathbf{f}_{\text{ext}}(\mathbf{x}+\mathbf{l}) + \mathbf{f}_{\text{ext}}(\mathbf{x}-\mathbf{l})) \rangle + 2\nu \nabla_{\mathbf{l}}^2 \langle \mathbf{v}(\mathbf{x}) \cdot \mathbf{v}(\mathbf{x}+\mathbf{l}) \rangle. \tag{3.15}$$

Proof: We will use the shorthand notation prime to denote the variables at $\mathbf{x}+\mathbf{l}$. From Eq. (3.2), we have

$$\partial_t v_i = -\partial_j (v_j v_i) - \partial_i P + f_{\text{ext},i} + \nu \partial_j \partial_j v_i, \tag{3.16}$$

and an equation for primed variable. Then we have

$$\begin{aligned} \partial_t \langle v_i v_i' \rangle = &- \langle v_i' \partial_j (v_j v_i) \rangle - \langle v_i \partial_j' (v_j' v_i') \rangle - \langle v_i' \partial_i P \rangle - \langle v_i \partial_i' P' \rangle \\ &+ \langle v_i' f_{\text{ext},i} \rangle + \langle v_i f_{\text{ext},i}' \rangle + \nu \langle v_i' \partial_j \partial_j v_i \rangle + \nu \langle v_i \partial_j' \partial_j' v_i' \rangle, \end{aligned} \tag{3.17}$$

where the last two terms on the first line is zero due to integral by parts and incompressibility. The viscous terms can be expressed by the derivative of the separation distance $\mathbf{l}$, that is, $\nu \langle v_i' \partial_j \partial_j v_i \rangle = \nu \langle v_i(\mathbf{x}) \partial_j \partial_j v_i(\mathbf{x}-\mathbf{l}) \rangle = \nu \nabla_{\mathbf{l}}^2 \langle v_i v_i' \rangle$, where homogeneity is used. The forcing term can be expressed as $\langle v_i(\mathbf{x})(f_{\text{ext},i}(\mathbf{x}+\mathbf{l}) + f_{\text{ext},i}(\mathbf{x}-\mathbf{l})) \rangle$.

What remains to prove is that the first two terms in the RHS of the above equation are equal to the first term on the RHS of Eq. (3.15).

$$\langle v_i' \partial_j (v_j v_i) \rangle + \langle v_i \partial_j' (v_j' v_i') \rangle = -\partial_{l_j} \langle v_i' v_j v_i \rangle + \partial_{l_j} \langle v_i v_j' v_i' \rangle = \partial_{l_j} \langle v_i' v_i \delta v_j \rangle. \tag{3.18}$$

Then using $v_i' v_i = (v_i v_i + v_i' v_i' - \delta v_i \delta v_i)/2$,

$$\partial_{l_j} \langle v_i' v_i \delta v_j \rangle = \frac{1}{2} \langle v_i^2 \partial_{l_j} \delta v_j \rangle + \frac{1}{2} \partial_{l_j} \langle v_i' v_i' \delta v_j \rangle - \frac{1}{2} \partial_{l_j} \langle \delta v_i \delta v_i \delta v_j \rangle, \tag{3.19}$$

where $\langle v_i^2 \partial_{l_j} \delta v_j \rangle = \langle v_i^2 \partial_j v_j' \rangle = 0$ because of incompressibility, and $\partial_{l_j} \langle v_i' v_i' \delta v_j \rangle = -\langle v_i v_i \partial_{l_j} v_j (\mathbf{x} - \mathbf{l}) \rangle = \langle v_i v_i \partial_j v_j (\mathbf{x} - \mathbf{l}) \rangle = 0$ because of homogenity and incompressibility. Thereby we obtain Eq. (3.15).

3.1.4.4 Derivation of four-fifths law

Considering the fully developed turbulence ($\nu \to 0$) and in the stationary limit ($t \to \infty$), the time dependence of Eq. (3.15) is removed. In the inertial subrange, the correlation length of the external force is much greater than the separation $\mathbf{l}$, so we can write the forcing term to $2\langle \mathbf{v}(\mathbf{x}) \mathbf{f}_{\text{ext}}(\mathbf{x}) \rangle = 2\epsilon$, where ϵ is the energy injection rate, which is also equal to the dissipation rate in steady state. In the high Renyolds number limit ($\nu \to 0$), the viscous term is negligible in the inertial subrange. Thus we have

$$\nabla_{\mathbf{l}} \cdot \langle \delta \mathbf{v}^2 \delta \mathbf{v} \rangle = -4\epsilon. \tag{3.20}$$

Now we consider the third-order longitudinal structure function $S_3(l)$, where the longitudinal notation is removed for simplicity.

$$S_3(l) = \frac{l_i l_j l_k}{l^3} \langle \delta v_i \delta v_j \delta v_k \rangle = 2 \frac{l_i l_j l_k}{l^3} (S_{ij,k} + S_{ki,j} + S_{jk,i}), \tag{3.21}$$

where $S_{ij,k} = \langle v_i v_j v'_k \rangle$. Using homogeneity and isotropy, we can expand the tensor $S_{ij,k}$ to

$$S_{ij,k}(l) = A(l)\delta_{ij}\frac{l_k}{l} + B(l)\left(\delta_{ki}\frac{l_j}{l} + \delta_{jk}\frac{l_i}{l}\right) + C(l)\frac{l_i l_j l_k}{l^3}. \tag{3.22}$$

And $S_3(l)$ becomes a function solely depends on $A(l)$, $B(l)$ and $C(l)$, i.e.,

$$S_3(l) = 2\frac{l_i l_j l_k}{l^3}\left[(A+2B)\left(\delta_{ij}\frac{l_k}{l} + \delta_{jk}\frac{l_i}{l} + \delta_{ki}\frac{l_j}{l}\right) + 3C\frac{l_i l_j l_k}{l^3}\right] = 6(A+2B) + 6C. \tag{3.23}$$

Now we consider connecting the structure function to the Eq. (3.20), using incompressibility

$$\nabla_{\mathbf{l}} \cdot \langle \delta\mathbf{v}^2 \delta\mathbf{v} \rangle = 4\partial_j S_{ij,i} = 4\partial_j \left[(A+4B+C)\frac{l_j}{l}\right]. \tag{3.24}$$

Using the relation $\partial_k f(l) = (l_k/l)f'(l)$ and $\partial_k(l_i/l) = \delta_{ik}/l - l_i l_k/l^3$, we have

$$\nabla_{\mathbf{l}} \cdot \langle \delta\mathbf{v}^2 \delta\mathbf{v} \rangle = 4(A' + 4B' + C') + \frac{8}{l}(A+4B+C), \tag{3.25}$$

which links the A, B and C with the dissipation rate ϵ but introducing new differential variables.

Using the incompressibility of $\partial_k S_{ij,k} = 0$ to obtain more relations,

$$\partial_k S_{ij,k} = \left[A'(l) + 2\frac{A(l)+B(l)}{l}\right]\delta_{ij} + \left[2B'(l) + C'(l) + 2\frac{C(l)-B(l)}{l}\right]\frac{l_i l_j}{l^2} = 0, \tag{3.26}$$

where the two terms in the square bracket should be both vanishing. Multiplying the first bracket

by 3 and adding the second bracket, we obtain the following.

$$\frac{d}{dl}\left[3A+2B+C\right]+\frac{2}{l}\left[3A+2B+C\right]=0. \tag{3.27}$$

The general solution is $3A+2B+C=const/l^2$, since the solution should be finite at $l\to 0$, we obtain

$$3A+2B+C=0, \quad B=-A-\frac{l}{2}A', \quad C=-A+lA'. \tag{3.28}$$

Eq. (3.23) and Eq. (3.25) become

$$S_3(l)=-12A, \quad -\epsilon=-lA''-7A'-\frac{8}{l}A. \tag{3.29}$$

Under the change of variable $y=A/l$, $x=\ln l$, the differential equation becomes

$$y''+6y'+15y=\epsilon. \tag{3.30}$$

The general solution is as follows.

$$y=\alpha\exp\left[(-3+6j)x\right]+\beta\exp\left[(-3-6j)x\right]+\frac{\epsilon}{15}. \tag{3.31}$$

Under the limit of $l\to 0$ ($x\to-\infty$), y should be finite, so $y=\epsilon/15$ and

$$S_3(l)=-\frac{4}{5}\epsilon l. \tag{3.32}$$

3.1.4.5 Velocity increments PDF and the intermittency

The velocity increments probability distribution function (PDF) is an essential metric for intermittency, which describes the anomolous scaling of the velocity increments compared to the Kolmogorov theory.

Kolmogorov theory is based on the self-similarity assumption, which leads to scale-invariant scalings for the longitudinal structure function. So, if we study the PDF of the longitudinal velocity increments $\delta v(l)$, it should also be scale-invariant, which means the large-scale velocity increment PDF should have the same shape as the small-scale velocity increment PDF in the inertial range. However, it is found that the fat-tailed feature becomes more and more clear when the spatial separation l is decreased. When the separation is large, the PDF is Guassian or near Guassian, but when the separation is small, the rare event with large velocity increments becomes more and more frequent. This scale dependent phenomenon is the symbol of intermittency, which suggests that the Kolmogorov theory needs revision to the self-similarity hypothesis.

In 1962, Kolmogorov and Obukhov gave a refined the self-similarity hypothesis [23]. The original averaged dissipation rate ϵ is replaced by a scale-dependent dissipation rate ϵ_l, which can be viewed as the filtered version of the dissipation field. The previous K41 calculation is still assumed to be valid for ϵ_l, but the whole system's expectation value should depend on the PDF of ϵ_l, which is assumed to follow a log-normal distribution. Then a refined structure function is given by

$$S_n(l) \propto (\mathbf{E}[\epsilon_l]l)^{n/3}(l/L)^{-\mu n(n-3)/18}, \tag{3.33}$$

where $\mathbf{E}$ stands for the expectation value, L is the system size and μ is experimentally measured to

be close to 0.23. So this anomalous scaling is apparent for high-order velocity structure function, and for low-order the correction is negligible since the rare event's effect to the structure function is not prominent.

3.2 Compressible turbulence

The previous sections mainly discuss incompressible turbulence, where the density of the fluid is spatially independent, so we have the incompressible condition $\nabla \cdot \mathbf{v} = 0$. However, realistically, the fluid is compressible, especially when the fluid's velocity is higher than the speed of sound. In this section we will discuss the compressible fluid, where the density now becomes a spatial-dependent variable.

3.2.1 Governing dynamics

From conservation law, we can write the transport equation of density, momentum, and kinetic energy [47], i.e.,

$$\partial_t \rho + \partial_j(\rho v_j) = 0, \tag{3.34}$$

$$\partial_t(\rho v_i) + \partial_j(\rho v_i v_j) = -\partial_i P + \partial_j \sigma_{ij} + \rho f_{\text{ext},i}, \tag{3.35}$$

$$\begin{aligned} \partial_t(\rho \frac{|\mathbf{v}|^2}{2}) + \partial_j \left[(\rho \frac{|\mathbf{v}|^2}{2} + P) v_j - 2\mu (v_i S_{ij} - \frac{1}{3} v_j S_{kk}) \right] \\ = P \partial_j v_j - 2\mu \left(|S_{ij}|^2 - \frac{1}{3} |S_{kk}|^2 \right) + \rho v_i f_{\text{ext},i}, \end{aligned} \tag{3.36}$$

where Eq. (3.35) is the compressible Navier-Stokes equation. μ is the dynamic viscosity, $S_{ij} = (\partial_j v_i + \partial_i v_j)/2$ is the symmetric strain tensor, and $\sigma_{ij} = 2\mu(S_{ij} - \frac{1}{3} S_{kk} \delta_{ij})$ is the viscous stress. Note that the Stokes hypothesis is used so that the bulk viscosity is ignored.

3.2.2 Coarse graining

Following the coarse graining and filtered appraoch used in the large eddy simulation, we can decompose any field $\mathbf{a}(\mathbf{x})$ into the large-scale component $\bar{\mathbf{a}}_l(\mathbf{x})$ and sub-grid component $\mathbf{a}'_l(\mathbf{x})$, where the coarse-grained field contains modes at scales greater than l, i.e.,

$$\bar{\mathbf{a}}_l(\mathbf{x}) = \int d^3\mathbf{r} G_l(\mathbf{r})\mathbf{a}(\mathbf{x}+\mathbf{r}), \tag{3.37}$$

where $G(\mathbf{r})$ is the Friedrichs mollifier satisfies normalized condition and centered at $\mathbf{r} = 0$. And $G_l(\mathbf{r}) = l^{-3}G(\mathbf{r}/l)$. Note that this filtering operation is linear and commutes with spatial and time derivatives. The residue field is the sub-grid component

$$\mathbf{a}'_l(\mathbf{x}) = \mathbf{a}(\mathbf{x}) - \bar{\mathbf{a}}_l(\mathbf{x}). \tag{3.38}$$

Applying the filtering operation to the continuity and Navier-Stokes equation, we have

$$\partial_t \bar{\rho}_l + \partial_j \overline{(\rho v_j)}_l = 0. \tag{3.39}$$

$$\partial_t \overline{(\rho v_i)}_l + \partial_j \overline{(\rho v_i v_j)}_l = -\partial_i \overline{P}_l + \partial_j \overline{\sigma_{ij}}_l + \overline{(\rho f_{\mathrm{ext},i})}_l \tag{3.40}$$

To reduce number of terms, we use the density-weighted Favre average [48], i.e.,

$$\widetilde{\mathbf{a}}_l = \frac{\overline{(\rho\mathbf{a})}_l}{\overline{\rho}_l}. \tag{3.41}$$

We will remove the subscript l from now on when there is no confusion. Then the continuity and

Navier-Stokes equation become

$$\partial_t \bar{\rho} + \partial_j(\overline{\rho}\widetilde{v_j}) = 0. \tag{3.42}$$

$$\partial_t(\overline{\rho}\widetilde{v}) + \partial_j(\overline{\rho}\widetilde{v_i}\widetilde{v_j}) = -\partial_j(\overline{\rho}\widetilde{\tau}(v_i, v_j)) - \partial_i\overline{P} + \partial_j\overline{\sigma_{ij}} + \overline{\rho}\widetilde{f}_{\text{ext},i}, \tag{3.43}$$

where $\widetilde{\tau}(v_i, v_j) = \widetilde{v_i v_j} - \widetilde{v_i}\widetilde{v_j}$ is the turbulent stress accounting for the effect from the scale smaller than l, and it is the only term couples the large scale momentum to the small scale. In addition, we can define the 2nd-order generalized central moments of any fields $f(\mathbf{x})$ and $g(\mathbf{x})$ by $\overline{\tau}(f, g) = \overline{(fg)}_l - \overline{f}_l\overline{g}_l$. Using $\overline{\tau}$ and $\widetilde{\tau}$ to describe the small-scale effect, the transport equation for large-scale kinetic energy can be written as

$$\partial_t(\overline{\rho}\frac{|\widetilde{\mathbf{v}}|^2}{2}) + \partial_j J_j = -\Pi_l - \Lambda_l + \overline{P}\partial_j\overline{\mathbf{v}}_j - D_l + \epsilon_l^{inj}, \tag{3.44}$$

where

$$\Pi_l(\mathbf{x}) = -\overline{\rho}\partial_j\overline{v}_i\widetilde{\tau}(v_i, v_j), \quad \Lambda_l(\mathbf{x}) = \frac{1}{\overline{\rho}}\partial_j\overline{P}\overline{\tau}(\rho, v_j) \tag{3.45}$$

are the subgrid scale kinetic energy flux to scales less than l,

$$D_l(\mathbf{x}) = \partial_j\widetilde{u}_i[2\mu\overline{S_{jj}} - \frac{2}{3}\mu\overline{S_{kk}}\delta_{ij}], \quad \epsilon_l^{inj}(\mathbf{x}) = \widetilde{v}_i\overline{\rho}\widetilde{f}_{\text{ext},i} \tag{3.46}$$

are the dissipation and energy injection by the external force on the large scale,

$$J(\mathbf{x}) = \overline{\rho}\frac{|\widetilde{\mathbf{v}}|^2}{2}\widetilde{v_j} + \overline{P}\overline{v}_j + \widetilde{v}_i\overline{\rho}\widetilde{\tau}(v_i, v_j) - \widetilde{v}_i\overline{\sigma}_{ij}. \tag{3.47}$$

is the large-scale transport of kinetic energy, and $-\overline{P}\partial_j\overline{v}_j$ is the large-scale pressure dilatation.

3.2.3 Scale Decomposition

The viscous range l_μ is defined as the scale at which viscous effects become significant in kinetic energy balance. In [47] it has been shown that D_l is negligible on scales $l \gg l_\mu$, and injection of kinetic energy can be localized on large scales $L \gg l$ with proper stirring. Therefore, there exists an intermediate scale $L \gg l \gg l_\mu$ where dissipation and external injection are negligible, which is the inertial range of compressible turbulence.

The subgrid scale flux terms in Eq. (3.45) transfer large-scale kinetic energy to scales smaller than l. H. Aluie argues in [49] that this subgrid scale flux cascade is localized based on empirical facts that the structure function is localized and the scalings are weak. This result has been verified by a numeric study [50]. If we use a density-weighted velocity field, the statistics of the compressible turbulence is very similar to the incompressible turbulence.

3.3 Quantum turbulence

Quantum turbulence refers to the turbulence of quantum fluid or superfluid, where the fluid is purely inviscid or mixed with some portion of viscid classical fluid. The quantum fluid in the literature emphasizes quantized vortices more than the invisicid fluid. But normally we do not distinguish them very carefully, since the quantized vortices come from the irrotational nature of superfluid.

In this section, I will first introduce the history of superfluid and theoretical models of its fluid dynamics, then discuss the energy cascade and dissipation mechanism.

3.3.1 Superfluid

The superfluid, named by Pyotr Kapitsa, was first observed by him in 1937 in liquid ^{4}He [51]. When the liquid ^{4}He is cooled below the λ point (2.17 K), he observed that the liquid could flow with no resistance through the capillaries and over the edges of containers. He also observed that a thin layer of helium below the λ point (helium II) could climb up and out of the container. Around the same time, John Allen and Don Misener observed an unusually high thermal conductivity [52]. All these observations suggest that a new state of matter was found, and Fritz London proposed that superfluidity was a quantum mechanical phenomenon related to Bose-Einstein condensation.

In 1995, the creation of Bose-Einstein condensates in dilute gases of alkali atoms provided a new system in which superfluidity could be studied [53]. However, despite the close relationship between superfluidity and Bose-Einstein condensates, they are very different ideas. Helium II superfluid can achieve a density of almost 100% superfluid with a density of less than 10% BEC. In atomic BEC, with spatial modulation of the density, the superfluid density can be much less than the BEC density. Basically, BEC is a state of matter that can be described by a condensate wave function (order parameter), but its transport behavior, which gives the superfluid density, depends on details of the spatial dependence of the wave function. This will be elaborated on in Chap. 7. But for most cases, the superfluid order parameter is equal to the BEC order parameter, and we will not emphasize their difference in this chapter.

With the BEC order parameter defined by a complex macroscopic wavefunction $\psi(\mathbf{x})$, the fluid dynamics is well described by the Gross-Pitaevskii equation [Eq. (2.57)]. By introducing the Madelung transformation $\psi = \sqrt{n}\exp(i\theta)$, we obtain a hydrodynamic description by superfluid

mass density $\rho = nm$, and velocity $\mathbf{v} = \frac{\hbar}{m}\nabla\theta$. This mapping agrees with the irrotational feature of the superfluid. Since the macroscopic wavefunction should be single valued for the space coordinate $\mathbf{x}$, the phase winding can only be multiples of 2π, that is, the circulation $\Gamma = \oint \mathbf{v} \cdot d\mathbf{l} = \kappa n$, where n is an integer and $\kappa = h/m$ is the quantized circulation. A vortex with such quantized circulation is called a quantized vortex, and any rotational motion of a superfluid can only be sustained by quantized vortices.

In the incompressible fluid section, I introduce some model of energy cascade by vortex stretching, which tries to relate the turbulence with vortices, however, numerical simulation suggests the vortex-strectching term is not dominant. And in the classical fluid the relationship between the vortices and turbulence is still unclear. However, the quantized vortex does not diffuse, since the flow is inviscid. And the core of the quantized vortex is very thin and on the scale of healing length in the system. So in quantum fluid we have a more well-defined vortex compared to classical fluid, and it might give us a better understanding of the relation between vortices and turbulence.

3.3.2 Theoretical models

3.3.2.1 Vortex filament model

The vortex filament model simplifies the description of a quantized vortex by treating it as a one-dimensional filament in a three-dimensional fluid. This filament carries circulation and is where the phase of the superfluid order parameter changes by 2π. The velocity at a point $\mathbf{r}$ due

to the presence of a filament is given by the Biot-Savart law:

$$\mathbf{v}_s(\mathbf{r}) = \frac{\kappa}{4\pi}\int_s \frac{(\mathbf{s}-\mathbf{r})\times d\mathbf{s}}{|\mathbf{s}-\mathbf{r}|^3}, \tag{3.48}$$

where $\mathbf{s}$ is the vortex line, and the integral is along the vortex line, similar to the Biot-Savart law in the magnetic field calculation. The rest of the superfluid is considered incompressible and irrotational, with the exception of these filaments.

A simplification of the Biot-Savart law is to decompose the filament dynamics into local and nonlocal parts, and the nonlocal part is ignored assuming the local part dominates, which is called the local induction approximation (LIA). Schwartz [54] shows that the motion of the filament is perpendicular to its tangential $\mathbf{s}'$ and curvature $\mathbf{s}''$ direction, where the prime stands for the diffentiation with respect to the one-dimensional coordinate ε is we use the parametric form $\mathbf{s}(\varepsilon, t)$, i.e.,

$$\dot{\mathbf{s}} = \frac{\kappa}{4\pi}\mathbf{s}'\times\mathbf{s}''\ln\left(\frac{2(l_+l_-)^{1/2}}{e^{1/4}a_0}\right), \tag{3.49}$$

where a_0 is the vortex core size, and l_+ and l_- are the lengths of the two adjacent line elements after segmentation. As we can see, the motion is along the binormal direction $\mathbf{s}'\times\mathbf{s}''$ which explains the helical oscillation pattern of the vortex line (Kelvin waves) as a steady-state solution. LIA is a good approximation for single vortex, for dynamics related to many vortices such as vortex reconnection, the nonlocal term needs to be considered carefully.

The vortex filament model can also be extended to the finite-temperature case where normal fluid is present. It is a good model for understanding the vortex motion, but it is not precise enough for multiple vortices dynamics.

3.3.2.2 The Gross-Pitaevskii model

Using hydrodnamical picture, the GPE becomes quantum Euler equation

$$\partial_t \rho + \nabla \cdot (\rho \mathbf{v}) = 0, \tag{3.50}$$

$$\partial_t (\rho \mathbf{v}) + \nabla \cdot (\rho \mathbf{v}\mathbf{v} + P\mathbf{I} - \mathbf{\Sigma}) = \rho \mathbf{f}, \tag{3.51}$$

where $\mathbf{I}$ is the unit tensor, $\mathbf{f} = -\nabla V_{\text{ext}}$ is the externel force, and $P = g\rho^2/(2m^2)$ is the pressure, and $\mathbf{\Sigma}$ is the quantum stress, i.e.,

$$\mathbf{\Sigma} = \frac{\hbar^2}{4m^2}\nabla^2\rho\mathbf{I} - \frac{\hbar^2}{m^2}\nabla\sqrt{\rho}\nabla\sqrt{\rho}. \tag{3.52}$$

It is obvious that this set of equations is dissipationless, which agrees with the observation that the superfluid is inviscid.

However, experimental results have revealed that the quantum turbulence agrees with the Kolmogorov spectrum, where dissipation is required to balance the large-scale energy injection, so that the kinetic energy can cascade from large to small scale. The dissipation mechanism in a quantum fluid is in debate, but we can conclude that there must be an inertial range where the energy injection and dissipation are negligible. Typically, quantum turbulence has three main characteristic length scales: the length scale L of energy injection by external stirring, which is often approximated by the size of the system, the mean distance between the vortex l_i, and the radius of the vortex core ϵ determined by the healing length of the quantum fluid. The Richardson cascade is dominated on the scale $L \gg l \gg l_i$ with the exponent $E(k) \propto k^{-5/3}$, and an additional

cascade is believed to be in between the l_i and ϵ by Kelvin waves, which is the vibration of the vortex lines excited by vortex reconnection.

Using the coarse graining method in the section of compressible turbulence, we can again decompose scales and discuss the energy cascade in the inertial range.

3.3.3 Coarse Graining and Richardson Energy cascade

Using the same notation system as the compressible fluid, the coarse grained quantum Euler equation [55] becomes

$$\partial_t \overline{\rho} + \nabla \cdot (\overline{\rho}\widetilde{\mathbf{v}}) = 0, \tag{3.53}$$

$$\overline{\rho}(\partial_t + \widetilde{\mathbf{v}} \cdot \nabla)\widetilde{\mathbf{v}} + \nabla \cdot (\overline{\rho}\widetilde{\tau}(\mathbf{v}, \mathbf{v})) = -\nabla \overline{P} + \nabla \cdot \overline{\mathbf{\Sigma}} + \overline{\rho}\widetilde{\mathbf{f}}. \tag{3.54}$$

We can further apply the coarse graining to the kinetic energy budget equation

$$\partial_t \frac{1}{2}\rho|\mathbf{v}|^2 + \nabla \cdot \left[(\frac{1}{2}\rho|\mathbf{v}|^2 + P)\mathbf{v} - \mathbf{\Sigma} \cdot \mathbf{v}\right] = P\nabla \cdot \mathbf{v} - \mathbf{\Sigma} : \nabla \mathbf{v} + \rho \mathbf{v} \cdot \mathbf{f}, \tag{3.55}$$

where the ":" stands for the double index contraction by $\mathbf{A} : \mathbf{B} = A_{ij}B_{ij}$, and obtain the large-scale kinetic energy budget equation

$$\partial_t (\frac{1}{2}\overline{\rho}|\widetilde{\mathbf{v}}|^2) + \nabla \cdot \mathbf{J} = \overline{P}\nabla \cdot \widetilde{\mathbf{v}} - \overline{\mathbf{\Sigma}} : \nabla \overline{\mathbf{v}} - \Pi_l - \Lambda_l + \epsilon_l, \tag{3.56}$$

where

$$\mathbf{J} = (\frac{1}{2}\overline{\rho}|\widetilde{\mathbf{v}}|^2 + \overline{P})\widetilde{\mathbf{v}} + \overline{\rho}\widetilde{\mathbf{v}} \cdot \widetilde{\tau}(\mathbf{v}, \mathbf{v}) - \frac{\overline{P}}{\overline{\rho}}\overline{\tau}(\rho, \mathbf{v}) - \overline{\mathbf{\Sigma}} \cdot \widetilde{\mathbf{v}} + \frac{\overline{\mathbf{\Sigma}}}{\overline{\rho}} \cdot \overline{\tau}(\rho, \mathbf{v}), \tag{3.57}$$

$$\epsilon_l = \overline{\rho}\widetilde{\mathbf{v}} \cdot \widetilde{\mathbf{f}}, \tag{3.58}$$

$$\Pi_l = -\overline{\rho}\nabla\widetilde{\mathbf{v}} : \widetilde{\tau}(\mathbf{v}, \mathbf{v}), \tag{3.59}$$

$$\Lambda_l = \frac{\nabla\overline{P}}{\overline{\rho}} \cdot \overline{\tau}(\rho, \mathbf{v}) - \frac{1}{\overline{\rho}}\nabla \cdot \overline{\mathbf{\Sigma}} \cdot \overline{\tau}(\rho, \mathbf{v}). \tag{3.60}$$

The spatial transport term does not contribute to the cascade since it vanishes at the boundary. Again, the energy injection is localized to large scale L, so $\overline{\tau}(\mathbf{v}, \mathbf{f})$ has been neglected. The term related to the subscale is the subscale grid flux term $\Pi_l + \Lambda_l$, which is quite similar to the classical compressible turbulence. Notice that the dissipation term is not here, but to reach a fully developed turbulence, an empirical small-scale dissipation D_l is required. Then there is no reason to expect a cascade different from the Richardson cascade in a classical fluid. The remaining question is how to study the range it holds. T. Tanogami [55] estimates the crossover scale by balancing momentum flux $\rho\mathbf{v}\mathbf{v}$ and quantum stress $\mathbf{\Sigma}$, which gives $\lambda \approx \kappa/v_{rms} \approx l_i$, where $\kappa = h/m$ is the quantum circulation.

3.3.4 Dissipation mechanism

In the coarse-grained scheme, we have seen that the Richardson cascade in quantum fluid should be similar to the classical turbulence. However, we do not have a good understanding of the dissipation mechanism. What we can know from the experimental result is that the dissipation has to be on the small scale; otherwise, we should not observe the Richardson cascade. I will introduce some candidates for the dissipation mechanism in the quantum turbulence community.

3.3.4.1 Kelvin wave and Kelvin Cascade

Kelvin waves are defined as helical displacements of a rectlinear vortex line propogating along the core. It originates from vortex reconnection, where the tips of the crossing point, similar

to the bending point of a plucked string, can relax into vibrations along its new vortex core. An approximate dispersion relation for the inviscid fluid is given in [56]

$$\omega = \frac{\kappa k^2}{4\pi}\left[\ln\left(\frac{1}{ka_0}\right) + c\right], \tag{3.61}$$

where a_0 is the vortex core parameter and $c \sim 1$. It is worth to note that the Kelvin wave only survives in superfluid, and it is damped by mutual friction when the normal fluid is around. At high k, the Kelvin wave is unstable and some other type of quasiparticles (phonons) will be radiated. This can be seen as a dissipation mechanism for incompressible kinetic energy, since phonons contribute to compressible kinetic energy. So the whole picture of the Kevin wave related dissipation can be summarized as: low k Kelvin wave forms by vortex reconnection, then the Kelvin wave cascades from low k to high k due to nonlinear interaction, and finally is radiated to phonons at high k. In this way, the system's incompressible kinetic energy (vortices) transforms to the compressible kinetic energy (phonons). In superfluid helium, the phonons can leave the system by interacting with the container wall. In an atomic BEC, the phonon cannot leave the system by colliding with the container wall because the wall is made up of the optical potential as a rigid body. However, the wall depth of the container is typically on the order of the chemical potential, so the phonon can leave similarly to pouring out of the boundary.

3.3.4.2 Friction from Normal Fluid

The Kelvin wave cascade model describes the dissipation mechanism at zero temperature, when the normal fluid is negligible in the system. However, realistically, turbulence is far from equilibrium, vortices and phonons are all over the system. When these excitations are no longer

coherent, we can treat them as a normal fluid with viscosity, which can exert frictional force on the vortices and the Kelvin wave. The interaction between normal fluid and superfluid is far from trivial and requires detailed modeling, which is part of the reason the scaling prediction of the Kelvin wave cascade is different from model to model.

3.3.5 Quantum Turbulence Experiments

Earlier quantum turbulence mainly focuses on the thermal counterflow of the two-fluid, since it is a unique phenomenon in a quantum fluid. The experimentalist touches on the energy spectra and velocity structure function type of statistics since the mid 1990s. Later on the turbulence experiments in atomic BEC started around 2009, and a scaling law was found in 2016. I will summarize these cornerstone experimental results.

3.3.5.1 Quantum turbulence experiments in ^{4}He

Kolmogorov spectrum in superfluid ^{4}He In 1998 Maurer and Tabeling [57] confirmed the Kolmogorov spectrum in superfluid ^{4}He turbulence for the first time. Using total-head tube coupled to a piezoelectric quartz, the authors measured the pressure time traces of the turbulent flow excited by two counter-rotating disks. The authors then mapped the pressure fluctuation to the velocity fluctuation and observed the energy spectra for turbulent He4 under three different temperatures 2.3, 2.08, and 1.4K. The Kolmogorov spectrm ($E(k) \sim k^{-5/3}$) are observed for all three cases independently of the superfluid fraction. Also, the intermittency effect is observed from the PDF of the velocity increments with different time separations at 1.4K.

Decay grid turbulence experiments in ^{4}He Oregon group developed a gird turbulence setup for superfluid ^{4}He [58]. An upward moving grid is used to excite the turbulence, and vorticity ω is measured by a second sound transducer assuming the vorticity is proportional to the second sound attenuation coefficient based on [59]. In classical turbulence the energy dissipation rate $\epsilon = \nu\langle\omega^2\rangle$. The authors assumed that this relation holds for ^{4}He if we replace the vorticity by the quantum ciculation times the vortex line length L, i.e. $\epsilon = \nu'\kappa^2 L^2$, where ν' is the effective kinematic viscosity. The authors observed the decay of the vorticity (κL) following $t^{-3/2}$ [22]. This relation agrees with the Kolmogorov exponent $2/3$ for the dissipate rate ϵ, i.e. the total energy is $E \propto \epsilon^{2/3}$, and for the decay turbulence $\epsilon = -dE/dt \propto -\epsilon^{-1/3}d\epsilon/dt$, so we have $\epsilon \propto t^{-3}$ and finally agrees with the experimental result $L \propto t^{-3/2}$.

Velocimetry and visualization in ^{4}He Maryland group first observed the quantized vortex by injecting less than 10% hydrogen particles as tracers of the motion of ^{4}He [60]. The tracer particles were illuminated by an argon-ion laser sheet for imaging. Using this technique, the Maryland group observed non-Gaussian PDF of the velocity field, which is largely related to quantum vortices, so it is able to resolve the velocity field up to vortice core size [61]. Kelvin wave and vortex reconnection were also observed using the same technique [62].

3.3.5.2 Quantum turbulence experiments in Atomic BEC

Quantum turbulence of atomic BEC in harmonic trap Sao Carlos group first observed vortex tangles in a 3D harmonic trapped BEC by a combination of rotation and shaking of the trap in 2009 [11], which is the first evidence of quantum turbulence in BEC. During the free expansion of the gas, they observed a self-similar expansion, i.e. the momentum distribution has a similar

aspect ratio of the density in-situ aspect ratio before expansion, which is opposite to the result in typical trapped BEC in the ground state. A power law is found for the momentum distribution $n(k) \propto k^{-2.9}$ [17], however, it is difficult to compare the result with the Kolmogorov scaling, since the gas is inhomogeneous and the velocity field is difficult to extract.

Quantum turbulence of atomic BEC in optical boxes Cambridge group used a spatial light modulator to create a homogeneous box-trapped BEC, which is a great platform to study homogeneous turbulence. Turbulence was created by shaking the box potential and the momentum distribution of the turbulent cloud was observed by free expansion [12]. However, the observed scaling $n(k) \propto k^{-3.5}$ is different from the Kolmogorov exponent, and the authors claimed that the turbulence they observed is more closely related to wave turbulence where the phonons' motion dominates over vortices.

3.3.5.3 Summary

As you can tell, the quantum turbulence experiments in the atomic BEC and superfluid ^{4}He are very different. The latter is more closely related to the classical turbulence study, measuring statistics of the turbulent flow by direct or indirect sensor of the velocity field. However, the atomic BEC turbulence studies only measure the momentum distribution of the whole cloud, losing the spatial correlation information due to lack of methods to extract the velocity field, which is the core physical quantity to measure and study in a turbulent flow. So it is tough to compare the experimental result with other fluids and with the classic physical laws such as the Kolmogorov law.

3.4 Velocimetry

In this section I will introduce the velocity measurement techniques both in classical fluid and quantum fluid. Velocimetry techniques are divided into intrusive and non-intrusive, and the latter is emphasized since it is a weak measurement with limited impact on the system during measurement.

3.4.1 Velocimtery in classical fluid

3.4.1.1 Intrusive Velocimetry

Pitot Tube The Pitot tube measures the velocity of fluid flow by converting the kinetic energy of the flow into potential energy. Note that this potential energy is the pressure energy not the gravity potential energy. A standard Pitot tube consists of two concentric tubes. The inner tube has an opening facing the fluid flow and measures the total (stagnation) pressure P_{tot}, while the outer tube, often with side holes, measures the static pressure P_{static} of the fluid. As the fluid enters the front of the Pitot tube, it comes to a halt (stagnation). The pressure at this point is the highest and is known as the stagnation pressure. The difference between this stagnation pressure and the static pressure gives a measure of the fluid's dynamic pressure, which can be used to calculate the fluid's velocity by

$$v = \sqrt{\frac{2(P_{tot} - P_{static})}{\rho}}. \tag{3.62}$$

Pitot tube is largely used in velocimtry of incompressible fluid, and it is worth noting that

the first energy spectrum experiment of quantum turbulence uses the Pitot tube as a probe for velocity fluctuation over time.

Hot Wire Anemometer A hot wire anemometer is an instrument commonly used for measuring the velocity of a fluid, particularly air [63]. The core of the device is a very thin wire (the "hot wire") heated to a temperature above the ambient temperature of the fluid. This wire is typically made of materials such as platinum or tungsten because of their stability and high melting points. When the fluid (like air) flows through the heated wire, it cools the wire down. The cooling rate depends on the velocity of the air; faster air flow results in more cooling, which leads to a resistance change that can be precisely measured from the voltage drop E across the hot wire. The relation between the velocity and the voltage drop needs calibration to the King's law:

$$E^2 = A + Bv^n, \tag{3.63}$$

where A, B and n are constants determined from calibration. The power n is typically close to 0.5 for laminar flow and close to 0.45 for turbulent flow.

3.4.1.2 Non-intrusive Velocimetry

Laser Doppler Velocimetry Laser Doppler Velocimetry (LDV) [64], also known as Laser Doppler Anemometry (LDA), is a technique used to measure the velocity of a fluid using the Doppler effect of laser light. LDV is based on the Doppler effect, which occurs when the frequency of a wave changes due to the relative motion between the source of the wave and the observer. It typically runs with two coherent lasers with the same frequency, intersecting at an interested

region for velocimetry. The tracer particles, when moving across the interference pattern, scatter photons in a period $T = \lambda/(2\sin\theta v)$, where λ is the wavelength of the incident laser, and θ is the angle between two beams, v is the velocity perpendicular to the fringe pattern. A photodetector can be used to record the scattering events for velocimetry.

Particle Image Velocimetry Particle Image Velocimetry (PIV) is an optical method of flow visualization that is used in research and engineering to obtain velocity measurements and related properties in fluids [65]. The fluid is seeded with tracer particles, which are typically small enough to faithfully follow the fluid flow dynamics without affecting them. The seeded flow is illuminated with a light source, typically shaped into a sheet that illuminates a plane of the fluid flow. A camera (or multiple cameras for 3D PIV) captures images of the illuminated particles at two or more instances in time. Images can be split into segments where the cross-correlation of the same segment of different images is calculated, where the peak of the cross-correlation gives the relative displacement Δx of two images within the time interval Δt of two adjacent images. The velocity of that segment is given by $v = \Delta x/\Delta t$, and applying this technique to all segments gives a velocity field of the fluid.

Laser Speckle Velocimetry Laser Speckle Velocimetry (LSV) [66] is another optical technique used to measure the velocity of a fluid flow, similar in some respects to PIV but with distinct differences. It is particularly useful in situations where seeding the flow with particles (as in PIV) is impractical or impossible. Speckles are random interference patterns produced by the scattering of coherent light (like laser light) from a rough surface or in a medium with scattering particles. In fluid dynamics, these naturally occurring speckles in the fluid are used instead of

artificially introduced tracer particles. The fluid flow is illuminated with a laser, and the scattered light, which forms the speckle pattern, is captured using a camera. As the fluid moves, the speckle pattern changes, providing information about the fluid's motion. Similar to PIV, cross-correlation techniques are used to analyze the changes in the speckle pattern between images. The average displacement of the speckle pattern in each interrogation region is used to calculate the velocity field.

3.4.2 Velocimetry in cold gases

3.4.2.1 Time-of-flight measurements

Time-of-Flight (ToF) measurement is a fundamental technique widely used in the field of cold atom physics. This technique involves releasing a cloud of ultra-cold atoms from a trap, such as a magnetic or optical trap, and allowing them to freely expand. Since the gas is typically dilute, we neglect the collision between atoms and during free expansion besides the gravitational accleration it moves with its original velocity. So if we allow the atoms to expand for long time such that its initial position difference is negligible, its positonal distribution gives the momentum (velocity) distribution of the cloud before expansion.

ToF gives the velocity distribution of the whole cloud but loses the velocity field information, so it is not ideal to study turbulence since it cannot give the spatial correlation of the velocity field. Previous quantum turbulence experiments of quantum gases mainly use ToF to measure $n(k)$ and write the energy spectrum as $E(k) = n(k)\hbar^2k^2/2m$. This indirect measurement needs a very long free expansion time up to 100 ms to resolve the large k in the inertial range. This is typically difficult to do for cold atom experiments since under free fall it will collide with the boundary of

the ultra high vacuum system; therefore, an additional magnetic field is applied to compensate gravity, but the magnetic field will also reshape the $n(k)$. So far no observed energy spectrum from ToF shows evidence of Kolmogorov scaling law.

3.4.2.2 Light dragging effect velocimetry

The light dragging effect [67, 68], a phenomenon historically rooted in the early studies of ether and first observed by Fizeau in his flowing-water experiment, has evolved to play a critical role in modern velocimetry techniques. The essence of the light-dragging effect, as depicted in Fizeau's experiment, lies in the interaction of light with a moving medium and how this movement alters the light's propagation. However, the medium has to be moved relatively on the order of speed of light to observe a measurable dragging; thereby it is unrealistic until the development of slow light, where the group velocity of the light can be slowed down to mm/s or even stopped. Therefore, the drag of a moving medium becomes obvious.

I will briefly introduce the principle of light dragging.

Light dragging effect The light-dragging effect can be understood from the special relativity. We consider the case in the following figure. The incident light is dragged in the medium moving vertically with velocity v, the medium length is L, and the distance dragged is Δx.

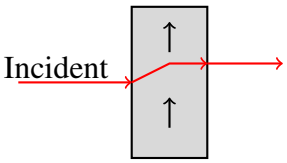

Figure 3.2: Illustration of the light dragging effect in a moving medium with vertical motion.

The walk off angle inside the medium is given by [69]

$$\tan\theta = \frac{\Delta x}{L} = \frac{v}{c}(\frac{c}{v_g} - \frac{v_p}{c}), \tag{3.64}$$

where v_g and v_p are the group and phase velocity determined by the relative dielectric constant ϵ_r

$$v_g = \frac{c}{\sqrt{\epsilon_r(\omega_0)} + \frac{\omega_0}{2\sqrt{\epsilon_r(\omega_0)}\frac{d\epsilon_r}{d\omega}|_{\omega_0}}}, \quad v_p = \frac{c}{\sqrt{\epsilon_r\omega_0}}. \tag{3.65}$$

The dragging can be largely amplified for highly dispersive media. In atomic physics, it could be realized by the electromagnetically induced transparency (EIT), where the group velocity of light can be slowed down.

Using this effect, the center of mass motion has been measured by [70], but it has not been applied to velocity field measurement. In principle, using a structured light pattern and analysis with cross-correlation, it might be possible to extract the velocity field.

3.4.2.3 Raman Velocimetry

Raman velocimetry in cold atom experiments utilizes the Raman scattering process to measure the velocity of atoms [71]. In a typical setup, two laser beams with slightly different frequencies are directed at the cloud of cold atoms. These beams are tuned close to an atomic resonance, facilitating a two-photon Raman transition. In this process, an atom absorbs a photon from one laser and then emits a photon into the other, effectively undergoing a transition between two different internal states. This transition is accompanied by a change in the atom's momentum as a result of the photon recoil.

The frequency difference between the two lasers is set to match the energy difference between the two internal states of the atom, plus or minus the kinetic energy associated with the atom's motion. By carefully tuning the frequency difference of the lasers, one can selectively address atoms moving at specific velocities.

The outcome of a Raman velocimetry experiment is often a velocity-sensitive population transfer between the atomic states, which can be detected and analyzed. By scanning the frequency difference between the two lasers, we can construct a velocity distribution of the atomic cloud. However, the measured velocity is still not the velocity field required for turbulence study.

Chapter 4: The RbRb apparatus

This chapter introduces the apparatus for BEC production, in which the vaccum system, optical system, and the magnetic field control in the lab is discussed in detail. The chapter is ended with a brief introduction of digital micromirror device which is closed related to the PIV for velocity field measurement in Chap. 5.

4.1 Experimental Layout

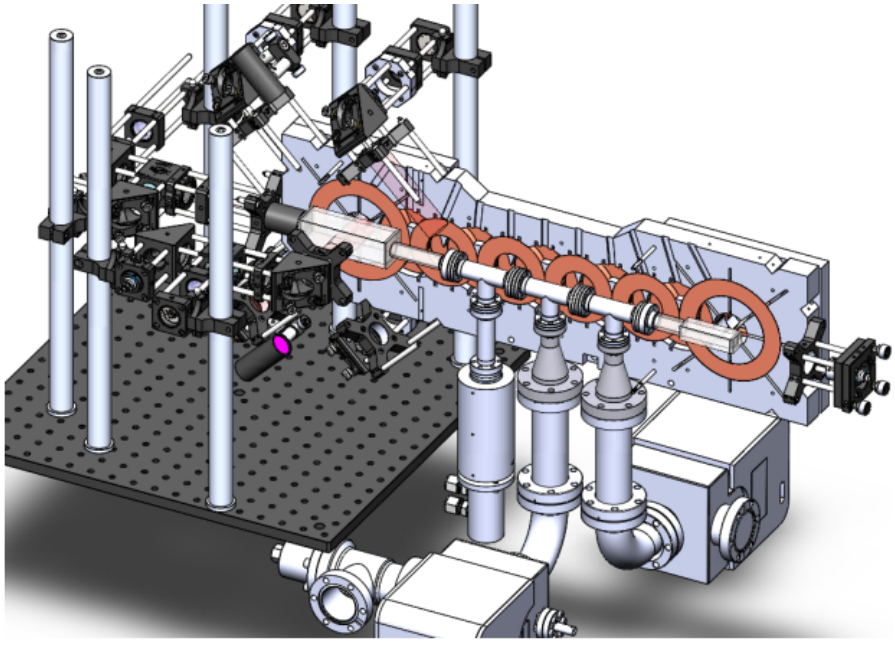

Figure 4.1: The RbRb apparatus. Reproduced from [1]. For clarity the science cell optics is not shown here, and only half of the transport coils are shown.

Figure 4.1 illustrates the apparatus used for Bose-Einstein Condensate (BEC) production.

The setup comprises two primary glass cells: the Magneto-Optical Trap (MOT) cell on the left and the science cell on the right. The MOT cell is where atoms are initially captured and subjected to laser cooling. The science cell, designed with a smaller volume, facilitates closer observation of atoms through microscopes with high numerical aperture and serves as the primary zone for conducting scientific experiments. Both cells, along with the atom source, are integrated into an ultra-high vacuum system, maintained by two ion pumps.

The surrounding optics, partially depicted in Fig. 4.1, are primarily dedicated to laser cooling in the MOT cell. However, to accommodate additional optical axes for scientific research, atoms are magnetically transferred from the MOT cell to the science cell using the surrounding coil system.

The apparatus is essentially a tripartite system, encompassing the vacuum system, optics system, and magnetic field control system. Each component is pivotal to the apparatus's functionality and will be discussed in detail in this chapter.

Concluding the experimental layout, a typical experimental sequence to produce BEC in RbRb involves several key steps. Initially, the MOT cell undergoes MOT loading for 2 to 6 seconds, followed by a brief laser cooling phase lasting less than 1 second. Subsequently, atoms are magnetically trapped and transported to the science cell within 2 seconds. Once in the science cell, RF or microwave evaporation occurs over 4 to 6 seconds, followed by the loading of atoms into the dipole trap. The final stage, dipole evaporation, takes place over 10 seconds, culminating in the achievement of BEC. Overall, the entire experimental sequence to produce BEC spans approximately 20 to 25 seconds.

4.2 Vacuum system

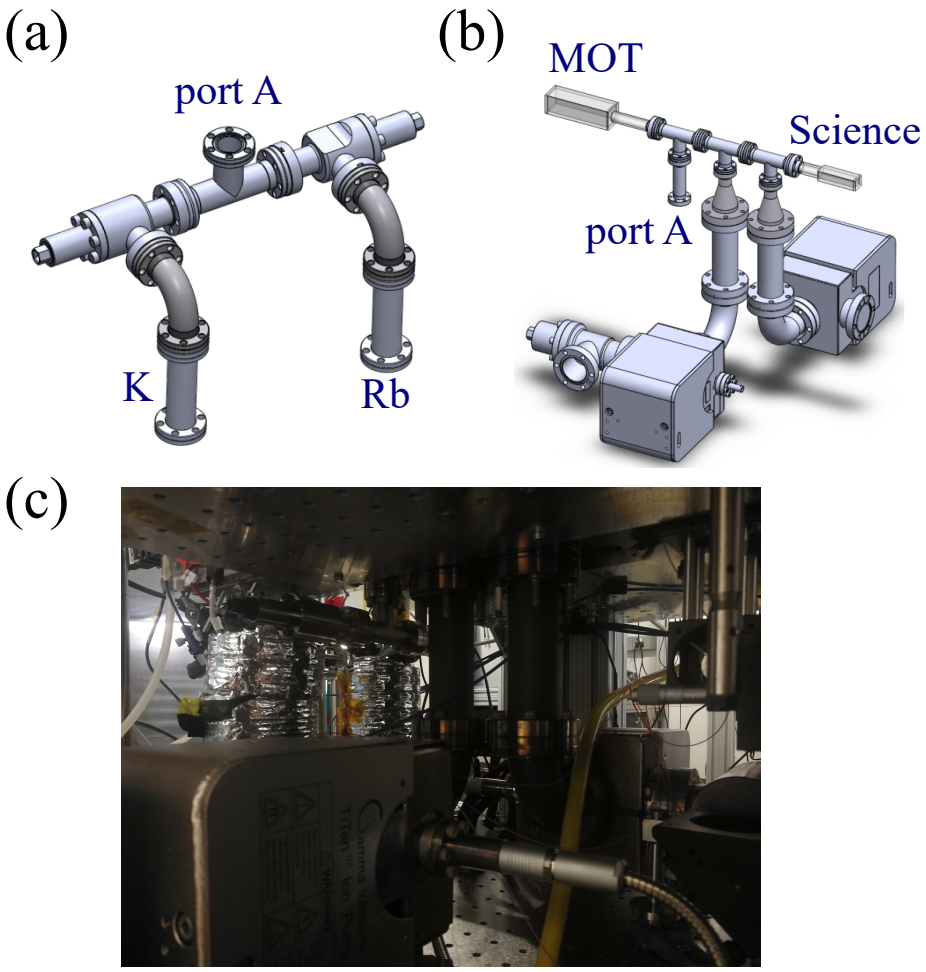

Figure 4.2: The RbRb vacuum chamber. (a), (b) are reproduced from [1]. (c) shows the physical vacuum chamber.

Fig. 4.2 shows the vacuum system, in which (a) depicts the atom source. In the vacuum system, we placed two species of alkali metals Rb and K stored in ampules before bake. They are placed on different sides of the vacuum chamber, and a Tee is used to combine them to port A. As shown in Fig. 4.2(b), two ion pumps are placed between the MOT cell and the science cell to achieve high vacuum, and a differential pumping tube is placed inside the system to let the science cell have a lower pressure than the MOT cell.

4.2.1 Vacuum bakeout

To achieve ultrahigh vacuum (UHV)[1], it's necessary to bake out the system to degas the molecules inside the metal. Baking is time-consuming and typically takes several months to achieve UHV. To accelerate the degassing, it would be better to bake at high temperatures such as $450°$C, however, some vacuum parts do not allow us to do so. The ion pump cannot resist bakeout temperatures higher than $350°$C, and the glass cell has an even lower bakeout temperature limit, i.e. $250°$C.

So we did a three-time bake. (i) Bake all vacuum parts under $450°$C without assembling and pumping with a turbo pump. (ii) Assemble the vacuum chamber except for the atom source and the glass cell, and bake under $350°$C with a turbo pump and the two ion pumps. (iii) Assemble the atom source ampules and glass cell to achieve a complete vacuum assembly and bake under $250°$C with a turbo pump and the two ion pumps.

For (ii) and (iii), as shown in Fig. 4.3(a) we wrapped the whole vacuum system in UHV aluminum foils and attached heat ropes to the foils. Initially, only the turbo pump is on and the ion pump is on when the pressure is below 10^{-5} Torr.

Bakeout sometimes ends in a pressure plateau where the pressure does not decrease over time, which suggests the existence of leakage in the system, so adding a residual gas analyzer (RGA) for leakage checking is recommended.

[1] Actually the UHV standard in the lab is pretty simple, i.e., the ion pump current reading should be 0, A, which corresponds to a pressure less than 10^{-10} Torr

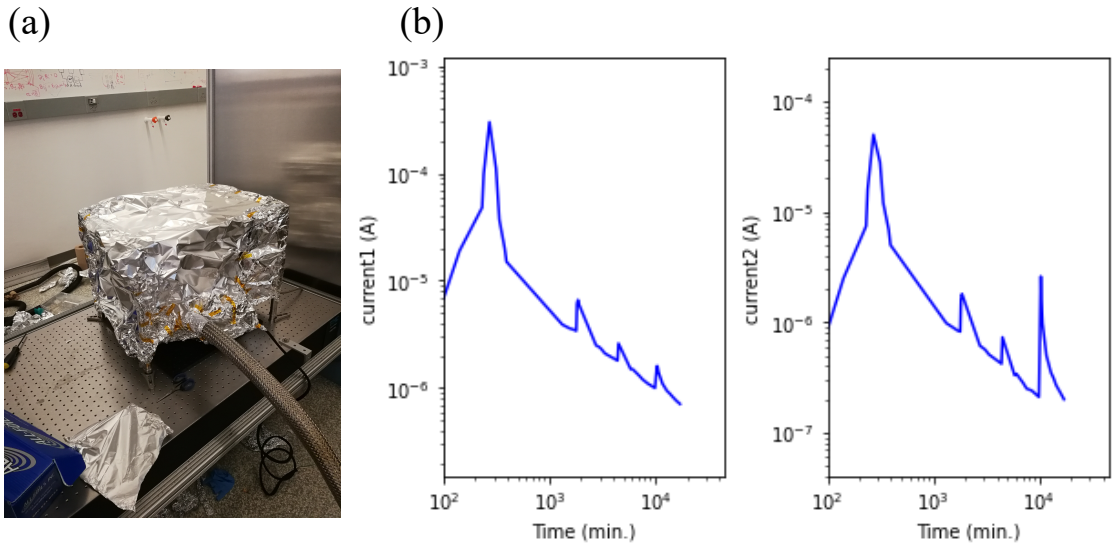

Figure 4.3: (a) shows the bakeout technique we use, in which the bellow is connected to a turbo pump, and the vacuum system is wrapped by the UHV aluminum foils. (b) shows a typical bakeout log. The current reading is from two ion pumps and the spikes are temperature sudden increasing of the baking during the process.

4.2.2 Atom source control

After UHV was achieved, we cracked the ampule and released the atoms. Unlike other systems with Zeeman slowers which typically heat the atoms source so that the atom background density is quite high, we set the Rb source temperature to $0°$C by a thermoelectric cooler (TEC) cooled by a metal piece with water running inside, and the source is wrapped by thermal blanket, as can be seen in Fig. 4.2(c). To avoid ice being frozen on the atomic source chamber, we flush the system with room-temperature nitrogen.

It is worth noting that the melting temperature of Rb is $39°$C, so the metal is in the solid phase at $0°$C, but there is still vapor with pressure P given by Eq. (4.1) [28], which is enough for the cold atom experiments.

$$\log_{10} P = -94.048 - \frac{1961.258}{T} - 0.038T + 42.575 \log_{10} T. \tag{4.1}$$

In the first few weeks after achieving UHV, to accelerate the whole system to reach an equilibrium, [2] we heat the source above the melting point for 20 minutes per day. Fluorescence is only observable after several weeks with the aid of periodic external heating.

Ultraviolet light (UV) is reported to reduce the portion of alkali atoms attached to the glass cell [1], we tried adding UV to the system during MOT loading but found no difference, which is still a mystery to this lab.

K atom source is typically controlled at room temperature $20°$C, but we never use that since we don't have lasers for K yet.

4.3 Experimental optical setups

Our laser system consists of three distinct lasers: the master laser, the cooling laser, and the repump laser. For effective laser cooling, precise dynamic control over the frequencies of the cooling and repump lasers is crucial. This precision is achieved by locking these lasers to a stable, known frequency, which is provided by the master laser. The master laser itself is stabilized by locking it to a specific atomic spectral line, ensuring a high degree of frequency stability and accuracy.

This section will first introduce the configuration of the MOT optics surrounding the MOT cell. Subsequently, we will delve into the details of the laser control and locking mechanisms, encompassing the master, cooling, and repump lasers.

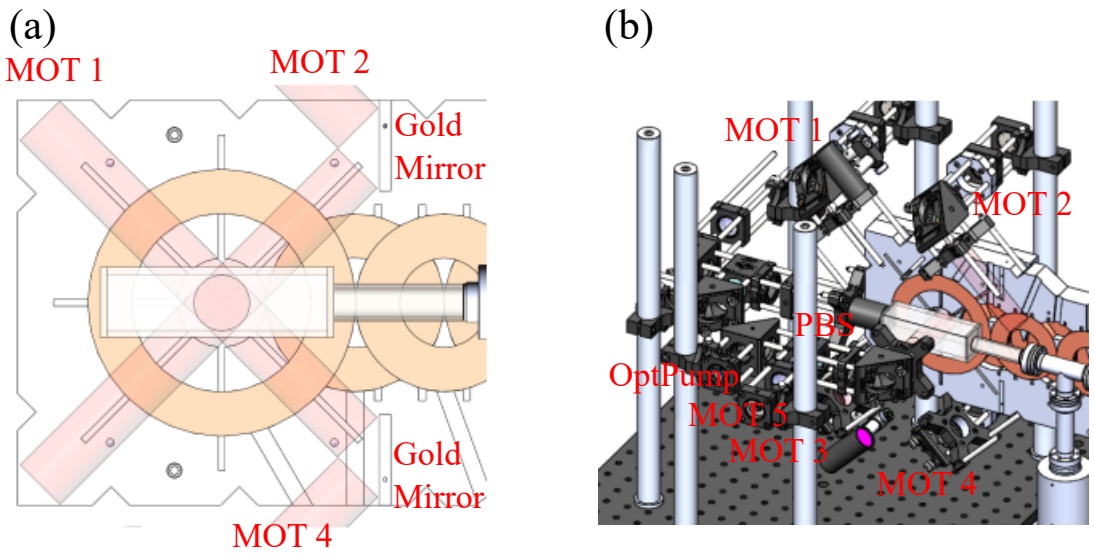

Figure 4.4: MOT optics. Reproduced from [1]. (a) Three pairs of beams that form the MOT region within the glass cell. The pair that goes in and out of the plane is not labeled in (a). In (b), MOT5 is labeled, and MOT6 is hidden behind the coils. In (b) an additional optical pumping beam labeled by OptPump has orthogonal polarization to the MOT5.

4.3.1 MOT optics geometry

The 3D MOT requires 6 cooling beams, as shown in Fig. 4.4, realized by a cage mount system attached to the coil holder. All the beams are tuned to circular polarized and two gold mirrors are used to preserve the polarization of the reflecting beams. Repump beams are sent in from MOT1 and MOT4. The optical pumping beam is propogated along MOT5 but with a polarization orthogonal to the MOT5.

4.3.2 Laser Control

In our lab we use hyperfine levels of ^{85}Rb and ^{87}Rb for laser control. The laser frequencies used are summarized in the following diagram, and the details will be elaborated in this section.

[2]In other words, we want more atoms to accumulate in the glass cell for experiments.

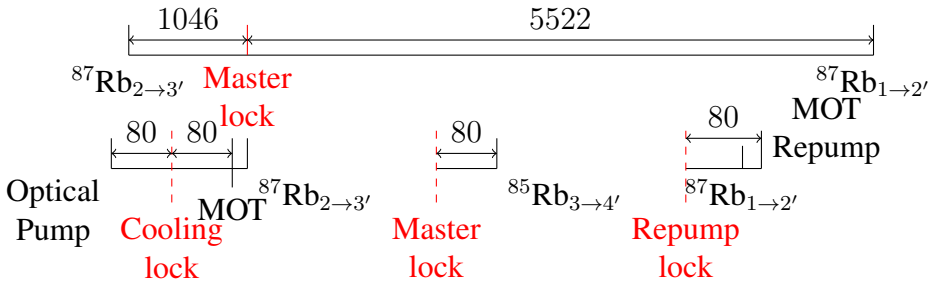

Figure 4.5: Laser frequency diagram. The unit is in MHz. The first row shows the frequency rough difference of the cooling, master, and repump laser. The second row gives detailed beam frequencies relative to the lock.

4.3.2.1 Master Laser

To achieve laser cooling, the frequency of the laser needs to be stabilized and can be controlled with high bandwidth. The cooling and repump lasers have to be locked to a frequency standard, in our lab we call it the master laser, which uses saturated absorption spectroscopy (SatAbs) of ^{85}Rb, shown in Fig. 4.6.

SatAbs can resolve frequency within the natural linewidth (6 MHz for Rb) among the Doppler-broadened absorption spectrum by a pump beam (pink in Fig. 4.6) that pumps some of the atoms from the ground to excited states so that the probe beam (red in Fig. 4.6) absorption efficiency will be reduced when the probe beam is resonant to the excited atoms which is a spike in the absorption spectrum.

In our setup, the pump and probe beam have a frequency difference of 160 MHz due to double passing of a 80 MHz AOM, $\nu_{pump} - \nu_{probe} = 160\,\text{MHz}$. We lock to the ^{85}Rb $F = 3 \to F' = 4$ transition with frequency $\nu_{3\to4}$, since the pump and probe beams counterpropagate with nonzero frequency difference, additionaly we have to take into account the Doppler shift kv, that is, $\nu_{pump} = \nu_{3\to4} + kv$ and $\nu_{probe} = \nu_{3\to4} - kv$. So, the Doppler shift is 80 MHz, and the beam sent

to the beatnote lock has the same frequency as the probe beam, that is, $\nu_{master} = \nu_{3\to4} - 80\,\text{MHz}$ = 384229161 MHz.

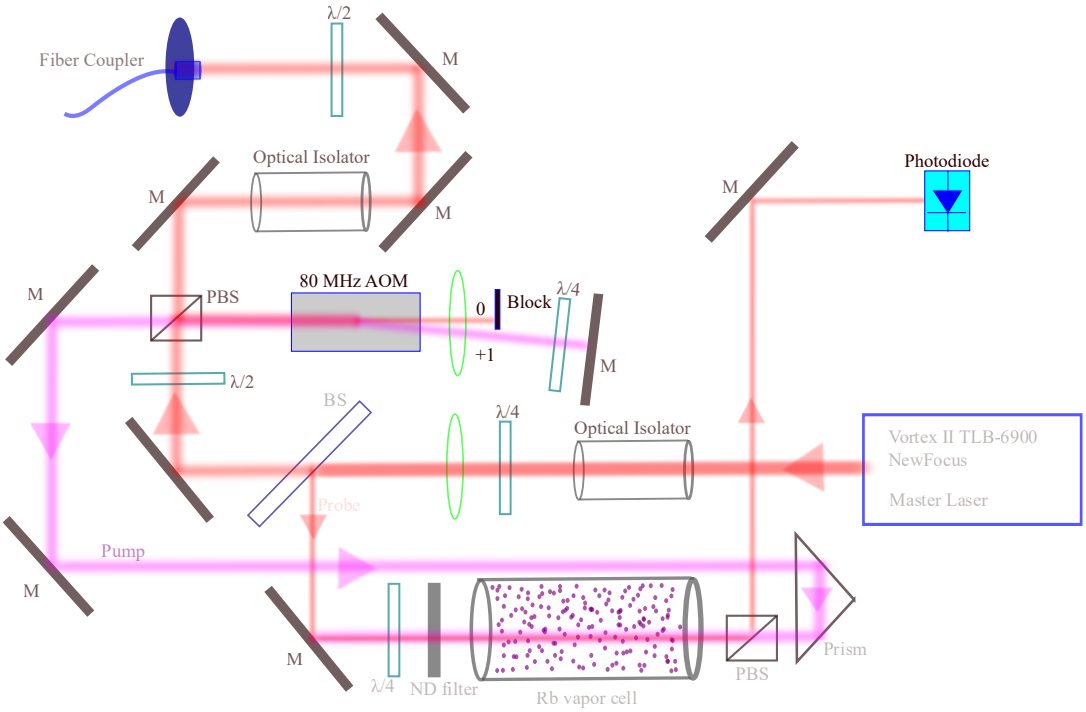

Figure 4.6: Master Laser SatAbs configuration.

4.3.2.2 Cooling Laser

The cooling laser setup is shown in Fig. 4.7, where 5 fiber output ports are used for beatnote lock, probes on science side, MOT and molasses cooling and optical pumping, respectively.

A taper amplifier is used to amplify the light from 30 mW to 700 mW for the MOT beam, which couples into a 2×6 fiber splitter and the maximum output power on each MOT arm is 30 mW. An additional $\lambda/4$ waveplate is placed before the MOT cooling port for polarization control.

The cooling laser is locked close to the ^{87}Rb $F = 2 \to F' = 3$ transition through the beatnote lock. The locked frequency can be dynamically tuned within each sequence, for

example, cooling laser frequencies in a typical BEC experiment are shown in the following table, where the cooling detuning δ is relative to the $F = 2 \rightarrow F' = 3$.

Stage	Cooling red δ(MHz)
MOT	19.5
CMOT	19.5 $\rightarrow$17.6
Molasses	49.0 $\rightarrow$137.0
Optical Pump	243.2[3]

The optical pumping in the experimental sequence is adjacent to the polarization gradient cooling, which typically ends with $\sim$ 100 MHz detuning, and the optical pumping pulse time typically only lasts less than 1 ms to avoid heating from the radiation pressure force, so in order to jump less laser frequency in such a short time we set the optical pumping beam frequency close to the $F = 2 \rightarrow F' = 2$ transition by the -1 order of an 80 MHz AOM which creates an additional -160 MHz difference compared to the MOT beam.

4.3.2.3 Repump laser

The repump laser setup is shown in Fig. 4.8, where 3 fiber output ports are used for beatnote lock, probe on the science side, and repump on the MOT side during laser cooling stages, respectively. The MOT repump port is coupled to the fiber splitter, so the fiber output on the MOT side has both cooling and repump light.[4]

The repump is locked close to the ^{87}Rb $F = 1 \rightarrow F' = 2$ transition through the beatnote lock. Although we are able to dynamically tune the repump frequency during the laser cooling stages, typically we do not change that and it is not very sensitive.

[3] The optical pumping is 23.4 MHz blue detuned to the $F = 2 \rightarrow F' = 2$.
[4] The splitter only couples repump into 2 arms on the MOT side.

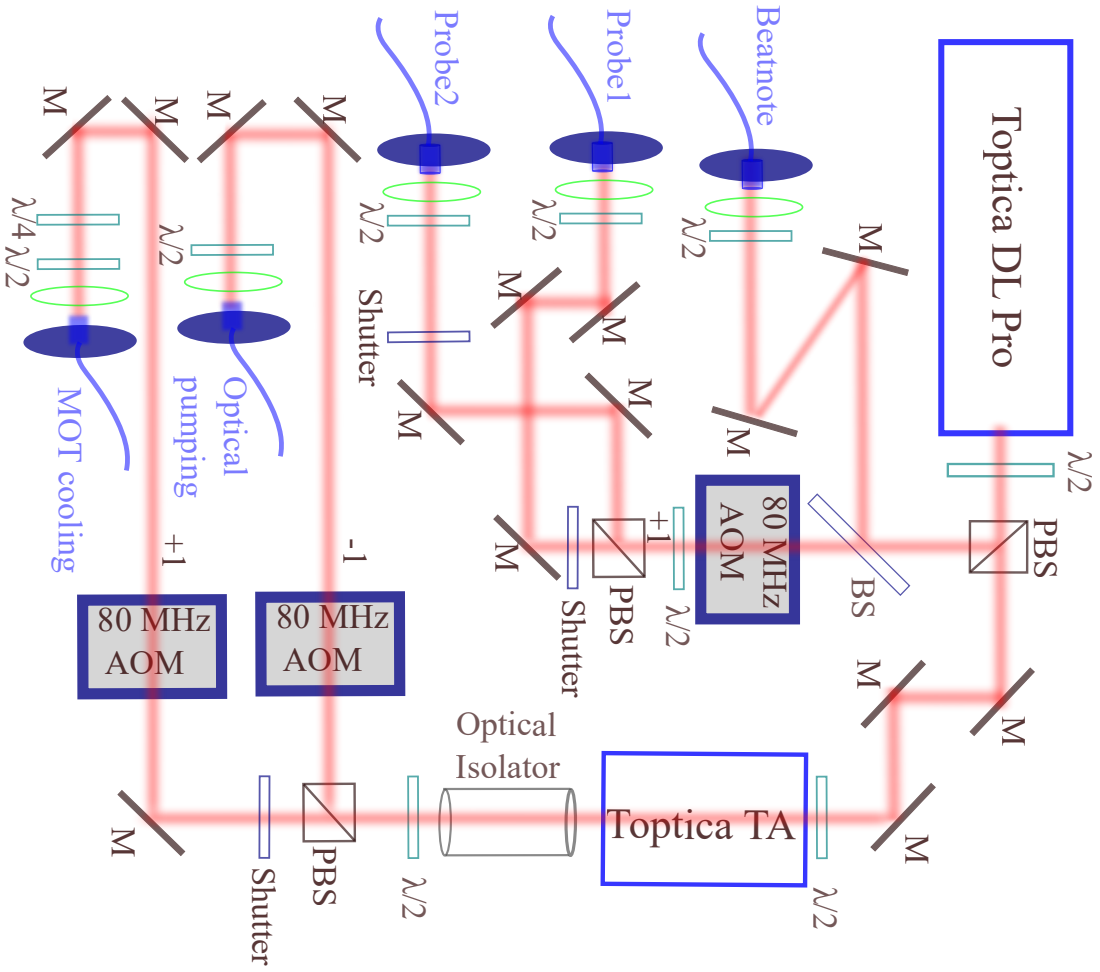

Figure 4.7: Cooling laser configuration.

4.3.3 Laser locking

In our lab, the master laser is locked to the Saturated Absorption (SatAbs) spectrum, ensuring a high degree of precision for the frequency standard. Both the cooling and repump lasers are then synchronized with the master laser through a beatnote method. The specifics of this synchronization process and the underlying principles of the laser locking mechanisms will be comprehensively discussed in the subsequent section.

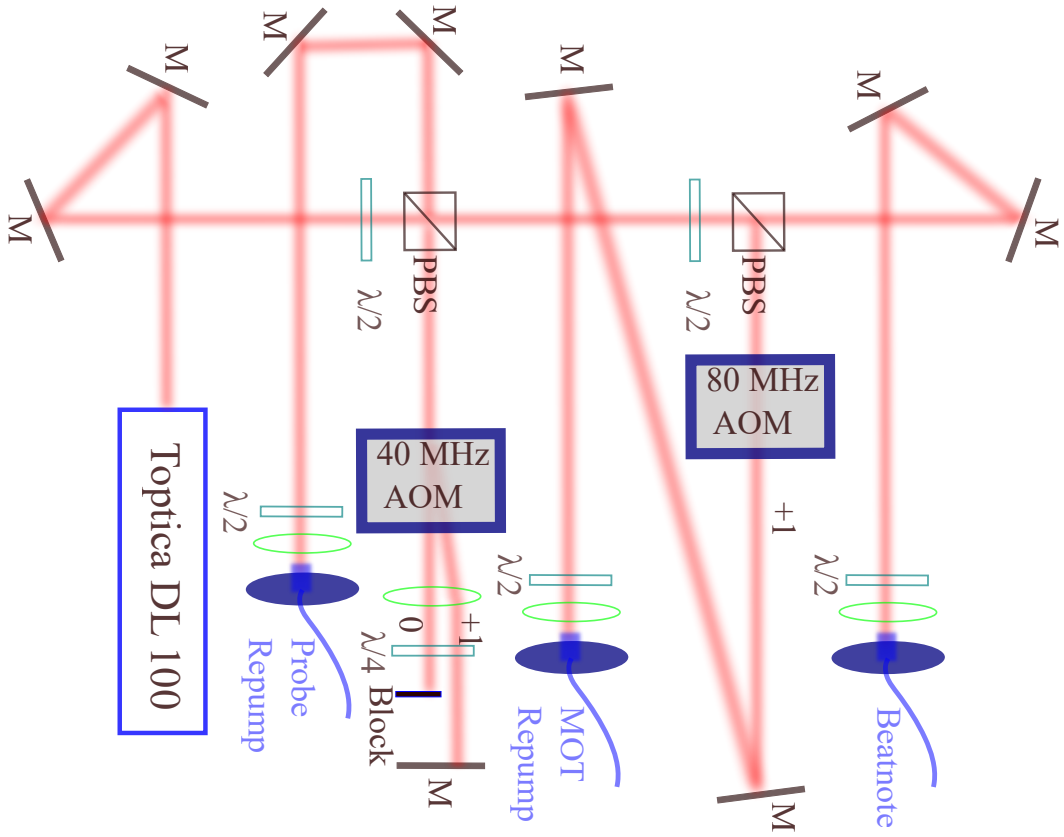

Figure 4.8: Repump laser configuration.

4.3.3.1 Master laser lock

The SatAbs photodiode collects the absorption spectrum and the error signal for locking is generated from a lock-in amplifier by frequency modulation (FM) of the AOM, shown in Fig. 4.9.

With FM, the SatAbs spectrum $S(f)$ is also modulated. Suppose that the laser frequency is swept with rate $df/dt = v_{\text{sweep}}$, then the photodiode reading is $S\left(f(t)\right) = S(f_0 + v_{\text{sweep}}t - f_{\text{AOM}}(t))$, where $f_{\text{AOM}}(t) = f_{\text{AOM},0} + A\cos(2\pi f_{\text{FM}}t)$. If we send the photodiode reading to the lock-in amplifier with reference signal $V_{\text{ref}} = \cos(2\pi f_{\text{FM}}t + \phi)$, then after the mixer the signal

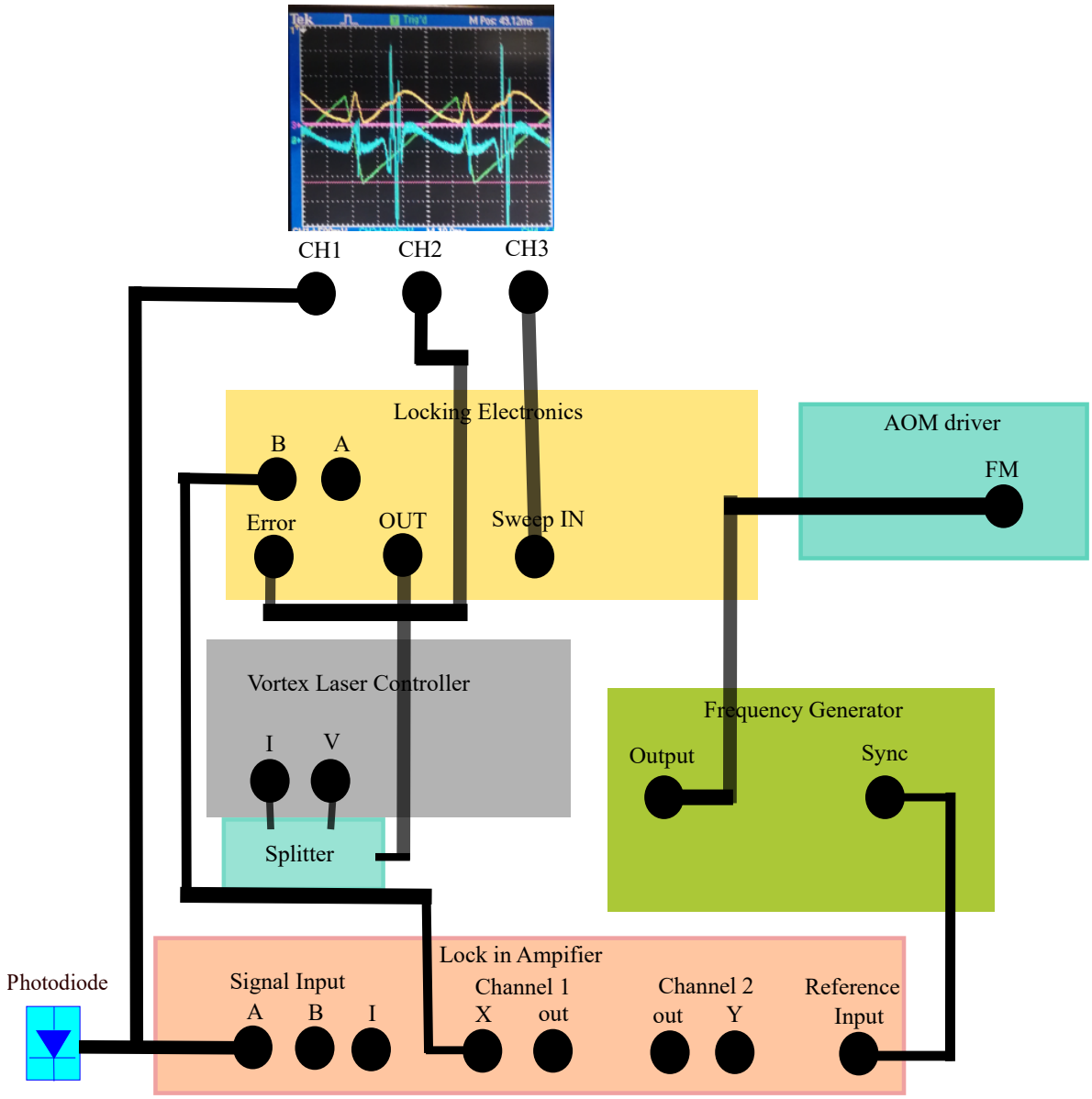

Figure 4.9: Master laser locking diagram

becomes

$$
\begin{aligned}
S\left(f(t)\right) V_{\text{ref}} =& S(f_0 + v_{\text{sweep}} t)\cos(2\pi f_{\text{FM}} t + \phi) \\
& - \frac{dS}{df}|_{f=f_0+v_{\text{sweep}}t} \left[f_{\text{AOM},0}\cos(2\pi f_{\text{FM}} t + \phi) + \frac{A}{2}\left(\cos(4\pi f_{\text{FM}} t) + \cos\phi\right)\right],
\end{aligned}
\tag{4.2}
$$

where $A \ll f_{\text{AOM},0}$ and $v_{\text{sweep}} f_{\text{FM}} \ll 1$. After the low pass filter, the signal becomes

$$[S\left(f(t)\right) V_{\text{ref}}]_{\text{DC}} = -\frac{A}{2} \cos\phi \frac{dS}{df}|_{f=f_0+v_{\text{sweep}}t}, \tag{4.3}$$

which is proportional to the derivative of the spectrum, thereby an error signal for locking is created for locking electronics.

4.3.3.2 Beatnote lock

The beatnote is generated from a fiber combiner which has three tones from the master, cooling, and repump laser. The fiber is then sent to a $10\,\text{GHz}$ fast photodiode (EOT GaAs ET-4000AF), shown in Fig. 4.10. The three beatnote frequencies within $10\,\text{GHz}$ are $1046\,\text{MHz}$, $5522\,\text{MHz}$, and $6568\,\text{MHz}$, in which we only need the first two to lock cooling and repump. A splitter (ZX10-R-14-S) split the beatnote into two. Low-pass filters (VLF-2850+) are applied to keep only the cooling-master beatnote, and high-pass filters (VHF-4400+) keep the other two high-frequency beatnotes. Note that to eliminate the cooling-repump beatnote, we also applied a low-pass filter (VLF-4400 +) in series with the high-pass filter. The beatnote and the Novatech DDS signal are sent to the PLL to receive an error signal to lock. Initially, we used the Precision Photonics LB1005 PI controller as the locking electronics. Later on we upgraded it to Toptica Digilock, which makes locking easier.

4.4 Magnetic field Control

The magnetic field is generated by running currents in coils in this lab, so coils and current controllers (servos) are needed.

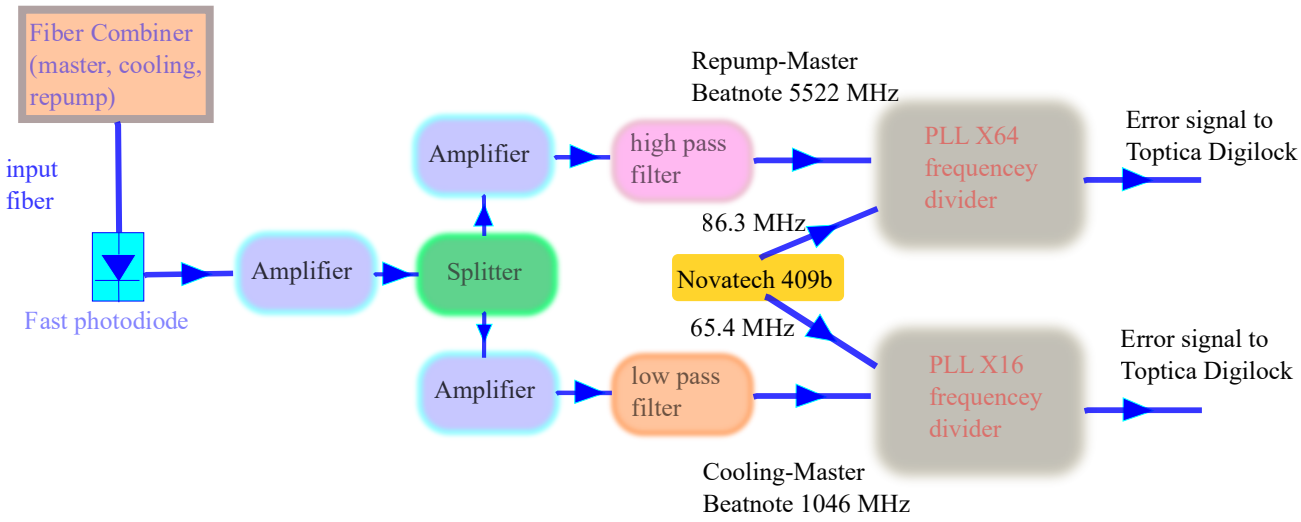

Figure 4.10: Beatnote lock diagram.

The magnetic field in this lab needs to be controlled under three cases: (i) laser cooling and magnetic trapping in the MOT cell. (ii) Magnetic transport of the trapped atoms from the MOT cell to the science cell. (iii) Magnetic trap and magnetic field control in the science cell for physics study.

In this section, we will introduce the coils used in the lab and the coil winding procedure. Then we introduce the servos, and finally the application of magnetic transport as well as bias and gradient control in the science cell.

4.4.1 Coils in RbRb

The coils used in the lab are shown in Fig. 4.11. (i) Out of the MOT cell we have 8 cloverleaf coils and 2 round coils for bias field control along 3 directions. (ii) We have 11 pairs of coils for magnetic transport, for clarity only half of the coils are shown in Fig. 4.11. The two round shape coils also create the quadrupole magnetic field for magnetic trapping in the MOT and science cell. (iii) Eight clover leaf and eight racetrack-shaped coils are out of the science cell

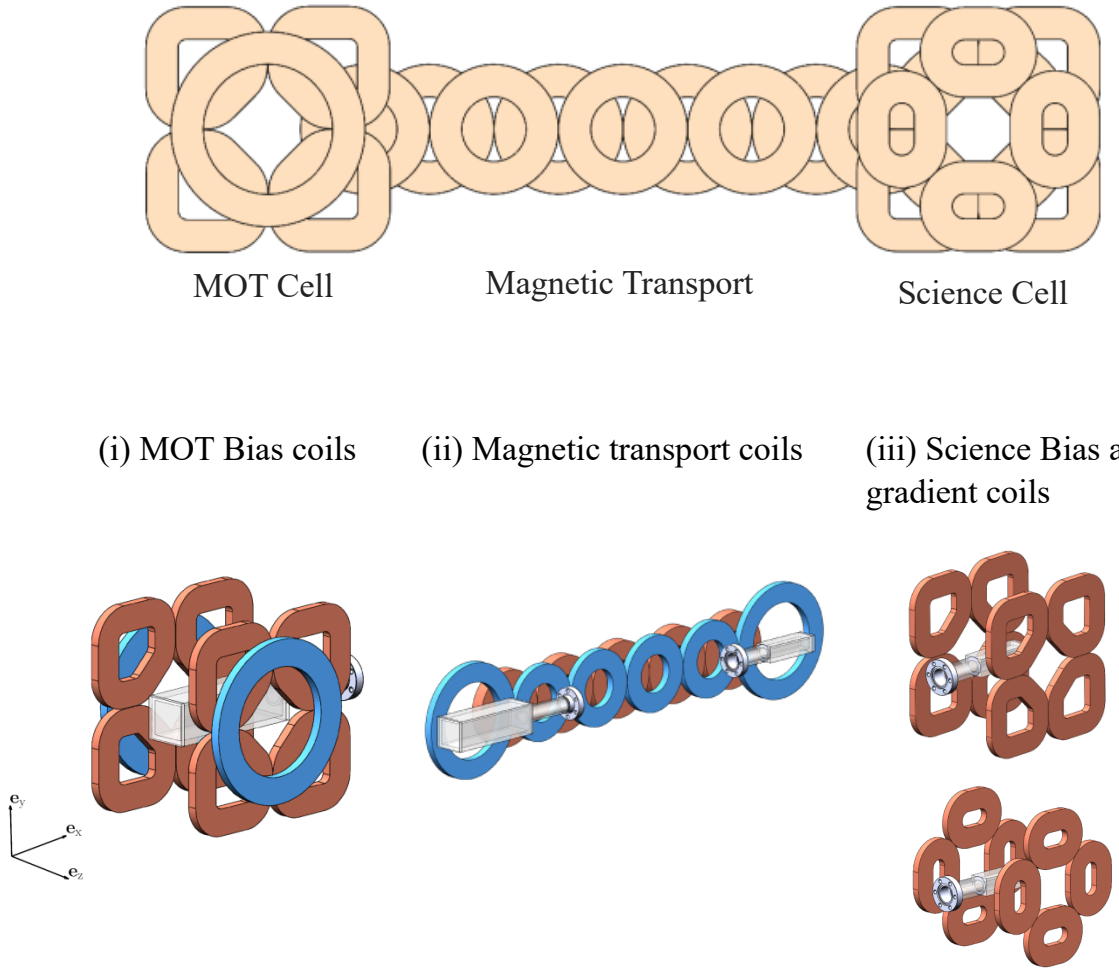

Figure 4.11: Coils in RbRb. Reproduced from [1].

for the bias and gradient field control.

4.4.2 Coil winding

The coil winding platform is shown in Fig. 4.12(a), where rods are to create tension during the winding of the ribbon wire. After 63[5] turns of winding for each coil, we tied the coil to the coil winding form, then put epoxy on top of the coil for shape fixing. To ensure that the epoxy

[5]The target number is 60, but we typically wind 3 more turns, since the epoxy during curation will be attached the outtermost turn, and we have to remove that turn.

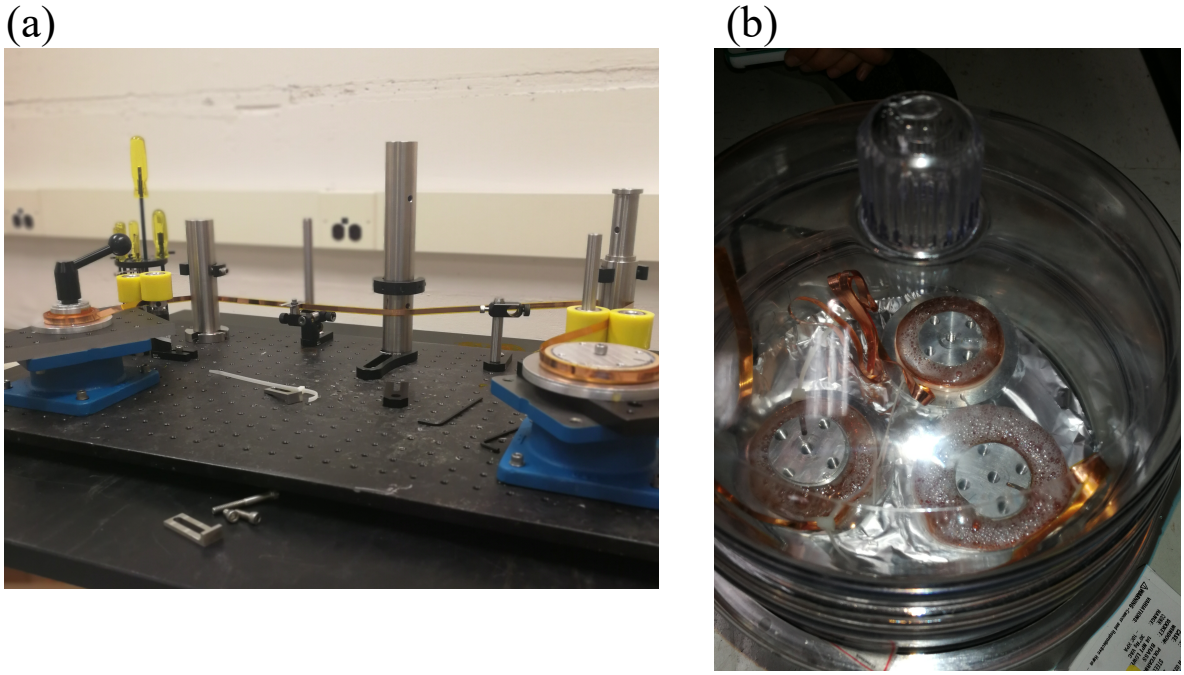

Figure 4.12: Coils winding. (a) shows the coil winding pipeline. (b) shows the coils with epoxy in a vacuum bubble.

was fully immersed in the coil, we placed the coils in a vacuum bubble for 30 minutes, as shown in Fig. 4.12(b). Then we let the epoxy cure, which typically takes more than 10 hours at room temperature. To accelerate the curation, the epoxy can be heated.

However, the epoxy does not have good thermal conductance, and the current running in the coil can be up to 100 A, thereby we need to remove the epoxy as much as possible for better heat dissipation. The epoxy on both sides of the coil is lathed off by team member Ana Valdes in the UMD machine shop.

An example of the lathed coil surface under the microscope is shown in Fig. 4.13(a).

4.4.3 Current servos

All current servos in the lab come from two supply (Angilent 4490A) capable of conducting 440 A with beefy cables connected from the corridor outside to the lab "current" manifold, shown

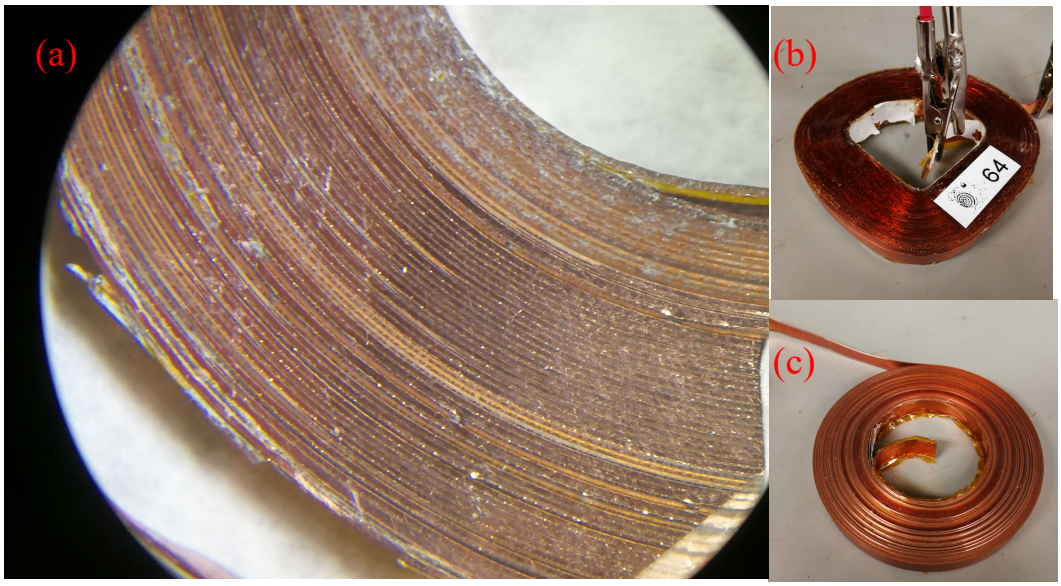

Figure 4.13: (a) Coil surface after lathing under microscope. (b) A cloverleaf coil with epoxy covered. (c) A round shape coil with epoxy removed.

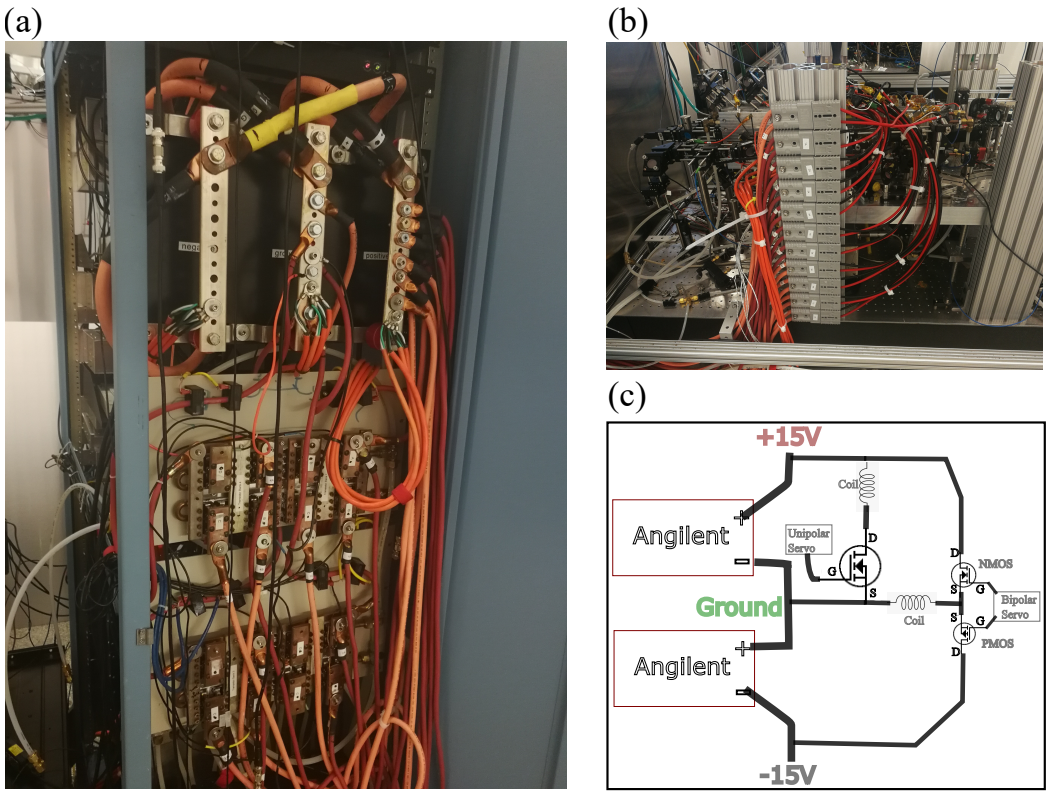

Figure 4.14: (a) The metal bars are the "bus" of the $+15V$, ground and $-15V$ for the current control in the lab. Below is the transistor bank for the transport coil current. (b) Shows the 11 high current cable connectors for the transport coil. (c) Shows the diagram of the unipolar and bipolar current control in the lab.

in Fig. 4.14.

4.4.3.1 Unipolar current servo

The unipolar current servos in the lab control the current of all the magnetic transport coils, including the MOT and science quadrupole coil. It is built on the basis of the design of the NIST lab which uses the Hall sensor for current sensing.

4.4.3.2 Bipolar current servo

The bipolar current servo is designed to control the bias and gradient magnetic field ranging from -20 A to 20 A in the lab. We used to use the commercial product Kepco as the bipolar current source, while the noise in the current mode is quite large and we have an additional servo in its voltage mode for higher bandwidth and less noise. In the current design, we need 12 bipolar servos (3 MOT bias + 9 for the bias and gradient in the science cell), so purchasing 12 Kepcos is not a financially wise choice. Instead, we built the low-noise sensing resistor-based bipolar current servos on our own. The details of the design can be found in [72]. Here, I will briefly state the design.

The circuit has three high-level modules depicted in Fig. 4.15(a): current sensing module, feedback module, and current generation module. In the current sensing module, a sense resistor transduces the load current to a voltage. The feedback module uses an opamp-based proportional-integral (PI) servo to maintain the sensed voltage at a target value. Lastly, the output of the feedback module is used to govern the MOSFET gate voltage, thereby determining the current through the load.

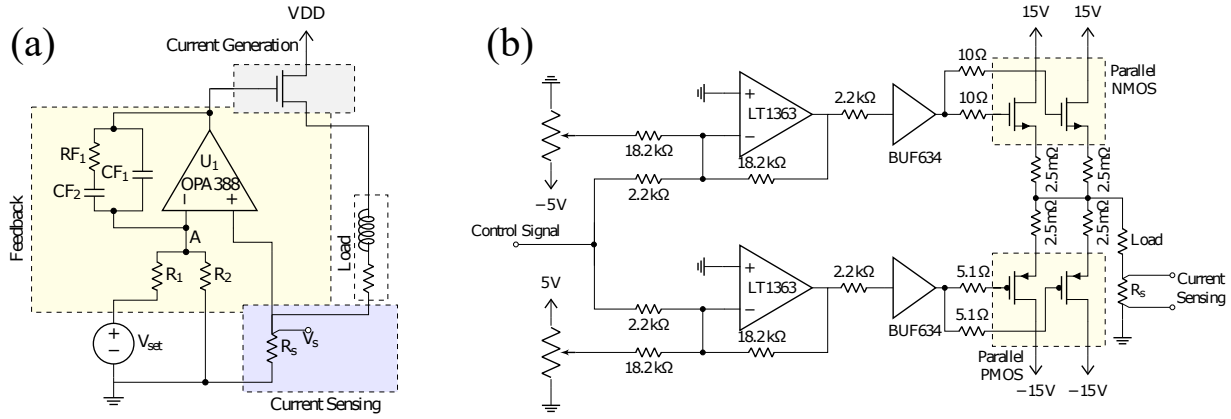

Figure 4.15: Bipolar servo schematics. (a) High-level modules including current sensing, feedback and current generation. (b) Bipolar current control schematics. The control signal is input on the left and divided into positive and negative channels (top and bottom respectively) that control separate banks of NMOS and PMOS transistors before being delivered to the load (far right) and sensed.

The current generation module uses N–channel MOSFETs (NMOS, IXFN520N075T2) for positive current and P–channel MOSFETs (PMOS, IXTN170P10P) for negative current, as shown in Fig. 4.15(b). To avoid crossover distortion when the feedback signal passes below the threshold voltage of the MOSFETs, we used a class AB amplifier design [73, 74]. MOSFETs have a threshold gate voltage V_{th} below which they do not conduct; the AB amplifier design adds a positive offset voltage to the NMOS gate and a negative offset voltage to the PMOS gate. In our circuit, this is implemented with a pair of noninverting summing amplifiers (based on LT1363 opamps) that use trim pots to tune these offset voltages close to the threshold voltage of the MOSFET. The threshold voltages of NMOS and PMOS have opposite polarity, so only one group of MOSFETs will turn on for a specific control signal. For example, when the control signal is positive, the gate voltage of the NMOS and PMOS will be greater than their thresholds, allowing the NMOS to conduct while disabling the PMOS.

4.4.4 Magnetic transport

As we have previously stated, the science cell has a lower background pressure leading to a longer lifetime that is ideal for BEC experiments. Also, the science cell gives more optical axes since the MOT setup is on the other end. Therefore, the apparatus would benefit from the transport of the atoms from the MOT cell to the science cell. We selected magnetic transport because of its high stability. We heard a very pleasant experience from the RbChip lab that once the magnetic transport is optimized, you don't need to optimize it for years. And based on my experience, this is a definitely true statement. The only issue is that it is quite complicated and requires the fabrication of many coils. So in this section, we will first introduce the principle of magnetic transport and then discuss its realization in the lab.

4.4.4.1 Physical principle of the magnetic transport

Magnetic transport in atomic physics is facilitated by an array of overlapping coils configured as an anti-Helmholtz arrangement [75]. Ideally, the aspect ratio of the gradient field $\beta = -B_{zz}/B_{yy}$ should be constant during transport, where B_{ij} is the shorthand notation for dB_i/dx_j. Here z is the direction of strong confinement and y is the direction of transport, and the minus sign in the definition of β is due to the divergent-free B field satisfying $B_{zz} = -(B_{xx} + B_{yy})$.

On the other hand, the atoms are trapped at the place with the minimum magnitude of the B field. In our case, the minimum is zero.

So during transport at time t, the atom is transported to position $\widetilde{y} = y(t)$, then the B field should satisfy two conditions: (i) $|B(y)| = 0$; (ii) $\beta_0 = -B_{zz}(y)/B_{yy}(y)$.

To achieve that, we have to turn on 3 coils simultaneously. Let us take a step back and

suppose we want to achieve that with 2 coils, then condition (i) fixes the current ratio of two coils, and we don't have more free-tuning parameters to fulfill condition (ii). Conversely, with three coils on, we have two independent current ratios to fulfill both conditions.

The 3-coil configuration gives a good scheme for transport except for the boundary conditions. Before and after transport, the atoms are confined in a magnetic quadrupole trap with $\beta = 2$. Consequently, to achieve a different β value during transport, we use a 2-coil configuration at the start to ramp the β value from 2 to β_0, and keep it constant during transport and use another 2-coil configuration at the end to ramp β from β_0 to 2.

With a predefined $y(t)$, we can determine the magnetic field $B(t)$ and the currents $I(t)$ that run in each coil.

4.4.4.2 Realization of magnetic transport

As previously stated, 11 coil pairs are used for transport, so we have 9 free-tuning magnetic gradients to control for the 3-coil configuration, i.e., [(1,2,3), (2,3,4), (3,4,5),...,(9,10,11)]. Then for the 2-coil stages, we have more parameters to decide, from where to transit from 2-coil to 3-coil and the β_0 value to the detail of the β ramp. Finally, $y(t)$ is also optimized. We send all these parameters to a machine learning platform (M-Loop [76]) for optimization, and the transport efficiency is up to 80%, which is validated by a round-trip transport.

An example of a round trip transport curve is shown in Fig. 4.16.

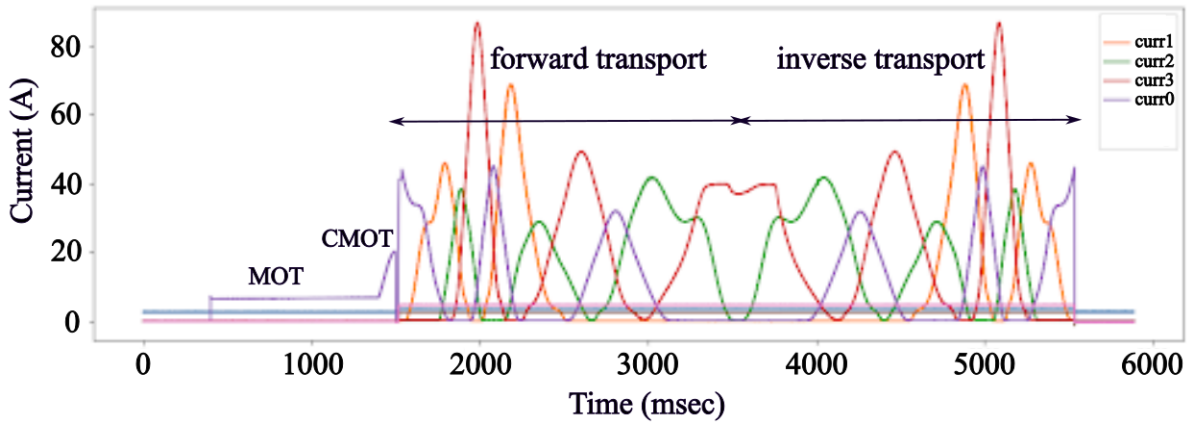

Figure 4.16: Time traces of current control during a round-trip magnetic transport.

4.4.5 Bias and gradient field control

In both the MOT cell and the science cell, bias magnetic field control is essential. And for the science cell, we aim to achieve additional full magnetic gradient control, i.e., we want to control all the 9 components of the tensor $\nabla \mathbf{B}$. From the Maxwell equation we have $\nabla \cdot \mathbf{B} = 0$ and $\nabla \times \mathbf{B} = \mathbf{0}$. So in total, we need at least 5 independent gradient controls for the 5 degrees of freedom. In our design, we used 16 coils with 9 independent bipolar current controls to achieve full control of bias and gradient magnetic field control.

I will elaborate the design in the subsequent sections.

4.4.5.1 Bias configuration

As shown in Fig. 4.17, we use eight independently controlled cloverleaf coils to control the bias field. The designed B field versus current I is $B_x/I_x = 1.553$ G/A, $B_y/I_y = 3.198$ G/A and $B_z/I_z = 3.198$ G/A.

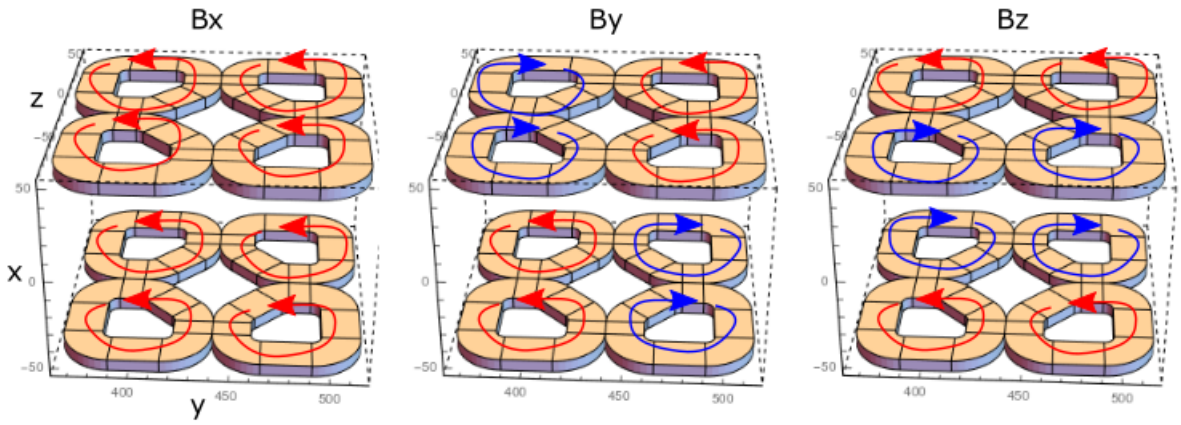

Figure 4.17: Bias coil and current configuration.

4.4.5.2 Gradient configuration

As shown in Fig. 4.18, we use eight independently controlled cloverleaf coils to control the gradient field components except for the $dB_y/dy = -dB_z/dz$ pair controlled by eight racetrack coils. As a shorthand notation we use $B_{ij} = dB_i/dx_j$. The designed gradient field versus current I is (i) $B_{yz}/I = B_{zy}/I = 0.923$ G/cm/A, (ii) $B_{xy}/I = B_{yx}/I = 0.937$ G/cm/A, (iii) $B_{xz}/I = B_{zx}/I = 0.937$ G/cm/A, (iv) $B_{xx}/I = -2B_{yy}/I = -2B_{zz}/I = 0.366$ G/cm/A and (v) $B_{yy}/I = -B_{zz}/I = 0.492$ G/cm/A.

4.4.5.3 Calibration of the B field

Number of turns calibration The number of turns of each coil during fabrication might have some uncertainty, so it is necessary to calibrate it, and we select to test it with the BEC. The procedure is as follows. (i) We prepared the BEC in a magnetic sensitive state, for example, $|F = 2, m_F = 2\rangle$. (ii) We applied a magnetic gradient force $-\boldsymbol{\mu} \cdot \boldsymbol{\nabla}|\mathbf{B}|$ during the free expansion of BEC by running currents to only one of the eight clover leaf coils, for example 10 A with a

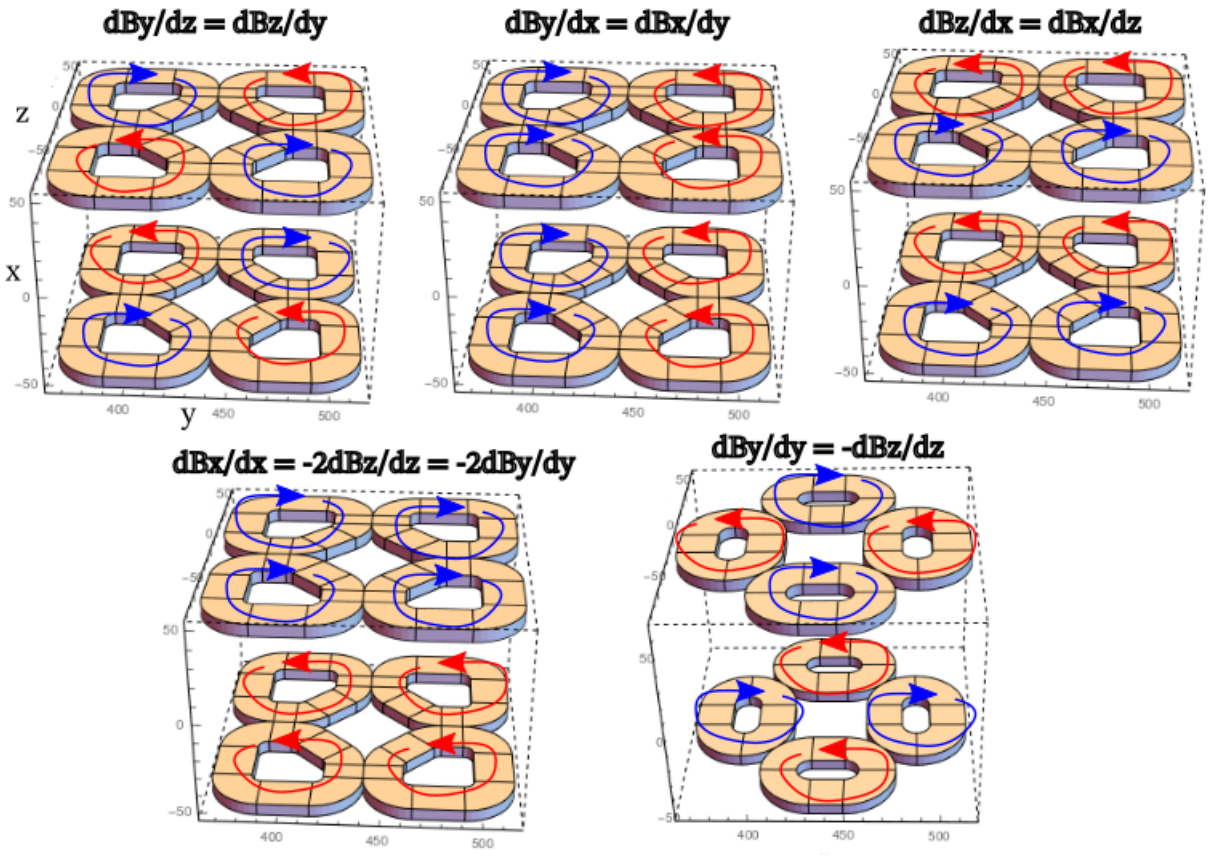

Figure 4.18: Gradient coil and current configuration.

TOF$=15$ ms. From the camera, we can know the displacement of the cloud as a result of the magnetic gradient. The displacement ratio gives the number of turns ratio.

B field versus Current Calibration The B field can be calibrated by microwave or RF resonance. In our case, we used the microwave and the two states are $|F=2,m_F=2\rangle$ and $|F=1,m_F=1\rangle$ with a magnetic sensitive Zeeman shift 2.1 MHz/G. We basically scan the resonance by ARP under different detuning and magnetic fields by scanning currents applied in coils. An example of B_y versus I is shown in Fig. 4.19. Note that the minimum detuning is nonzero which means the existance of non-zero background magnetic field. The zero-field current can be obtained at the minimum of the resonance. In this way we obtain the zero-field current in the lab is

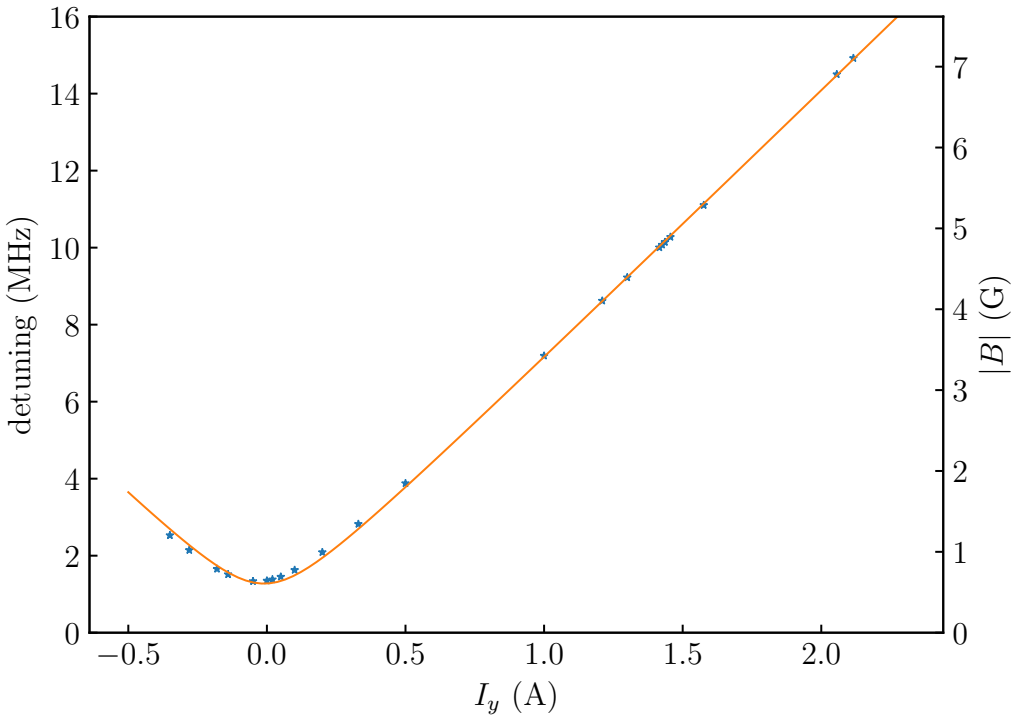

Figure 4.19: Calibration of B field using microwave resonance. Blue points are measured from ARP resonance, and the orange is fitted from the square root of a parabola.

$(I_x, I_y, I_z) = (-53\ \mathrm{mA}, -45\ \mathrm{mA}, -224\ \mathrm{mA})$. And the B field and current ratio can be extracted from the slope in the large field region, i.e., $B_x/I_x = 1.38\ \mathrm{G/A}$, $B_y/I_y = 3.33\ \mathrm{G/A}$ and $B_z/I_z = 3.30\ \mathrm{G/A}$. These values are close to the design.

4.5 Digital micromirror device control

A Digital Micromirror Device (DMD) is a type of microelectromechanical system (MEMS) that is pivotal in the field of digital light processing (DLP) technology [77]. At the core of a DMD is an array of microscopic mirrors, each individually controlled to tilt at precise angles. These mirrors, typically fabricated on a silicon wafer, are capable of tilting in two directions, allowing them to reflect incoming light either into or away from the optical path of the device.

In a typical application, light from a source is directed onto the DMD chip. Each mirror's orientation determines whether the light is reflected towards the projection lens ('on' state) or away from it ('off' state). This binary operation of the mirrors, combined with the diffraction effects, enables the creation of high-resolution images or patterns. Due to their high speed and precision, DMDs are capable of modulating light both spatial and temporal.

In our lab, we have two DMDs, one is for creating a spatial and temporal dependent optical dipole potential using scalar light shift and the other uses to create patterns from the vector light shift.

Typical applications of the scalar light shift DMD include (i) creating confining trap, such as the box trap, or creating a harmonic trap using halftoning [78]. (ii) creating collective mode excitations such as the scissors mode by displacing the harmonic trap by an angle. (iii) creating dynamical "movie" such as Bragg scattering by a moving sinusodial potential [79].

Typical applications of the vector light shift include (i) creating spatial dependent vector light shift, (ii) creating tracer particles for velocimetry which will be introduced in the chap. 5.

DMD chip is not designed for a laser source since it creates many laser speckles which act as an uncontrollable disorder optical potential for the atoms. LED is not a good option here, since it diverges so fast during propogation. Superluminescent LED (SLED) is an option [80], but its power is quite low. In our lab, for the scalar light shift light source we selected a multimode $635\ \mathrm{nm}$ laser with $\sim 3\ \mathrm{nm}$ linewidth which reduces the coherence length and thereby reduces the speckles effect. For the vector light shift DMD, we use the single mode $790\ \mathrm{nm}$ laser source.

Chapter 5: Velocimetry

In Chap. 3 we introduced several well-developed velocimetry techniques in the classical fluid and some proposed techniques in quantum fluid, among which the particle image velocimetry (PIV) is the one implemented in our system. In this chapter I will introduce the detail of the implementation and benchmark test on several velocity field in atomic BEC.

5.1 PIV in BEC

I want to begin with a question: what is the most important part in the PIV? My answer is tracer particles, which show the same trajectory as the fluid particles so that we can read the velocity field of the fluid. Ideally, we expect the tracer particles to have the same mechanical property of the fluid particles, at the mean time we can also distinguish the tracers from the fluid. A different spinor species seems to be the best candidate because the scattering length differences between the inter- and intra-species are approximately the same. For example, in the ^{87}Rb, we can prepare the BEC in $|F = 1, m_F = 1\rangle$ and use $|F = 1, m_F = 0\rangle$ as tracer particles. With an additional magnetic bias field we can selectively transfer $|F = 1, m_F = 0\rangle$ to the $F = 2$ manifold for imaging.

The main technical challenge is then how to introduce the tracer particles into the system in a spatial-dependent manner so that we can extract the local velocity field. A non-spatial

dependent transfer of fluid particles to tracer particles can be implemented typically by a RF or microwave pulse which can be hardly controlled in a spatial dependent manner due to its large wavelength (RF:~ 100 m; microwave:~ 100 mm) relevant to the typical size of an atomic BEC (~ 10 μm). Consequently we have to use EM field with wavelength at least a magnitude smaller than the size of atomic BEC, and that is the laser with wavelength ≤ 1 μm. In Chap. 2 we have introduced using AC vector light shift as RF field, i.e., if the incident light has two tones

$$\mathbf{E} = \boldsymbol{\epsilon} \left[e^{-i(\omega+\Delta\omega)t} + e^{-i(\omega-\Delta\omega)t} \right], \tag{5.1}$$

then the effective B field is proportional to

$$\mathbf{B}_{eff} \propto i(\mathbf{E} \times \mathbf{E}^*) = 2i(\boldsymbol{\epsilon} \times \boldsymbol{\epsilon}^*)[1 + \cos(2\Delta\omega t)]. \tag{5.2}$$

Therefore, apart from the DC effective magnetic field, we obtain an AC effective magnetic field with angular frequency $2\Delta\omega$ which is the frequency difference of the two tones.

If an external DC magnetic bias field sets a Zeeman shift with angular frequency $2\Delta\omega$ that is resonant to the AC part of the B_{eff}, the magnetic dipole transition will drive the atoms to other spinor states within the ground state manifold, thereby we can achieve the RF coupling in an optical manner under the condition that $2\Delta\Omega$ is in the RF range. Finally, the spatial dependence of the coupling can be achieved by a spatial light modulator, in this way we can control the position of the tracer particles. We can also understand the magnetic dipole transition by two-tone laser as a three level Raman transition, and thereby we will call the PIV technique Raman PIV.

I have briefly stated the Raman PIV in BEC, in the following subsection I will introduce the details of its implementation in our system.

5.1.1 Details of the Raman PIV technique

Our Raman PIV technique, schematically illustrated in Fig. 5.1(a)-(c), allows us to directly measure the velocity field and thereby both velocity structure function and velocity increments statistics for turbulence study in Chap. 6. In this technique we begin with some initial velocity distribution [representative depiction in Fig. 5.1(a)], then create localized "tracer particles" consisting of atoms in a different hyperfine state using a spatially resolved Raman technique [Fig. 5.1(b)], and, after a Δt delay, measure the displacement of the tracers [Fig. 5.1(c)]. This then directly leads to the local fluid velocity.

We used ^{87}Rb BECs with $N \approx 2 \times 10^5$ atoms in the $|F = 1, m_F = 1\rangle$ hyperfine ground state with strong vertical confinement (trap frequency $\omega_z = 2\pi \times 220$ Hz) provided by a 1064 nm trapping laser with an elliptical cross section, traveling along e_x. Additionally, a digital micromirror device (DMD) patterned 638 nm multimode laser traveling along $-\mathrm{e}_z$ provided in-plane confinement. An ≈ 1.4 G magnetic bias along e_y created a $\Delta f = 1$ MHz Zeeman splitting between adjacent m_F states.

Figure 5.1(d) schematically shows the geometry used to create localized tracer particles: a pair of copropagating 790 nm lasers with frequency difference Δf drove m_F-changing Raman transitions with a 50 kHz Rabi frequency.

The two-tone Raman beam, with a wavelength of 790 nm, was generated by applying amplitude modulation to the 80 MHz frequency signal driving the acousto-optical modulator

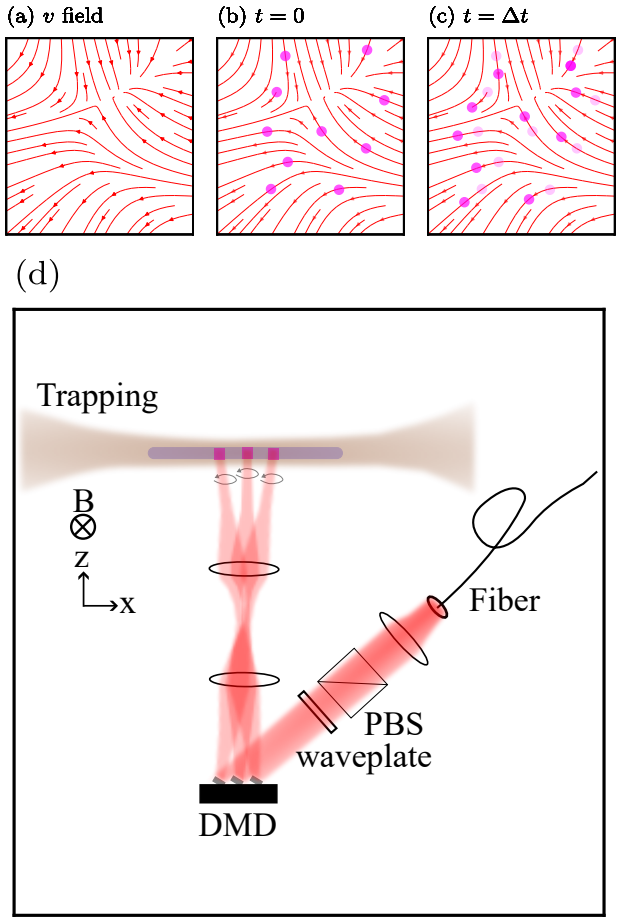

Figure 5.1: Concept. (a) An example of velocity field. (b) Tracer particles (bright pink) are injected into the system at $t = 0$. (c) At $t = \Delta t$, tracer particles (bright pink) move from their initial position (dark pink). (d) Spatially-resolved Raman technique to create localized tracer particles.

(AOM). This modulation was set at a frequency difference of $\Delta f/2 = 0.5$ MHz, effectively manipulating the AOM's first-order output to create the desired two-tone beam.

We selected 0.5 MHz modulation to ensure that we can couple the two-tone with enough power(≈ 100 mW) of light simultaneously into a single optical fiber so that the two-tone can co-propogate to the BEC. The PBS and waveplates is to ensure the outcoming light from the DMD has as much circular polarized component as possible. Ideally, we expect a purely circular polarized beam since it will create the effective magnetic field along the beam propagation

direction $\hat{e}_z$, which can be seen by plugging the circular polarized vector into the effective B field expression, i.e. $i(\hat{e}_x + i\hat{e}_y) \times (\hat{e}_x - i\hat{e}_y) = 2\hat{e}_z$. For some reason, the beam polarization is difficult to control after reflecting from the DMD, and we rotated the waveplate to optimize for a maximum Rabi frequency of 50 kHz at the atom.

The bichromatic 790 nm Raman beam was patterned by the DMD, enabling the placement of arbitrary patterns of tracer atoms in $|F = 1, m_F = 0\rangle$. Tracer atoms were selectively measured using partial transfer absorption imaging (PTAI) [81], in which ≈ 6.8 GHz microwaves transferred the tracers to $|F = 2, m_F = 0\rangle$ where they were detected using resonant absorption imaging. Our imaging system had a nominal 1 μm resolution, and allowing us create and then detect tracers with $1/e$ radius down to 1.6 μm.

In our experimental sequence we first initialized the velocity field of interest and then created a set of N tracers, at positions $\mathbf{r}_0^j$ in the $\hat{e}_x$-$\hat{e}_y$ plane using an $\approx \pi/2$ Raman pulse, with $j = 1 \ldots N$ (these positions were directly verified by PTAI measurement). After a Δt evolution time, we imaged the tracers to obtain the final positions $\mathbf{r}^j$. The velocity at each $\mathbf{r}_0^j$ was taken as the first order finite-difference $\mathbf{v}^j = (\mathbf{r}^j - \mathbf{r}_0^j)/\Delta t$.

5.2 Velocity field measurement of benchmark flow in BEC

The benchmark test progresses from simple to complex scenarios, beginning with the dipole and scissors modes in a harmonic trap and advancing to the irrotational quadrupole flow pattern in a rotating harmonic trap.

5.2.1 Dipole mode

The most simple velocity field is the dipole mode in a harmonic trap [38], in which the motion is analogous to a harmonic oscillator, and the spatial dependence of the velocity field is negligible. So, the dipole mode is ideal for the sanity check of the PIV technique.

I will first derive the dipole mode velocity field and give the experimental verification.

5.2.1.1 Dipole mode velocity field derivation

Starting from the GPE [Eq. (2.57)], and we use the hydrodynamics picture by writing the condensate wavefunction as $\psi = \sqrt{\rho}e^{i\varphi}$, where ρ is the atom number density and φ is the phase of the wavefunction. The velocity field is determined by the phase gradient, i.e., $\mathbf{v} = \frac{\hbar}{m}\boldsymbol{\nabla}\varphi$. The GPE becomes

$$\begin{aligned} \partial_t \rho + \frac{\hbar}{m}\partial_i\left(\rho\partial_i\varphi\right) = 0, \\ -\hbar\partial_t\varphi = \frac{\hbar^2}{2m}\partial_i\varphi\partial_i\varphi + g\rho + V - \mu. \end{aligned} \tag{5.3}$$

Since we only measured the velocity field in 2D, here we focused on the dipole mode in the XY plane with the external harmonic trap potential $V = \frac{1}{2}m(\omega_x^2x^2 + \omega_y^2y^2)$. The excitation of the system can be found by adding a perturbation into the system, i.e., $\widetilde{\rho} \to \rho + \delta\rho$ and $\widetilde{\varphi} = \varphi + \delta\varphi$, which should also satisfy the Eq. (5.3), thereby we can obtain

$$\begin{aligned} \partial_t\delta\rho + \frac{\hbar}{m}\partial_i(\delta\rho\partial_i\varphi + \rho\partial_i\delta\varphi) = 0, \\ -\hbar\partial_t\delta\varphi = \frac{\hbar^2}{m}\partial_i\delta\varphi\partial_i\varphi + g\delta\rho. \end{aligned} \tag{5.4}$$

Since the ground state of the BEC has zero velocity field, we can set $\varphi = 0$, and the density can be treated with Thomas-Fermi approximation, i.e., $\rho = (\mu - V)/g$. The equation of motion for

the perturbation further reduces to

$$\begin{aligned} &\partial_t \delta\rho + \frac{\hbar}{m}(\partial_i \rho \partial_i \delta\varphi + \rho \partial_i^2 \delta\varphi) = 0, \\ &\hbar \partial_t \delta\varphi + g\delta\rho = 0. \end{aligned} \tag{5.5}$$

Now we consider the excitation with angular frequency ω, i.e., $\delta\rho = \delta\bar{\rho}e^{-i\omega t}$, $\delta\varphi = \delta\bar{\varphi}e^{-i\omega t}$. For the dipole mode, the trial solution for oscillation along $\hat{e}_x$ and $\hat{e}_y$ are $\delta\varphi = \delta\bar{\varphi}_x x e^{-i\omega t}$ and $\delta\varphi = \delta\bar{\varphi}_y y e^{-i\omega t}$, which gives the eigenmode $\omega = \omega_x$ and $\omega = \omega_y$ respectively. So the dipole mode frequency along the principle axis is the trap frequency, and the dipole mode velocity field along axis $\hat{e}_j$ is given by $v_j(t) = \frac{\hbar}{m}\delta\bar{\varphi}_j e^{-i\omega_j t}$, where $j = x$ or y. Note that this velocity field is spatial-independent, so we can place a single tracer into the BEC for the velocity field measurement.

5.2.1.2 Dipole mode experimental verification

We first prepared $|F = 1, m_F = 1\rangle$ BEC in the ground state with trap frequency $(\omega_x,\ \omega_y) = 2\pi \times (46,\ 23)\mathrm{Hz}$ created by projection from the confining DMD. [Fig. 5.2(a)]. The dipole mode was excited by a magnetic kick along the weak confinement direction $\hat{e}_y$ [vertical in Fig. 5.2(a-b)]. We then injected the tracer patterns shown in Fig. 5.2(b) using Raman PIV, and measured the tracers' position difference with $\Delta t = 2\,\mathrm{ms}$. One tracer position is plotted in the Fig. 5.2(c) with a dipole mode frequency of $23.6\,\mathrm{Hz}$ and peak velocity $\approx 0.5\ \mathrm{mm/s}$ fitted by a damped sinusoidal function. The measured dipole frequency agrees well with the trap frequency.

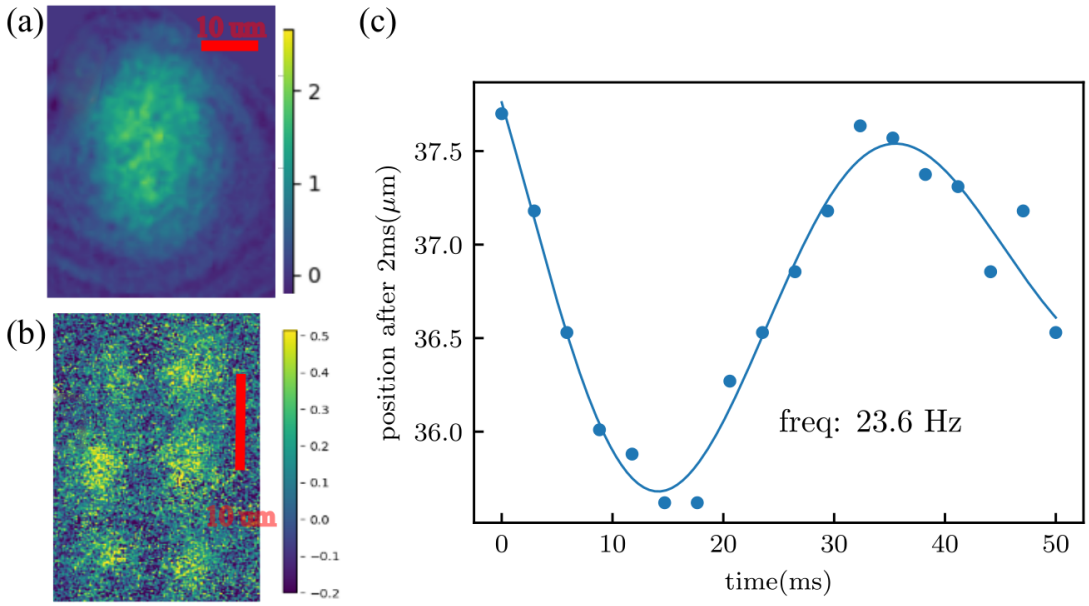

Figure 5.2: Velocity measurement of the dipole mode using PIV. (a) shows the ground state BEC in a harmonic trap. (b) shows the PIV tracer patterns. Colorbars in (a-b) show the optical density (OD). (c) shows the position change of a tracer under dipole mode excitation.

5.2.2 Scissors mode

We then add some complexity by introducing some spatial dependence in the velocity field. The quadrupole mode [82] would be a good candidate in which the scissors mode [83] is the one I am most interested, since it is related to the irrotational flow of the superfluid. So, here I applied the Raman PIV to study the velocity field of the scissors mode. Before that, let me explain more about the scissors mode.

Consider the BEC in a harmonic trap under an angle displacement [Fig. 5.3(a)], similar to the pendulum, the BEC would have an angle oscillation with a frequency dependent on the moment of inertia. The classical moment of inertia is given by $I_c = \int d^3r \rho r^2$, but the measured moment of inertia extracted from the angle oscillation frequency in the superfluid is less than I_c,

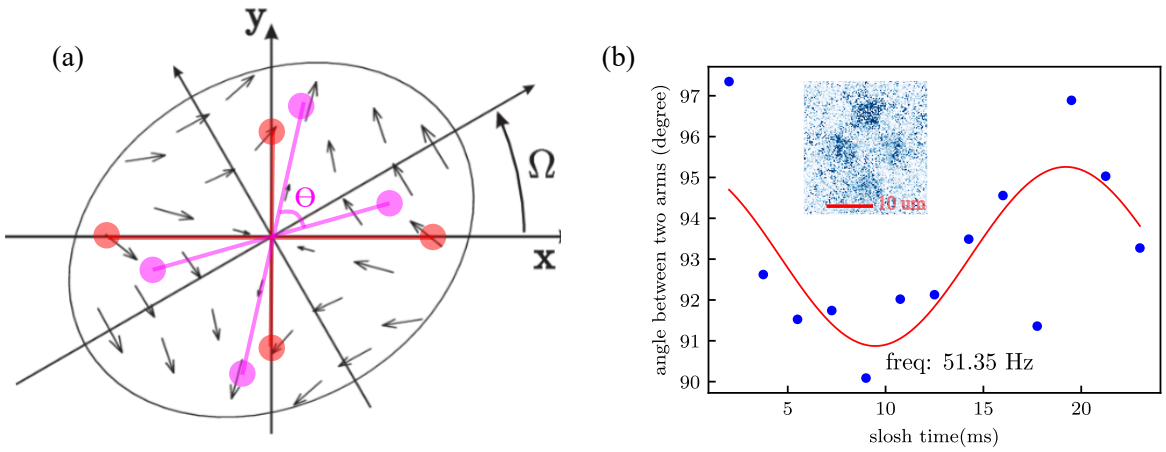

Figure 5.3: Scissors mode measurement using PIV. (a) shows the velocity field of a rotating harmonic trap. In the PIV, the red dots move to the pink dots with the angle between two "arms" θ changing dynamically. (b) shows the scissors mode oscillation of the θ using PIV, and the inlet shows the tracers' pattern used in the experiment.

which can be explained by the irrotational velocity field in the superfluid, and this special mode is called the scissors mode with a velocity field $\mathbf{v} = \nabla(\alpha xy)$, where α is a parameter determined by the trap frequency. Fig. 5.3(a) depicts this irrotational velocity field, and we observe that the overall shape rotating direction agrees with the long arm (weak confinement) movement, while opposite to the short arm (strong confinement) fluid motion. Now suppose we do a PIV measurement to this flow field by injecting 4 tracer particles, which are drawn as red circles in Fig. 5.3(a) with the two-arm angle $\theta = 90°$, then under some time interval they will move to the positions marked by pink dots with $\theta < 90°$. In contrast, if we reverse the direction of Ω, the θ will increase during the PIV, thereby the θ will oscillate back and forth with a frequency equal to the overall shape oscillation frequency. We typically call this mode the "scissors" mode, since it is analogous to scissors' arms opening and closing periodically.

5.2.2.1 Scissors mode derivation

From the equation of motion of the wavefunction perturbation [Eq. (5.5)], we apply the trial solution for the scissors mode, i.e., $\delta\rho = \delta\bar{\rho}e^{-i\omega t}$ and $\delta\varphi = \delta\bar{\varphi}_{xy}\ xye^{-i\omega t}$ and obtain the following.

$$\begin{aligned} &-i\omega\delta\bar{\rho} - \frac{\hbar(\omega_x^2+\omega_y^2)}{g}xy\delta\bar{\varphi}_{xy} = 0, \\ &g\delta\bar{\rho} - i\omega\hbar xy\delta\bar{\varphi}_{xy} = 0. \end{aligned} \tag{5.6}$$

Consequently the eignfrequency ω should satisfy

$$\det\begin{pmatrix} i\omega & \frac{\hbar(\omega_x^2+\omega_y^2)}{g}xy \\ g & -i\omega\hbar xy \end{pmatrix} = 0 \quad \Rightarrow \quad \omega = \sqrt{\omega_x^2+\omega_y^2}. \tag{5.7}$$

The velocity field is given by

$$\mathbf{v}(t) = \frac{\hbar\delta\bar{\varphi}_{xy}}{m}\boldsymbol{\nabla}(xy)e^{-i\omega t} = \frac{\hbar\delta\bar{\varphi}_{xy}}{m}(x\hat{e}_y + y\hat{e}_x)e^{-i\omega t}, \tag{5.8}$$

which is quite different from the classical fluid with rotational velocity field $\mathbf{v} = \boldsymbol{\omega}\times\mathbf{r} = \omega(x\hat{e}_y - y\hat{e}_x)$.

5.2.2.2 Scissors mode velocity field verfication

The experimental result is shown in Fig. 5.3(b), where we loaded the atoms into a harmonic trap with trap frequency $(\omega_x,\ \omega_y) = 2\pi\times(46,\ 23)\mathrm{Hz}$ confined by the optical potential created from the confining DMD. We excited the scissors mode by a sudden displacement of the trap potential by changing the harmonic trap potential from the confining DMD. The tracer pattern is

shown in the inlet, and the angle θ is measured after the $\Delta t = 2\,\text{ms}$. The oscillating frequency agrees well with the theoretical result $\omega_{\text{sissors}} = \sqrt{\omega_x^2 + \omega_y^2} = 2\pi \times 51.4\text{Hz}$.

5.2.3 Rotating Trap

The scissor mode indicates that the irrotational flow exists in the BEC, but we only measured velocity at four different positions. So, can we add more tracers and observe the whole velocity field? For slowly rotating systems, such that no vortices are present, the superfluid velocity is theoretically established to exhibit an irrotational quadrupole-like pattern [84] $\mathbf{v} = a(y\mathbf{e}_x + x\mathbf{e}_y)$ with $a \propto \Omega$ for small Ω. At higher rotation frequencies, when Ω becomes comparable to the trap frequencies $\omega_{x,y}$, this becomes a metastable configuration with a range of possible instability conditions [85, 86] the details of which must be obtained numerically. Here I will first derive the steady-state flow field, then give the experimental verification for an overcritical transient flow field.

5.2.3.1 Steady-state velocity field

In the rotating frame with angular frequency $\mathbf{\Omega}$, the GPE becomes

$$\frac{\partial \rho}{\partial t} + \nabla \cdot (\rho(\mathbf{v} - \mathbf{\Omega} \times \mathbf{r})) = 0, \tag{5.9}$$

$$\frac{\partial \mathbf{v}}{\partial t} + \nabla \left(\frac{v^2}{2} + \frac{V}{m} + \frac{g}{m}\rho - \mathbf{v} \cdot (\mathbf{\Omega} \times \mathbf{r}) \right) = 0, \tag{5.10}$$

where the external potential $V = \frac{m}{2}(\omega_x^2 x^2 + \omega_y^2 y^2)$.

Consider the case $\mathbf{\Omega} = \Omega \hat{e}_z$, and using the irrotational ansatz $\mathbf{v} = \alpha \nabla(xy)$. Then $\mathbf{v} =$

$(\alpha y, \alpha x, 0)$, and $\mathbf{\Omega} \times \mathbf{r} = (-\Omega y, \Omega x, 0)$. Eq. (5.9) reduces to

$$\frac{\partial \rho}{\partial x}(\alpha + \Omega)y + \frac{\partial \rho}{\partial y}(\alpha - \Omega)x = 0. \tag{5.11}$$

Eq. (5.10) reduces to

$$\begin{aligned} \frac{g}{m}\frac{\partial \rho}{\partial x} &= -\frac{1}{m}\frac{\partial V}{\partial x} + (2\alpha\Omega - \alpha^2)x, \\ \frac{g}{m}\frac{\partial \rho}{\partial y} &= -\frac{1}{m}\frac{\partial V}{\partial y} - (2\alpha\Omega + \alpha^2)y. \end{aligned} \tag{5.12}$$

Consequently we obtain

$$\frac{\Omega - \alpha}{\Omega + \alpha}\frac{x}{y} = \frac{\frac{1}{m}\frac{\partial V}{\partial x} + (\alpha^2 - 2\alpha\Omega)x}{\frac{1}{m}\frac{\partial V}{\partial y} + (\alpha^2 + 2\alpha\Omega)y} = \frac{(\omega_x^2 + \alpha^2 - 2\alpha\Omega)x}{(\omega_y^2 + \alpha^2 + 2\alpha\Omega)y} \quad \Rightarrow \quad \frac{\Omega - \alpha}{\Omega + \alpha} = \frac{\omega_x^2 + \alpha^2 - 2\alpha\Omega}{\omega_y^2 + \alpha^2 + 2\alpha\Omega} \tag{5.13}$$

Hence the α satisfies a cubic equation

$$2\alpha^3 + (\omega_x^2 + \omega_y^2 - 4\Omega^2)\alpha + \Omega(\omega_x^2 - \omega_y^2) = 0. \tag{5.14}$$

Under the low Ω limit, write $\alpha = \delta\Omega$ and keep only linear term of Ω, we obtain

$$\delta = \frac{\omega_x^2 - \omega_y^2}{\omega_x^2 + \omega_y^2} \quad \Rightarrow \quad \mathbf{v} = \Omega\frac{\omega_x^2 - \omega_y^2}{\omega_x^2 + \omega_y^2}\boldsymbol{\nabla}(xy) \tag{5.15}$$

5.2.3.2 Rotating Trap Experimental Verification

The overcritical transient velocity field has a similar irrotational quadrupular pattern $\mathbf{v} \propto \boldsymbol{\nabla}(xy)$, and it is easier to measure because of the faster motion inside the fluid. The transient behavior is first studied from a GPE simulation and then measured experimentally.

Experimental procedure Atoms were prepared in a harmonic trap with frequencies $(\omega_x, \omega_y) = 2\pi \times (40, 50)$ Hz, where the XY plane potential was generated by the confining DMD. In our case the steady-state solution would limit the rotation frequency to $\Omega \lesssim 2\pi \times 40$ Hz, leading to typical speeds $|\mathbf{v}| \sim 0.25$ mm/s. To obtain an increased signal, we focused on overcritical systems with $\Omega = 2\pi \times 50$ Hz, for which $|\mathbf{v}| \approx 0.7$ mm/s. Experimentally we began with static systems, then linearly increased the angular frequency from zero to Ω in 15 ms, held Ω constant for 2 ms (at which time the BEC rotated by an angle $\theta = \pi/2$) and then performed PIV.

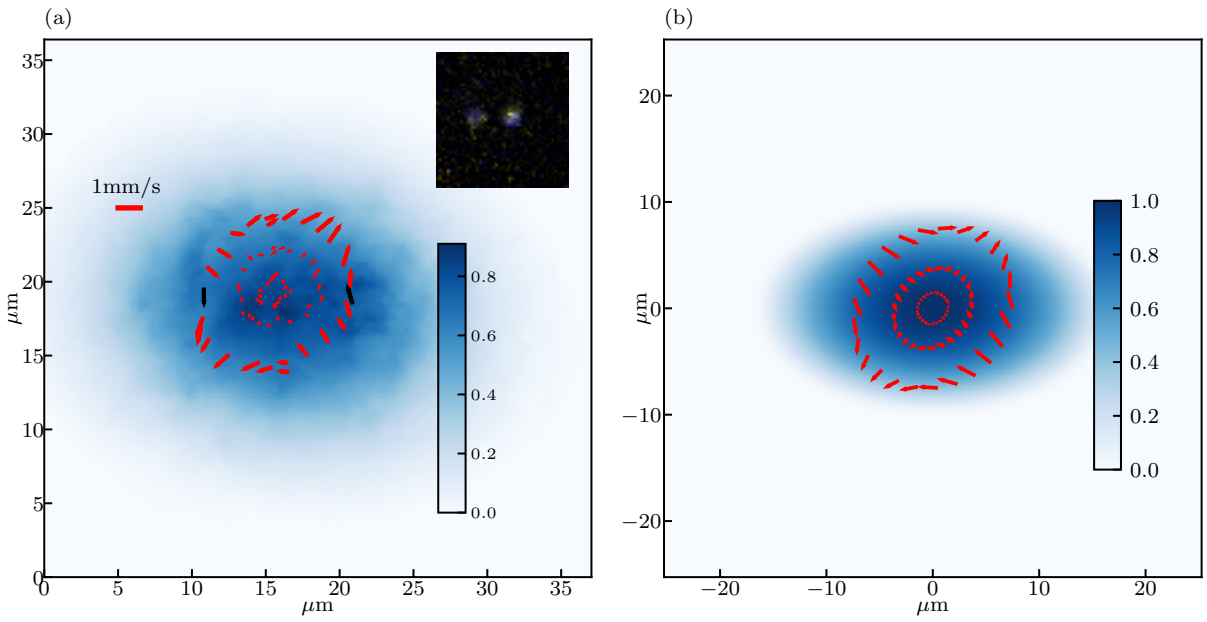

Figure 5.4: Rotating harmonic trap flow field measurement using PIV. (a) shows measured the velocity field of a rotating harmonic trap. The inlet shows the tracer particles motion of the black arrow. The arrow end is the tracer's initial position and the arrow head is the final position after 1.5 ms. The color scale shows the experimental optical density from PTAI. (b) shows the velocity field from the GPE simulation under the same case as (a). The color scale is rescaled to agree with the measurement in (a).

In Fig. 5.4(a), we illustrate the velocity field across three circles with diameters of 2, 5, and 10 μm. The tracer pattern comprises two squares, each with a side length of 2.2 μm, positioned with spatial separations of 5 μm or 10 μm. In particular, on the smallest circle with a 2 μm

diameter, the tracer pattern is a single square due to the resolution limit. We systematically scanned these patterns by rotating them around the center of each circle in increments of 15°. This process was repeated six times for each pattern, under two conditions: a wait time (Δt) of 0 and 1.5 ms. Fig. 5.4(b) shows the Gross-Piteavskii equation (GPE) simulation for comparison.

The irrotational quadrupole velocity field is clearly observed in the 5 μm and 10 μm circles. This is the first known direct visualization of an irrotational atomic superfluid, confirming the validity of our method for subsequent turbulence studies.

Chapter 6: Turbulence experiments in atomic BEC

In this chapter, I will introduce the velocity structure function (VSF) measurement using Raman PIV in a turbulent BEC and compare it to the K41 theory. Also, the intermittency is observed from the high order of VSFs and fat-tailed of the velocity increment probability density function (VI-PDF).

6.1 Turbulence Generation

Because Kolmogorov theory is valid for isotropic homogeneous systems, we turned our attention to near-ground state BECs with uniform atomic density. We employed the confining DMD to create a time-independent 2D disk-shaped potential $V(\mathbf{r}) = V_0\Theta(|\mathbf{r}| - r_0)$ with radius $r_0 = 22\ \mu\mathrm{m}$ and depth $V_0 \gg \mu$, where $\mu \approx h \times 550\ \mathrm{Hz}$ is the chemical potential. [1]

We then initialized turbulence with a pair of counter-rotating stirring "rods," with $3.5\ \mu\mathrm{m}$ radii (also created by the confining DMD) that locally depleted the atomic density. As shown in Fig. 6.1, the initially overlapping rods followed nominally circular trajectories (red curves, with a $25\ \mathrm{Hz}$ rotational frequency) in which the radius changed every $400\ \mu\mathrm{s}$ to a random value in the interval $[12\ \mu\mathrm{m}, 15\ \mu\mathrm{m}]$. The stirring potential was applied for $16\ \mathrm{ms}$, the system was then

[1] The speed of sound is $c = 1.3\ \mathrm{mm/s}$, meaured within a square box potential with roughly the same size of the disk, since the atoms are vertically confined within a harmonic trap of $\omega_z = 2\pi \times 220\ \mathrm{Hz}$ which is less than $mc^2 = h \times 368\ \mathrm{Hz}$, and thereby we need add an additional geometric factor $\frac{3}{2}$ to obtain the chemical potential $\mu = \frac{3}{2}mc^2 = h \times 553\ \mathrm{Hz}$.

allowed to equilibrate for $40\ \mathrm{ms}$ prior to PIV measurement (with $\Delta t = 0.3\,\mathrm{ms}$ evolution time).

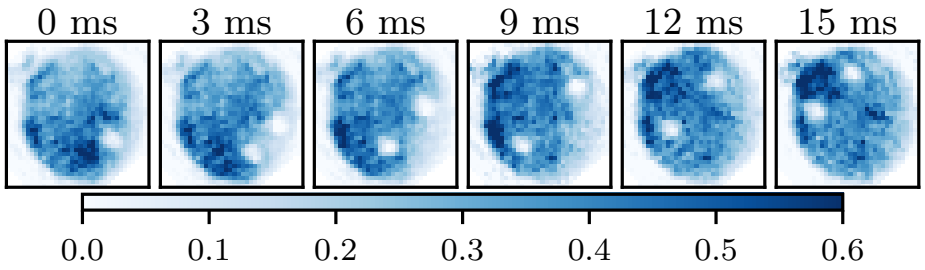

Figure 6.1: Turbulence initialization. Atomic density measured at at six times during the excitation process. Two counter-rotating stirring rods are moved in the condensates. The color bar is the optical density from PTAI measurements.

6.2 Velocity Increments Dataset Collection

We used tracer patterns consisting of $N = 4$ tracers arrayed in a square [Fig. 6.2] with three different side-lengths: $10.6\,\mu\mathrm{m}$, $11.4\,\mu\mathrm{m}$, and $12.6\,\mu\mathrm{m}$. Together these patterns gave access to six tracer separations l comprising the side as well as the diagonal lengths. To obtain the structure functions which are an ensemble average of various powers of the velocity increments, each pattern was repeated ≈ 50 times. [2]

The tracer positions $\mathbf{r}^j$ were determined as their centers of mass (COM) $\overline{\rho^j \mathbf{r}}/\overline{\rho^j}$. To first order in Δt the resulting velocity is the density-weighted (or Favre-averaged [48]) velocity $\widetilde{\mathbf{v}} = \overline{\rho \mathbf{v}}/\overline{\rho}$, used when applying Kolmogorov theory to compressible fluids [47, 49, 50] (we omit the tilde in what follows). Each measurement yielded 12 velocity increments $\delta \mathbf{v}_{\mathbf{l}^{ij}}(\mathbf{r}^j)$: with $\mathbf{r}^j$ associated with each tracer, and $\mathbf{l}^{ij} = \mathbf{r}_0^i - \mathbf{r}_0^j$ connecting to the remaining tracers.

We repeat the above procedure 44 times over eight days, so we obtain velocity increments

[2] The initial position $\mathbf{r}_0$ and final position $\mathbf{r}$ with $\Delta t = 0.3\ \mathrm{ms}$ of the trace were measured in a same experiment sequence. We first measured $\mathbf{r}$ and then waited for $10\ \mathrm{ms}$ to measure $\mathbf{r}_0$.

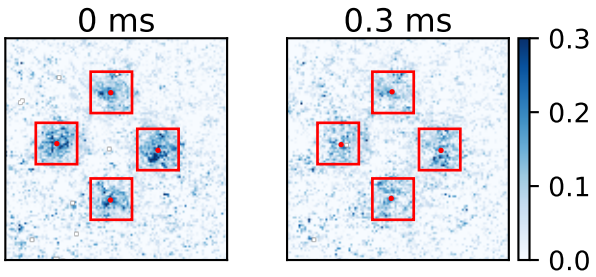

Figure 6.2: An example of Tracer patterns. Tracers are positioned on a squared array, each side measuring $12.6\,\mu\mathrm{m}$. The left shows the position where the tracers are originally injected and the right represents the tracers' position with a time interval $\Delta t = 0.3\,\mathrm{ms}$ compared to the left. The red squares outline each region of interest (ROI), within which the red dots indicate the center of mass used for velocity field calculation. The color bar is the optical density from the PTAI measurements.

Runs	l_1	l_2	l_3	l_4	l_5	l_6
1	$\{\delta^{[1]}_{(1)}\mathbf{v}_{n_1}\}$	$\{\delta^{[1]}_{(2)}\mathbf{v}_{n_2}\}$	$\{\delta^{[1]}_{(3)}\mathbf{v}_{n_3}\}$	$\{\delta^{[1]}_{(4)}\mathbf{v}_{n_4}\}$	$\{\delta^{[1]}_{(5)}\mathbf{v}_{n_5}\}$	$\{\delta^{[1]}_{(6)}\mathbf{v}_{n_6}\}$
2	$\{\delta^{[2]}_{(1)}\mathbf{v}_{n_1}\}$	$\{\delta^{[2]}_{(2)}\mathbf{v}_{n_2}\}$	$\{\delta^{[2]}_{(3)}\mathbf{v}_{n_3}\}$	$\{\delta^{[2]}_{(4)}\mathbf{v}_{n_4}\}$	$\{\delta^{[2]}_{(5)}\mathbf{v}_{n_5}\}$	$\{\delta^{[2]}_{(6)}\mathbf{v}_{n_6}\}$
⋮	⋮	⋮	⋮	⋮	⋮	⋮
44	$\{\delta^{[44]}_{(1)}\mathbf{v}_{n_1}\}$	$\{\delta^{[44]}_{(2)}\mathbf{v}_{n_2}\}$	$\{\delta^{[44]}_{(3)}\mathbf{v}_{n_3}\}$	$\{\delta^{[44]}_{(4)}\mathbf{v}_{n_4}\}$	$\{\delta^{[44]}_{(5)}\mathbf{v}_{n_5}\}$	$\{\delta^{[44]}_{(6)}\mathbf{v}_{n_6}\}$

Table 6.1: Velocity increments dataset. The dataset covers six distinct tracer separations from the squared array pattern, i.e., $(l_1, l_2, l_3, l_4, l_5, l_6) = (10.6, 11.4, 12.6, 15.0, 16.1, 17.8)\mu\mathrm{m}$. Velocity increments data is labeled as $\delta^{[i]}_{(j)}\mathbf{v}_{n_j}$, where $i = 1..44$ is the index of the experimental run, and $j = 1..6$ is the index of the tracer separation l_j. $n_j = 1.. \approx 200$ for $j = 1, 2, 3$ and $n_j = 1.. \approx 100$ for $j = 4, 5, 6$ since in each experimental run, the measurement is repeated for ≈ 50 times for each tracer pattern which consists 4 data points for the square side ($j = 1, 2, 3$) and 2 for the square diagonal ($j = 4, 5, 6$).

datasets shown in Table. 6.1.

6.3 Structure functions

The structure functions we focus on includes the longitudinal $S^L_p(l) = \langle|\delta\mathbf{v}(\mathbf{x}, \mathbf{l})\cdot\mathbf{e}_l|^p\rangle$, transverse $S^T_p(l) = \langle|\delta\mathbf{v}(\mathbf{x}, \mathbf{l})\cdot\mathbf{e}_\perp|^p\rangle$, and scalar $S^S_p(l) = \langle|\delta\mathbf{v}(\mathbf{x}, \mathbf{l})|^p\rangle$ VSFs. The average $\langle\cdots\rangle$ is the ensemble average over all positions $\mathbf{x}$ and displacement directions $\mathbf{e}_l$. Please note the absolute value is used in the definition of the structure function which is commonly used in turbulence

experiments.

Historically, the second- and third-order structure functions are most frequently discussed in the literature, since the second-order structure function is directly related to the kinetic energy spectrum, and the third-order structure function gives the four-fifth law (section. 3.1.4.4), which is an exact result derived by Kolmogorov. So we will discuss them in detail, and then discuss the higher-order structure function to see the deviation from the K41 scaling.

6.3.1 Third order structure function (S_3)

K41 predicts $S_p(l) \propto l^{(p/3)}$, so it would be easy to start with the case of $p = 3$ in which S_3 is linear to l. Data points of S_3 in Fig. 6.3 results from the velocity increments dataset in

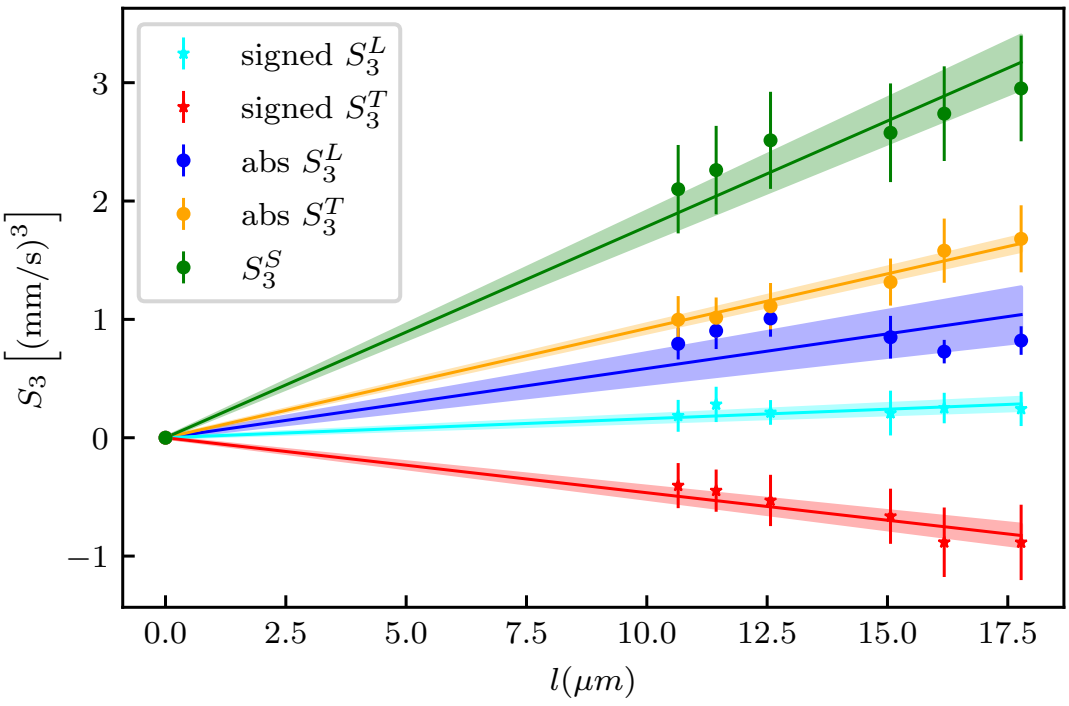

Figure 6.3: Measured $S_3(l)$. Data point results from the average of 44 experimental runs, each of which derived $S_3(l)$ from about 50 nominally identical experimental repetitions. The uncertainties are the two-sigma standard error of the mean across the set of experimental runs, and lines are fitted to the data plotted along with their $2-\sigma$ uncertainty band.

section. 6.2. The dot points are the absolute value structure function, here we also add asterisk points for the signed structure function without the absolute value to compare to the Kolmogorov four-fifth law. Here the error bar stands for the 95 percent confidence interval, which is two-sigma standard error of the mean across the set of experimental runs. [3] The shaded area gives the $2-\sigma$ uncertainty for the linear fit. Note that the linear fit passes the origin, since from the definition $|\delta\mathbf{v}(l=0)|=0$.

The scalar S_3^S (green) agrees well with the linear relationship, while the transverse and longitudinal ones are slightly off. The absolute value of S_3^T is typically slightly greater than that of S_3^L, which aligns with our observations.

From the four-fifth law $S_3(l)=-\frac{4}{5}\epsilon l$ we can estimate the dissipation rate ϵ in the system. Here we used the mean of the signed S_3^L and S_3^T as the signed S_3 for estimation, then the dissipation rate $\epsilon\approx 10^{-5}\mathrm{m}^2/\mathrm{s}^3$. We did not observe the anticipated negative slope in the signed longitudinal structure function, S_3^L, and notably, the signed transverse structure function, S_3^T, exhibited a higher degree of asymmetry compared to S_3^L, which was unexpected [87].

6.3.2 Second order of structure function (S_2)

The K41 theory did not originally predict $S_2(l)\propto l^{2/3}$. Rather, this relationship, known as the two-thirds law, is an empirical finding from experimental observations, as discussed in section. 3.1.4.2. Any theory of turbulence, including the K41 theory, must first align with this empirically established law.

Moreover, S_2 is directly related to the kinetic energy spectrum, and the famous Kolmogorov

[3] Assuming the data points follows normal distribution, then the 95 percent confidence interval for n data points is $t_{n-1}(0.025)\sigma.\sqrt{n}$, where σ is the standard deviation and $t_{45}(0.025)\approx 2$. Although the velocity increments PDF has non-Gaussian feature, it is still near-Gaussian in our case as shown in Fig. 6.8, so the normal distribution assumption is reasonable.

scaling $E(k) \propto k^{-5/3}$ can be derived from that. Since our PIV experiments are restricted to 2D, I will elaborate on it in 2D.

6.3.2.1 Relation between S_2 and kinetic energy spectrum

The first thing worth noting is that the kinetic energy spectrum in the turbulence study is power spectrum of the velocity field rather than the Fourier spectrum of kinetic energy, i.e.,

$$E(\mathbf{k}) = |\mathrm{FT}[v_x(\mathbf{r})]|^2 + |\mathrm{FT}[v_y(\mathbf{r})]|^2 \neq |FT[v_x^2(\mathbf{r}) + v_y^2(\mathbf{r})]|, \tag{6.1}$$

where FT stands for the Fourier transform.

Second, the power spectrum $E(\mathbf{k})$ is always reduced to 1D by averaging out the angle dependence of the $\mathbf{k}$, so there is an additional k from the Jacobian so that it satisfies $\int dk E(k) = \int d^2k E(\mathbf{k})$, i.e.,

$$E(k) = \int_0^{2\pi} d\theta \, kE(k, \theta), \tag{6.2}$$

where (k, θ) is the polar coordinate of $\mathbf{k}$.

From Wiener-Khinchin's theorem, the autocorrelation of the velocity field is the Fourier transform of the power spectrum, i.e.,

$$R_2(\mathbf{r}) \equiv \int d^2x \, \mathbf{v}(\mathbf{x}+\mathbf{r}) \cdot \mathbf{v}(\mathbf{x}) = \mathrm{FT}[E(\mathbf{k})] = \int d^2k E(\mathbf{k}) \cos(\mathbf{k} \cdot \mathbf{r}). \tag{6.3}$$

Here the Fourier transform reduces to the integral of cosine since the power spectrum is real symmetric.

On the other hand, the scalar $S_2^S(\mathbf{r})$ can be decomposed by the autocorrelation function,

i.e.,

$$S_2^S(\mathbf{r}) \equiv \int d^2x\, |\mathbf{v}(\mathbf{x}+\mathbf{r})-\mathbf{v}(\mathbf{x})|^2 = \int d^2x\, [\mathbf{v}^2(\mathbf{x}+\mathbf{r})+\mathbf{v}^2(\mathbf{x})-2\mathbf{v}(\mathbf{x}+\mathbf{r})\cdot\mathbf{v}(\mathbf{x})] = 2[R_2(0)-R_2(\mathbf{r})]. \tag{6.4}$$

Please note that to obtain the structure function that only depends on the magnitude of $\mathbf{r}$, we need to average out the angle dependence of $\mathbf{r}$, i.e., $S_2^S(r) = \frac{1}{2\pi}\int_0^{2\pi} d\phi\, S_2^S(\mathbf{r})$, where (r, ϕ) is the polar coordinate of $\mathbf{r}$. Combining Eq. (6.4) and Eq. (6.3), we obtain

$$S_2^S(\mathbf{r}) = 2\int d^2k[1-\cos(\mathbf{k}\cdot\mathbf{r})]E(\mathbf{k}) = 2\int kdkd\theta[1-\cos(kr\cos(\theta-\phi))]E(k,\theta) \tag{6.5}$$

We can further expand the nested cosine using the Jacobi-Anger expansion with Bessel functions and obtain

$$S_2^S(\mathbf{r}) = 2\int kdkd\theta[1-J_0(kr)-2\sum_{n=1}^{\infty}(-1)^n J_{2n}(kr)\cos(2n(\theta-\phi))]E(k,\theta). \tag{6.6}$$

If the system is isotropic, we can further reduce it to

$$S_2^S(r) = 2\int dk(1-J_0(kr))\int d\theta kE(k,\theta) = 2\int dk(1-J_0(kr))E(k), \tag{6.7}$$

where ϕ is averaged out. It is worth noting that the structure function and energy spectrum is not connected by a Fourier transform, but by a Bessel transform which is the Fourier transform of a radially symmetric function in the polar coordinate. If $E(k)$ follows $k^{-5/3}$, then

$$S_2^S(r) \propto 2r^{2/3}\int d(kr)(1-J_0(kr))(kr)^{-5/3} \propto r^{2/3}. \tag{6.8}$$

6.3.2.2 Measurement of S_2

Data points of S_2 in Fig. 6.4 results from the velocity increments dataset in section. 6.2. For an even order of structure function, we don't need to distinguish the absolute and signed structure function. The data points are fitted to the $S_2(l) = sl^{2/3}$ passing the origin, and the

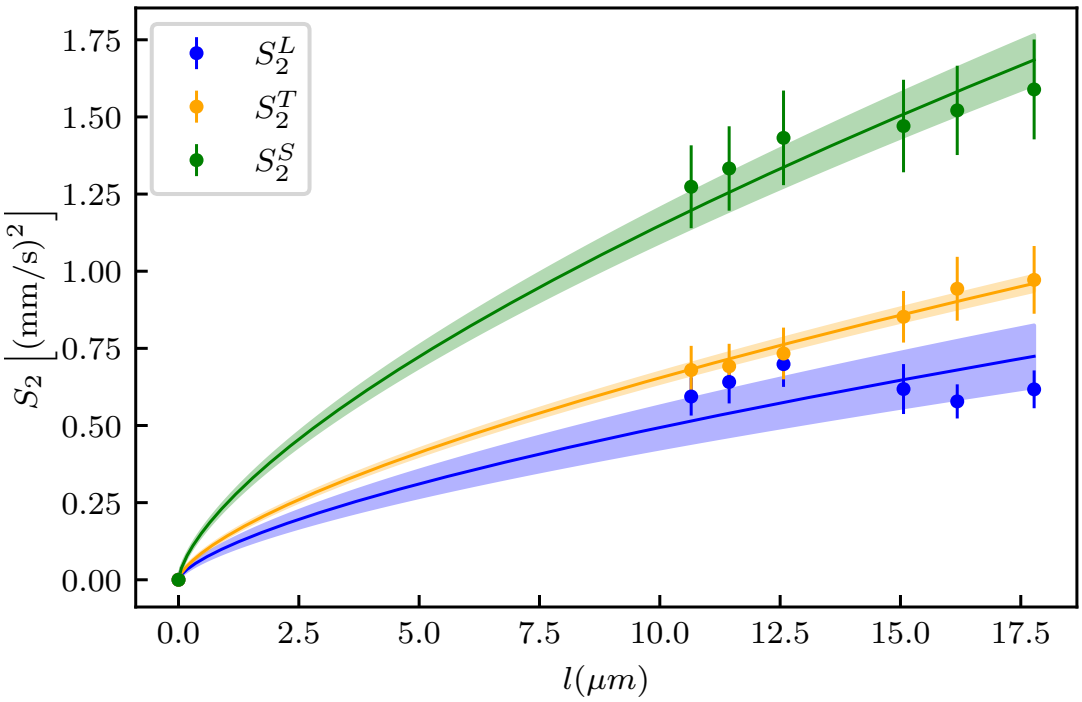

Figure 6.4: Measured $S_2(l)$. Data point results from the average of 44 experimental runs, each of which derived $S_2(l)$ from about 50 nominally identical experimental repetitions. The uncertainties are the two-sigma standard error of the mean across the set of experimental runs, and lines are fitted to the data by $l^{2/3}$ plotted along with their $2-\sigma$ uncertainty band.

error metric is the same as S_3. Similar to the measured S_3, the scalar one agrees well with $l^{2/3}$, and the longitudinal and transverse ones are slightly off. The amplitudes are $s^L = 1.06(7) \times 10^{-1}\ \mathrm{m}^{4/3}/\mathrm{s}^2$, $s^T = 1.41(2) \times 10^{-1}\ \mathrm{m}^{4/3}/\mathrm{s}^2$ and $s^S = 2.47(6) \times 10^{-1}\ \mathrm{m}^{4/3}/\mathrm{s}^2$. Transverse VSFs are generally larger than their longitudinal counterparts; for example the second order structure function has the exact relation $S_2^T(l)/S_2^L(l) = 4/3$ [88], and indeed we find $S_2^T(l)/S_2^L(l) =$

1.33(4). The good agreement of $S_2^S \propto l^{2/3}$ indicates the kinetic energy spectrum in our system follows $k^{-5/3}$ within the measured scale.

6.3.3 $S_n(l)$ for $n \leq 7$

Typically higher order structure functions have scalings deviations from the K41 scaling. As shown in Fig. 6.5(a), we obtained the scalar structure function $S_n^S(l)$ up to seventh order and fitted it to $a_n l^{\varepsilon_n}$, where ε_p is the fitted scalings.

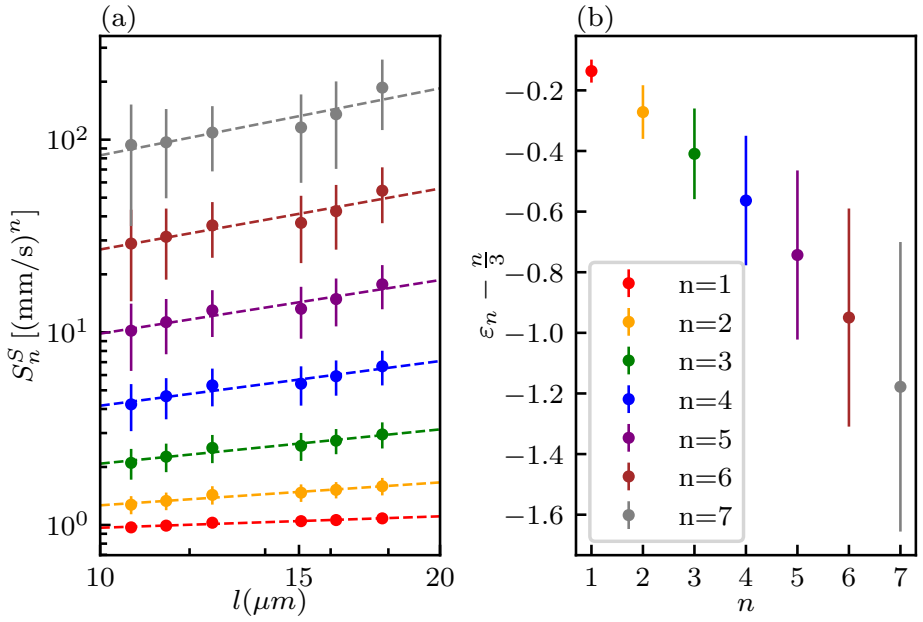

Figure 6.5: Measured $S_n^S(l)$. (a) Log-Log plot of $S_n^S(l)$, $n = 1..7$ fitted to the dashed lines $a_n l^{\varepsilon_n}$. The error bar shows the two-sigma standard error of the mean. (b) intermittency correction $\varepsilon_n - \frac{n}{3}$ versus n. The error bar is the two-sigma uncertainty of the fitting in (a).

Fig. 6.5(b) shows the deviation of the measured scaling ε_n from the K41 scaling $n/3$. We observed that the deviation increases for greater n, which is expected by the intermittency effect. K62 theory predicted that the deviation is $\propto -n(n-3)$. For our data, apart from the deviation is nonzero at $n = 3$, the quadratic deviation agrees with the prediction.

We further obtained the longitudinal and transverse structure function and the intermittency

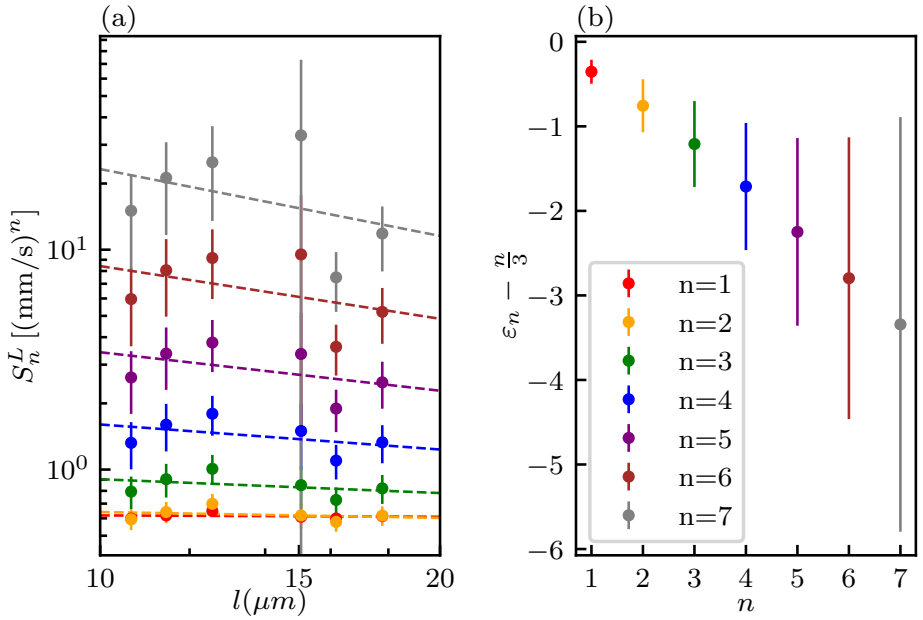

Figure 6.6: Measured $S_n^L(l)$. (a) Log-Log plot of $S_n^S(l)$, $n = 1..7$ fitted to the dashed lines $a_n l^{\varepsilon_n}$. The error bar shows the two-sigma standard error of the mean. (b) intermittency correction $\varepsilon_n - \frac{n}{3}$ versus n. The error bar is the two-sigma uncertainty of the fitting in (a).

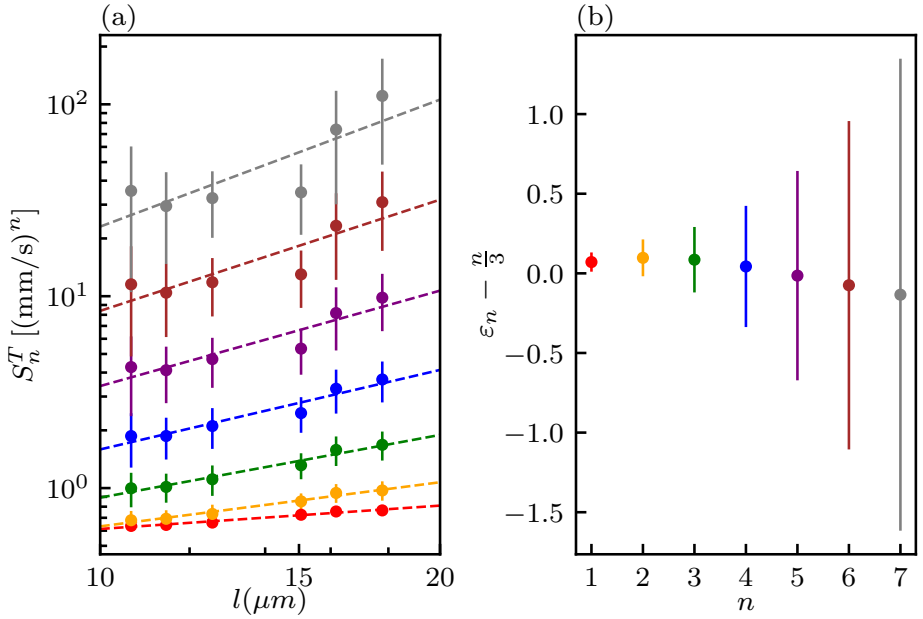

Figure 6.7: Measured $S_n^T(l)$. (a) Log-Log plot of $S_n^S(l)$, $n = 1..7$ fitted to the dashed lines $a_n l^{\varepsilon_n}$. The error bar shows the two-sigma standard error of the mean. (b) intermittency correction $\varepsilon_n - \frac{n}{3}$ versus n. The error bar is the two-sigma uncertainty of the fitting in (a).

corrections shown in Fig. 6.6 and Fig. 6.7. We observed that the longitudinal scalings are very off from the K41 scalings while the transverse scalings are quite close, which suggests anisotropy in the system.

6.4 Velocity increments PDF

Intermittency in the velocity increments PDF manifests itself as a deviation from the Kolmogorov 1941 (K41) scaling, not only observable through the higher-order structure functions but also evident in the scale dependence of the probability density functions (PDFs) themselves. As the scale decreases, the non-Gaussian characteristics of the velocity increments become increasingly pronounced, the velocity increments exhibit more extreme events than would be expected in a Gaussian distribution.

Having identified intermittency in the higher-order structure functions (section. 6.3.3), this section shifts focus to the PDFs of velocity increments (VI-PDFs), aiming to uncover further insights into the nuanced behavior of turbulent flows.

Recent measurements of the velocity PDF [61] and velocity increment PDF [89] in the superfluid ^{4}He have revealed contrasting results. At scales that exceed the average distance l_0 between quantum vortices, quantum turbulence manifests quasiclassical behavior in both its energy spectrum and velocity statistics. However, at smaller scales, the discrete essence of quantized vorticity influences the energy distribution and the frequency of high-velocity (increment) events [90]. In this work, the tracer separations are on the scale of l_0, thereby we expect that the PDF would be near-Gaussian but still have non-Gaussian heavy tails. In this section I will first introduce deconvolution used for estimation of PDF, and then discuss the non-Gaussian feature.

6.4.1 PDF from Deconvolution

In the realm of measurements, noise is an inherent component, making the observed measurement result, denoted as $\hat{M}$, a sum of the true result $\hat{R}$ and instrumental noise $\hat{N}$, as shown by:

$$\hat{M} = \hat{R} + \hat{N}, \tag{6.9}$$

where $\hat{P}$ represents the random process P, and we utilize $P(\Delta\mathbf{v})$ to denote the probability density function (PDF).

Given the additive nature of noise, the PDF adheres to a convolution relationship, expressed as:

$$M(\Delta\mathbf{v}) = [R * N](\Delta\mathbf{v}), \tag{6.10}$$

indicating that the observed PDF $M(\Delta\mathbf{v})$ is the convolution of the true signal PDF $R(\Delta\mathbf{v})$ and the noise PDF $N(\Delta\mathbf{v})$.

To calibrate the instrumental noise distribution $N(\Delta\mathbf{v})$ in velocimetry, we analyze the velocity increments distribution $M_{BEC}(\Delta\mathbf{v})$ of an unstirred Bose-Einstein condensate (BEC) shown in Fig. 6.8. Theoretically, the real distribution $R_{BEC}(\Delta\mathbf{v})$ for the BEC's ground state should resemble a Dirac-δ function centered at $\Delta\mathbf{v} = 0$, leading to the conclusion that $N(\Delta\mathbf{v}) = M_{BEC}(\Delta\mathbf{v})$.

For a turbulent BEC, the measured velocity increments distribution is $M_{turb}(\Delta\mathbf{v})$ shown in Fig. 6.8. The challenge is to deconvolve this measurement by the instrumental noise N to

uncover the real PDF, R_{turb}. While a direct approach involves Fourier transforms, where

$$R_{turb} = \mathrm{FT}^{-1}\left[\frac{\mathrm{FT}[M_{turb}]}{\mathrm{FT}[N]}\right], \tag{6.11}$$

this method does not guarantee the resultant PDF will remain non-negative, a necessary condition for real PDFs.

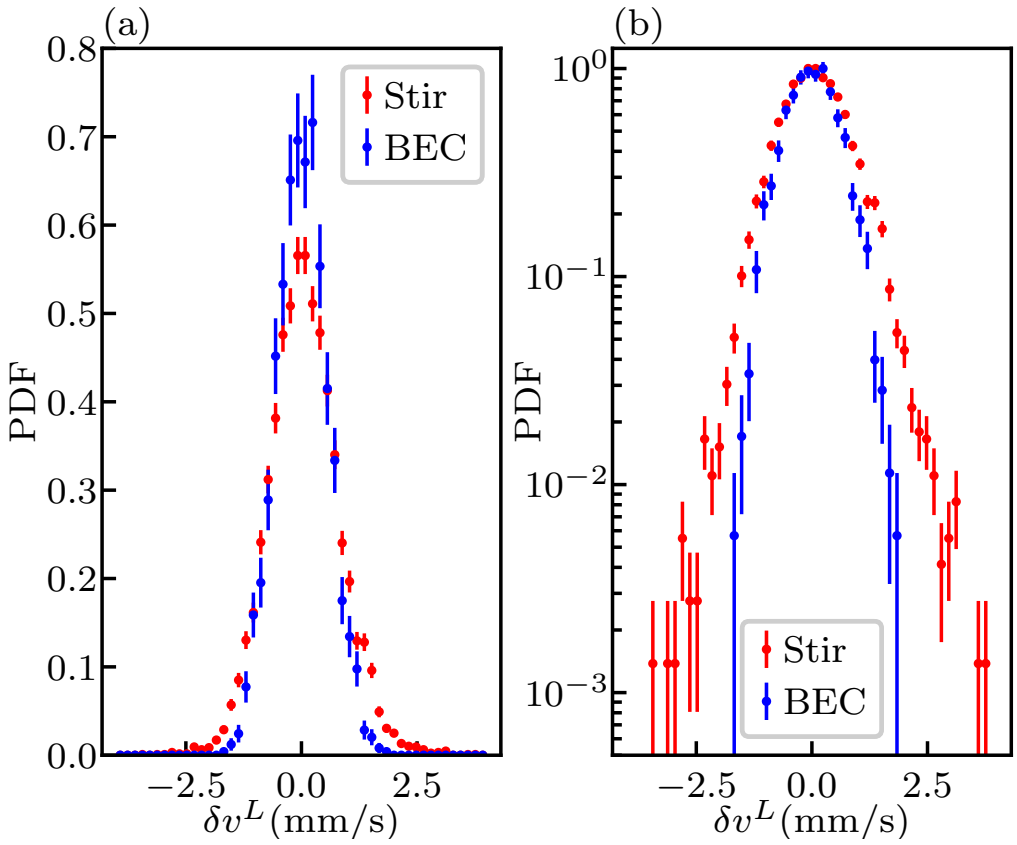

Figure 6.8: Histograms of longitudinal velocity increments at $l = 10.6\,\mu\mathrm{m}$ for unstirred (blue) and stirred (red) Bose-Einstein condensates (BECs). Panel (a) shows normalized PDFs in linear scale, while panel (b) displays PDFs rescaled to peak at 1 in log scale. Error bars indicate $\sqrt{n}$ statistical counting errors.

To address this, we employ quadratic programming for deconvolution [91], a method that will be detailed in the following section. This approach offers a more robust solution by ensuring that the deconvolved PDF, R_{turb}, maintains its non-negativity, aligning with the inherent

characteristics of probability distributions.

6.4.1.1 Quadratic Programming

Quadratic programming (QP) is a powerful optimization framework ideal for addressing problems where the objective function is quadratic and the constraints are linear. In the context of deconvolving a probability density function (PDF) from observed data contaminated with noise, QP offers an efficient and precise method. The core challenge involves extracting the true signal PDF, $R_{turb}(\Delta v)$, from the observed measurements, $M_{turb}(\Delta v)$, which are convolved with instrumental noise. For simplicity, we denote R_{turb} and M_{turb} as R and M respectively when the context is clear.

The deconvolution task can be elegantly formulated as an optimization problem within the QP framework. This is achieved by minimizing the following quadratic objective function:

$$||M - CR||^2 = -2(M^T C)R + R^T(C^T C)R, \tag{6.12}$$

where C represents the convolution matrix derived from the discretized instrumental noise across k bins, and is defined as:

$$C = \delta \begin{pmatrix} N(\Delta v_1 - \Delta v_1) & \dots & N(\Delta v_1 - \Delta v_k) \\ \vdots & \ddots & \vdots \\ N(\Delta v_k - \Delta v_1) & \dots & N(\Delta v_k - \Delta v_k) \end{pmatrix}, \quad \delta = \Delta v_{i+1} - \Delta v_i \tag{6.13}$$

with δ specifying the uniform spacing between velocity increments bins. R and M are represented

in vector form as:

$$R = \begin{pmatrix} R(\Delta v_1) \\ \vdots \\ R(\Delta v_k) \end{pmatrix}, \quad M = \begin{pmatrix} M(\Delta v_1) \\ \vdots \\ M(\Delta v_k) \end{pmatrix} \tag{6.14}$$

The optimization is subject to linear constraints ensuring that the PDF, R, is non-negative and normalized, formalized as:

$$\delta I^T R = 1, \quad R \geq 0. \tag{6.15}$$

By casting the deconvolution problem in terms of QP from the onset, we not only simplify the formulation of the deconvolution problem but also ensure that the solution, R, adheres to the fundamental properties of PDFs.

6.4.1.2 Velocity increments PDF after Deconvolution

In Fig. 6.9, we present the probability density function (PDF) for the stirred Bose-Einstein Condensate (BEC) as depicted in Fig. 6.8, alongside its deconvolved version achieved through quadratic programming [92]. Notably, Fig. 6.9(b) reveals the presence of non-Gaussian fat tails in the PDF, particularly in the rare-event region, where the probability exceeds that of the Gaussian distribution, as depicted by the black parabola. While the central portion of the PDF exhibits a mild negative skewness, this skewness becomes less discernible within the rare-event region. The deviation from Gaussian behavior is further analyzed and quantified in the subsequent section.

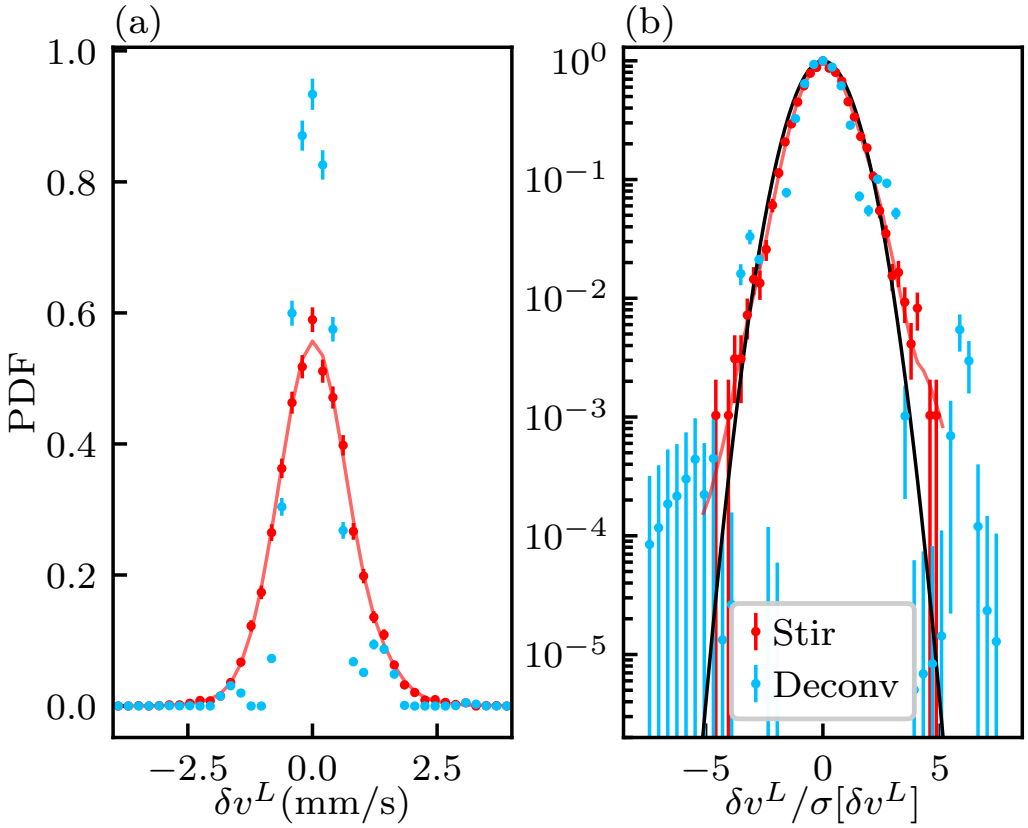

Figure 6.9: Histograms of longitudinal velocity increments at $l = 10.6\,\mu$m for stirred BECs (red) and their deconvolved versions (light blue), with the red curve illustrating the convolution of instrumental noise with the deconvolved PDF. Panel (a) displays PDFs normalized in linear scale, while panel (b) shows PDFs rescaled to peak at 1 in log scale, with velocity increments rescaled by the standard deviation. The black curve represents the normal distribution. Error bars denote statistical counting errors, given by $\sqrt{n}$.

6.4.2 Non-Gaussian Statistics

The non-Gaussian characteristics of a dataset can be effectively quantified and observed through statistical measures such as kurtosis [93] and the Jarque-Bera (JB) statistic [94]. Kurtosis, defined as $K \equiv \mu_4/\sigma^4$, measures the "tailedness" of a probability distribution, where μ_4 is the fourth central moment and σ is the standard deviation. For a perfectly Gaussian (normal) distribution, the kurtosis is 3. Deviations from this value indicate non-Gaussian features; specifically, a kurtosis greater than 3 suggests a distribution with fatter tails than a normal distribution (leptokurtic),

and a kurtosis less than 3 indicates thinner tails (platykurtic).

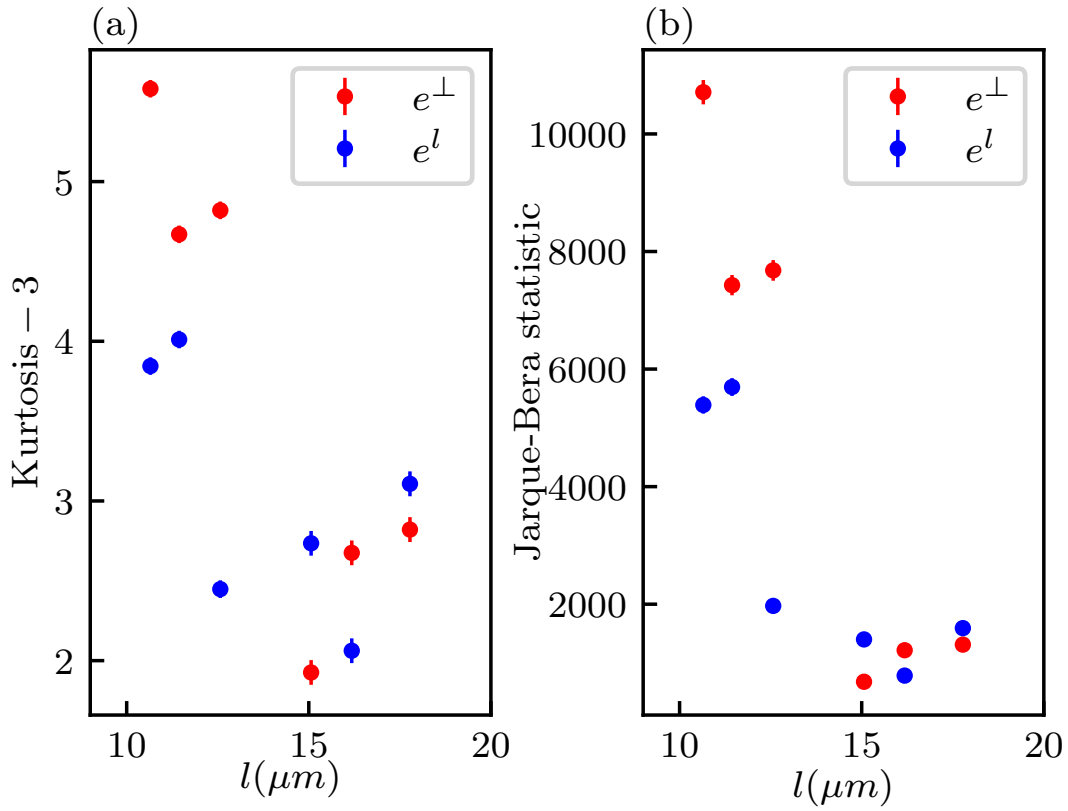

Figure 6.10: Kurtosis and Jarque-Bera (JB) Statistic of the deconvolved PDF as Functions of Positional Separations. Red and blue denote the transverse and longitudinal direction, respectively. The error bars indicate the standard error [2].

The Jarque-Bera statistic provides a composite measure of deviation from normality, combining both skewness ($S \equiv \mu_3/\sigma^3$) and excess kurtosis $K-3$ into a single statistic, where μ_3 is the third order central moment. The JB statistic is calculated as

$$\text{JB} = \frac{N}{6}\left(S^2 + \frac{1}{4}(K-3)^2\right) \tag{6.16}$$

where N is the sample size. A distribution that perfectly follows a normal distribution would have a JB statistic of zero. Higher values of the JB statistic indicate a greater departure from normality, capturing asymmetry (through skewness) and the heaviness of tails (through kurtosis)

in the distribution.

We calculated the kurtosis and JB of the deconvolved PDF and presented in Fig. 6.10. The observation that non-Gaussian characteristics become more pronounced at smaller scales l aligns with our expectations regarding intermittency in turbulence statistics. This scale-dependent manifestation of non-Gaussian features is a hallmark of the intermittent nature of turbulent flows.

6.4.3 Structure Function after Deconvolution

From the deconvolved probability density functions for both longitudinal and transverse velocity increments, $R_l(\Delta v)$, at various positional separations l, we derive the p-th order structure function as follows:

$$S_p(l) = \int_{-\infty}^{+\infty} d\Delta v \, (\Delta v)^p R_l(\Delta v). \tag{6.17}$$

To construct the scalar structure function, it is necessary to consider the longitudinal and transverse velocity increments as independent variables. This involves obtaining a two-dimensional (2D) PDF, $R_l(\Delta v^L, \Delta v^T)$, through 2D deconvolution employing quadratic programming (QP).

Fig. 6.11 illustrates the scalar structure function, where the intermittency correction, $\varepsilon_n - n/3$, is fitted the K62 theory, expressed as $-\mu n(n-3)$. This fit yields an intermittency exponent $\mu = 0.041(8)$, indicating a quantifiable measure of the deviation from K41 theory due to intermittency effects.

6.5 Numerical Simulation of the stirring turbulence

Numerical GPE simulation is the typical way for atomic BEC hydrodynamics simulation; however, it does not include the dissipation, thereby it cannot have a scaling the same as Kolmogorov's

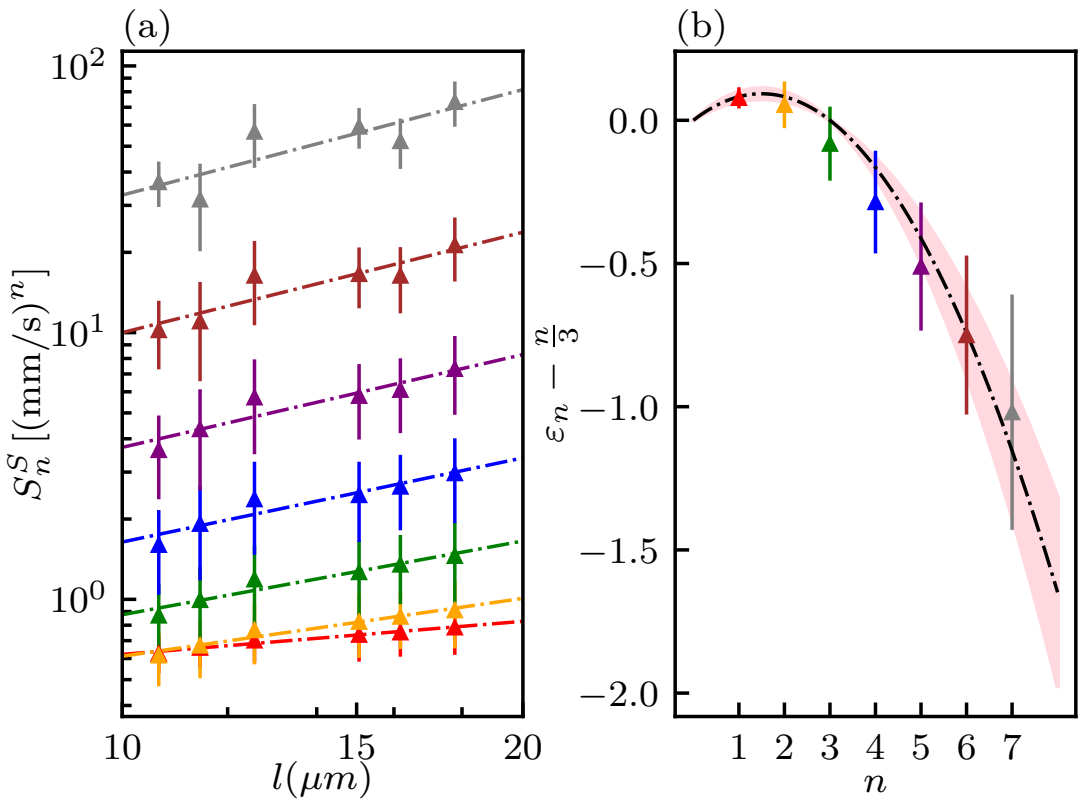

Figure 6.11: (a) Log-Log plot of deconvolved $S_n^S(l)$, $n = 1..7$ fitted to the dashed lines $a_n l^{\varepsilon_n}$. The error bars are estimated from the $\sqrt{n}$ statistical counting error. (b) intermittency correction $\varepsilon_n - \frac{n}{3}$ versus n. The error bar is the two-sigma uncertainty of the fitting in (a). The black dashed line represents the fit to the K62 theory, expressed as $-\mu n(n-3)$, where the pink shaded area denotes the standard error of the fitting.

prediction. Since in the inertial range theory, the dissipation is negligible in large scale, so here we add an additional dissipation term that only exists in the small scale. The detail of this numerical scheme will be introduced in this section.

But before that, I want to discuss the dissipation in our experimental system. Our atomic BECs are confined in a homogenous disc trap in the XY plance with an additional z confinement with trap frequency $\omega_z = 2\pi \times 220\,\mathrm{Hz}$. The XY confinement potential is much greater than the chemical potential $\mu \approx h \times 550\,\mathrm{Hz}$, so the atoms loss in the XY plane is negligible. Conversely, The lowest unstable collective mode frequency in the z direction has a frequency of $2\omega_z$, so all

of the xy excitations with energy below that should be fairly stable, however, the $2\hbar\omega_z$ of energy brings that unstable mode quite close to the trap depth, allowing it to evaporate.

So we can estimate the cutoff wavevector for dissipation via

$$k_{\text{cutoff}} = \frac{2\omega_z}{c} = 2\omega_z\sqrt{\frac{3m}{2\mu}} = \frac{2\sqrt{3}\omega_z m\xi}{\hbar} = 2\sqrt{3}\frac{\xi}{\ell^2_{\text{ho,z}}}, \tag{6.18}$$

$$\xi k_{\text{cutoff}} = 2\sqrt{3}\left(\frac{\xi}{\ell_{\text{ho,z}}}\right)^2, \tag{6.19}$$

where c is the speed of sound, $\xi = \sqrt{\hbar^2/2m\mu} \approx 325\,\text{nm}$ is the healing length, and $\ell_{\text{ho,z}} = \sqrt{\hbar/(m\omega_z)} = 727$ nm, so we get $\xi k_{\text{cutoff}} \approx 0.7$. This value will be used in the following dissipative GPE simulations.

6.5.1 Numerical dissipative GPE scheme

A numerical simulation using GPE with small-scale dissipation [95],

$$(i - \tilde{\gamma}(\mathbf{k}))\,\hbar\partial_t\tilde{\psi}(\mathbf{k},t) = [\hbar^2k^2/2m - \mu(t)]\tilde{\psi}(\mathbf{k},t) + \tilde{h}(\mathbf{k},t),$$

is implemented to reveal the Kolmogorov scaling law for the exact stirring sequence in the experiment where $h(\mathbf{k},t)$ is the fourier transform of $h(\mathbf{x},t) = gN|\psi(\mathbf{x},t)|^2\psi(\mathbf{x},t) + V_{ext}(\mathbf{x},t)\psi(\mathbf{x},t)$, μ is the chemical potential, and $\tilde{\gamma}(\mathbf{k}) = \gamma_0\theta(k - 2\pi s/\xi)$ is the dissipation term. The dissipation term does not conserve number of particles, however, we normalized the wavefunction at each time step, so the chemical potential is time dependent to conserve number of particles. Here, the dissipation term removes excitations with wavelengths smaller than ξ/s, where ϵ is the healing length, s and γ_0 is a free tuning parameter and θ is the Heaviside function. The previous section

estimates the $k_{\text{cutoff}} \approx 0.7/\xi$, thereby we use $s = 0.7/2\pi \approx 0.11$ for the following simulations.

The calculation flowchart would be (i) Calculate $\mu(t)$ and $h(\mathbf{x}, t)$ from $\psi(\mathbf{x}, t)$ (ii) Calculate $\tilde{h}(\mathbf{k}, t)$ by 2d fft. (iii) calculate $\tilde{\psi}(\mathbf{k}, t + \Delta t)$ using

$$(i - \tilde{\gamma}(\mathbf{k}))\, \hbar \partial_t \tilde{\psi}(\mathbf{k}, t) = [\hbar^2 k^2/2m - \mu(t)]\tilde{\psi}(\mathbf{k}, t) + \tilde{h}(\mathbf{k}, t)$$

by a fourth-order Runge-Kutta(RK4) method.

The initial state of the wavefunction was prepared as follows. We first calculated ψ_{gnd}, the zero-temperature ground state wavefunction without dissipation, from the imaginary evolution of GPE. Then we evolved ψ_{gnd} under a stochastic GPE in real-time for several seconds to obtain the initial state ψ_{init} satisfying $|\langle \psi_{\text{init}} | \psi_{\text{gnd}} \rangle|^2 \approx 0.97$.

We then evolved ψ_{init} by the dissipative GPE with stirring, following the same procedure in the experiments, i.e., stirring for 16 ms and free evolving for 40 ms.

We built up our numerical experiment ensemble with 20 experiments considering two randomnesses: (i) the initial state, (ii) the radial trajectory of the stirring rods.

6.5.2 Kinetic energy spectrum and structure functions

Since we used the center of mass to track the velocity field of the tracers in the experiment, we also used the density weighted velocity $\widetilde{v} = \overline{\rho v}/\bar{\rho}$ in the numerics for the study of the velocity field and the energy spectrum.

The kinteic energy spectrum agrees well with the Kolmogorov $-5/3$ scaling, as shown in Fig. 6.12. The green line is fitted to the spectrum within the inertial range with a scaling $-1.54(8)$. It is worth noting the k for the healing length is $1/\xi$ instead of $2\pi/\xi$, since the healing

length describes the length changes from zero to the max density without periodic features.

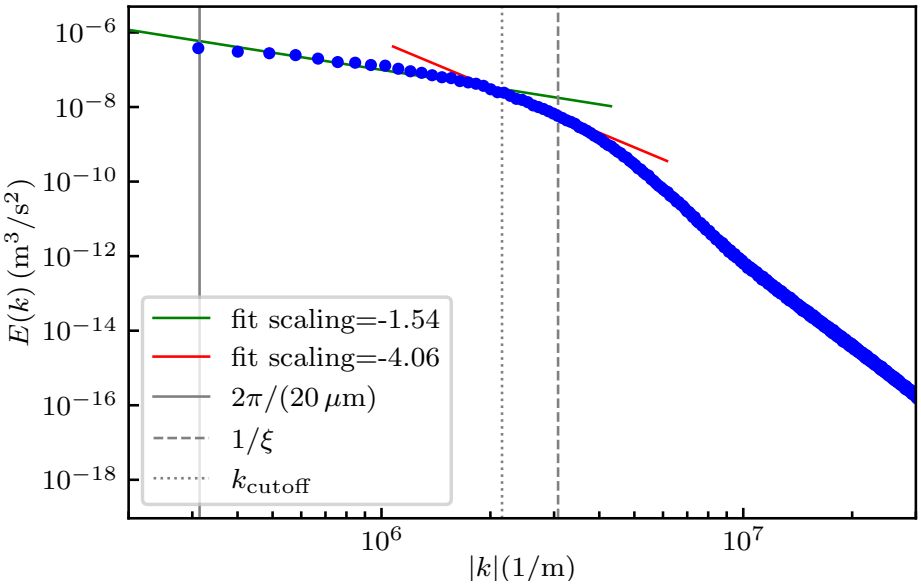

Figure 6.12: Kinetic energy spectrum corresponding to the case of turbulence freely decaying for 40ms after stirring. The blue dots represent the kinetic energy spectrum. The green line is fitted to the inertial range and the red line is fitted to the crossover range.

The second and third order of scalar structure functions are shown in Fig. 6.13, obtained from the direct computation of the numerical dataset. To compare with the experimental data, the velocity field is also calulated from the center-of-mass velocity field in a 7 μm $\times$ 7 μm region. Scaling in the experimental measured range (10.6 μm to 17.8 μm) is close to the K41 law; however, the amplitude of S_2^S is $\approx 15\%$ of the experimental data, indicating that the velocity increases from the numerical simulation are $\approx 40\%$ of the experimental data. The discrepency might result from some thermal component measured in the PIV, which is not included in the numerical scheme for zero-temperature BEC. Stochastic projected GPE for finite-temperature BEC might be a good candidate to resolve this issue. Nevertheless, the dissipative GPE scheme we employed successfully captures the scalings of the Kolmogorov spectrum and low-order structure functions.

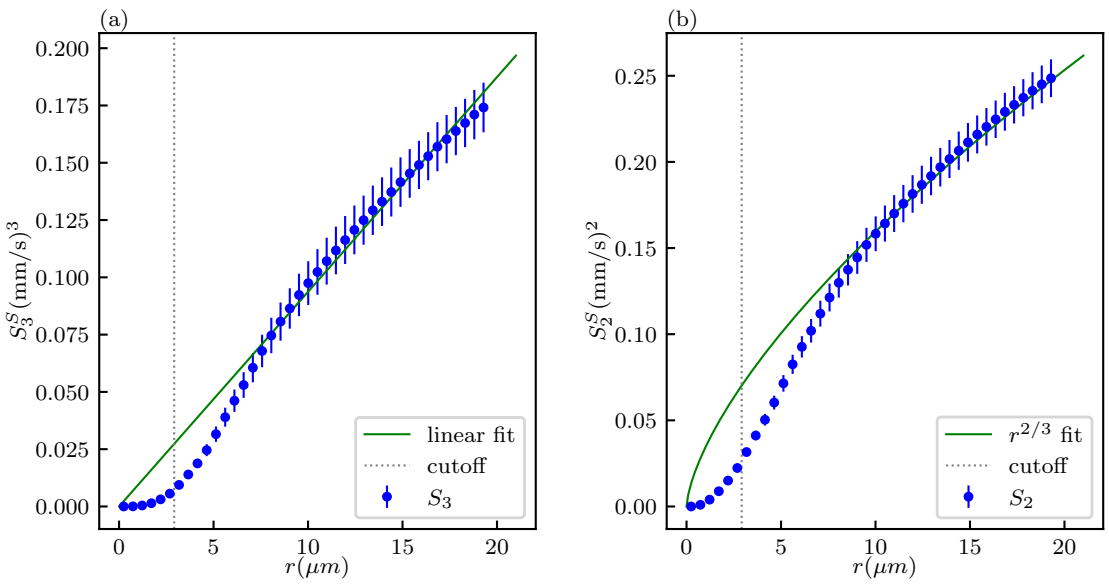

Figure 6.13: (a)Third order scalar structure function (blue) from direct calculation, and the green line shows the linear fit in the inertial range. (b)Second order scalar structure function (blue) from direct calculation, and the green curve shows the $r^{2/3}$ fit in the inertial range. The uncertainties are the two-sigma standard error of the mean across the set of numerical runs.

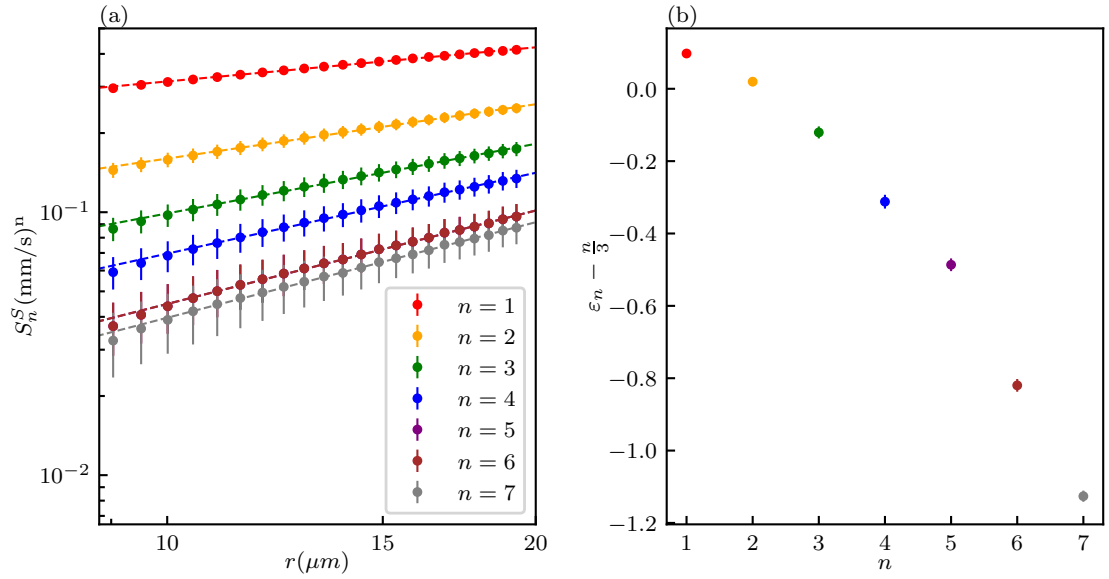

Figure 6.14: (a) Log-Log plot of $S_n^S(l)$, $n = 1..7$ fitted to the dashed lines $a_n l^{\varepsilon_n}$. The error bar shows the two-sigma standard error of the mean. (b) intermittency correction $\varepsilon_n - \frac{n}{3}$ versus n. The error bar is the two-sigma uncertainty of the fitting in (a).

We further obtained higher-order structure functions to see the effect of intermittency, as shown in Fig. 6.14. The intermittency correction is relatively larger than the experiments for higher orders.

Chapter 7: Measurement of Superfluid Density

7.1 Introduction

Superfluidity and Bose-Einstein condensation (BEC) are deeply connected. We have seen the irrotational velocity field in a rotating BEC, which suggests the superfluidity. The hydrodynamics in the BEC is typically described by the Gross-Piteavskii equation (GPE), which can be transformed into Euler equations describing inviscid fluid, thus in this case the superfluid fraction is believed to be 100%. On the other hand, GPE is a good mean-field description of the zero-temperature BEC, thereby the zero-temperature BEC also has a perfect BEC fraction, neglecting the quantum fluctuations. For finite temperature BEC, the superfluid and BEC fraction can be quite different, but under the zero-temperature limit, the BEC and superfluid fraction is always believed to be the same. In other words, in dilute atomic BECs, if you obtain a pure BEC, then the superfluid fraction is generally believed to be pure [96, 97].

On the contrary, superfluid ^{4}He can achieve a nearly $100\ \%$ superfluid fraction, with only about $14\ \%$ condensate fraction [98], and infinite 2D Berezinskii-Kosterlitz-Thouless superfluids (BKT) have no condensate at all [99, 100]. In 1970 Leggett showed that supersolids—systems spontaneously forming both superfluid and crystalline order (i.e. density modulations)—exhibit the reverse behavior: superfluid density far below the condensate density [101]. So in general, superfluid and condensate are very different concepts. Condensate describes the state that can be

described by a complex-order parameter (macroscopic wavefunction), which can be viewed as analogous to a single-particle wavefunction. The motion of the condensate can be described by the nonlinear Schrodinger equation (GPE), analogous to the motion of a single particle described by the Schrodinger equation. In this picture, the condensate motion is quite "collective", which is a simple generalization of the case of a single particle. However, superfluidity is a transport concept. In a rotating bucket experiment, the normal fluid density is determined by the fraction of fluid that is rotated along with the bucket, and the rest of the irrotational fluid is superfluid. Similarly, if you drag a pipe with the fluid filled inside, the fluid that follows the motion of the pipe is normal fluid, and the rest of the fluid that is stationary is superfluid. As you can see, the superfluid is related to the detailed transport motion, so it must depend on the excitation of the ground state.

To compare with the macroscopic wavefunction, we can introduce the superfluid order parameter. The complex-valued order parameter [38] $\phi(\mathbf{r}) = \sqrt{\rho^{\mathrm{sf}}}\exp[i\varphi(\mathbf{r})]$, which describes a superfluid with number density ρ^{sf} and phase $\varphi(\mathbf{r})$, gives rise to two hallmark superfluid properties: dissipationless supercurrents associated with spatial gradients in $\varphi(\mathbf{r})$ and (Bogoliubov [97]) phonons described by traveling waves in $\varphi(\mathbf{r})$. Because dissipationless supercurrents—both electrical and, as here, neutral—arise from phase gradients, they are locally irrotational; in liquid ^{4} He, the resulting nonclassical rotational inertia [102, 103] appears below the superfluid transition temperature T_{c}.

Supersolids are more exotic systems that spontaneously form a crystalline order while exhibiting superfluid transport properties and phase coherence [104]. Recent experiments with dipolar BECs of Dy and Er exhibit crystalline order and phase coherence [105, 106, 107], suggesting superfluid. Leggett argued that the modulated density $\rho(\mathbf{r})$ of a supersolid leads to an unavoidable

reduction in $\rho^{\rm sf}$, and derived an upper bound for $\rho^{\rm sf}$ [101]. This reduction is accompanied by the appearance of an unusual normal fluid that is pinned to the lattice potential and contrary to the usual two-fluid model carries no entropy. Here, the reduced superfluid density results from the 3D density distribution, and as such is masked in tight binding descriptions such as the Bose-Hubbard model, which makes the unrelated prediction of vanishing $\rho^{\rm sf}$ at the superfluid to Mott insulator transition [108, 109].

So an interesting question to ask would be can we see the reduction of $\rho^{\rm sf}$ in a pure BEC by introducing spatial modulated $\rho(r)$? The spatial modulation can be easily provided by the optical lattice in the experiment. If we only apply a 1D lattice, we might be able to observe the anisotropic superfluid density $\rho^{\rm sf}$, which is quite reasonable, since $\rho^{\rm sf}$ should be a tensor defined from the transport response.

In this chapter I will first introduce the Leggett bound and then discuss the superfluid hydrodynamics and finally show the experimental work on this topic: (i) measurement of the superfluid density via speed of sound and compared it to Leggett's bound; (ii) measurement of the rotating response of the system from the scissors mode.

7.2 Leggett's Formula in anisotropic superfluids

Here we consider pure 3D BECs well described by the Gross-Pitaveskii wavefunction $\psi(\mathbf{r}) = |\psi(\mathbf{r})|\exp[i\vartheta(\mathbf{r})]$. An optical lattice potential $V(\mathbf{r}) = (U_0/2)\cos(2k_{\rm r}x)$ periodically modulates the condensate density $\rho(\mathbf{r}) = |\psi(\mathbf{r})|^2$ with unit cell (UC) size $a = \pi/k_{\rm r}$ [Fig. 7.1(b)-*i*]. In contrast, the SF order parameter $\phi(\mathbf{r})$ is a coarse grained quantity describing the properties of the system on a scale $\gg a$, giving the nominally uniform density in Fig. 7.1(c)-*i*.

Even disregarding potential differences between $\rho^{\mathrm{sf}}(\mathbf{r})$ and $\rho(\mathbf{r})$, we argue that $\phi(\mathbf{r})$ is not simply equal to $\psi(\mathbf{r})$ averaged on some large scale compared to a. The fundamental origin of this effect can be understood by considering a 1D system of size L with periodic boundary conditions in which both the condensate phase ϑ and the SF phase φ wind by an integer multiple N of 2π [Fig. 7.1(b,c)-*ii*], yielding a metastable quantized supercurrent [110]. To satisfy the steady-state continuity equation, the microscopic current $J(x) = \rho(x)\,[\hbar\partial_x\vartheta(x)/m]$ must be independent of x [Fig. 7.1(b)-*ii*], however, the periodically modulated density $\rho(x) > 0$ implies that the local velocity $v(x) = \hbar\partial_x\vartheta(x)/m$ has an oscillatory structure and consequently $\vartheta(x)$ follows a staircase pattern [Fig. 7.1(b)-*iii, iv*] with steps of height $2\pi Na/L$.

From macroscopic considerations the superfluid current is $J = \rho^{\mathrm{sf}}\,[\hbar\partial_x\varphi(x)/m] = 2\pi N\hbar\rho^{\mathrm{sf}}/(mL)$. Equating the currents obtained from the condensate wavefunction and the SF order parameter and integrating over a UC [1] yields Leggett's equation [101]

$$\rho^{\mathrm{sf}}(x) = \left[\frac{1}{a}\int_{\mathrm{UC}}\frac{dx'}{\rho(x+x')}\right]^{-1}, \tag{7.1}$$

along with

$$\varphi(x) = \frac{1}{a}\int_{\mathrm{UC}}\vartheta(x+x')dx'.$$

GPE simulations confirm that these analytical relations are valid independent of the lattice period to healing length ratio. Equation (7.1) further implies that $\rho^{\mathrm{sf}} \leq \bar{\rho}$, where $\bar{\rho}$ is the spatial average of the condensate density over a UC, and at zero temperature the remaining density $\rho^{\mathrm{n}} = \bar{\rho} - \rho^{\mathrm{sf}}$

[1] Any average that removes the lattice structure suffices and the average over single UC where x' ranges from 0 to L is the most compact possible.

behaves as a normal fluid pinned to the lattice potential.

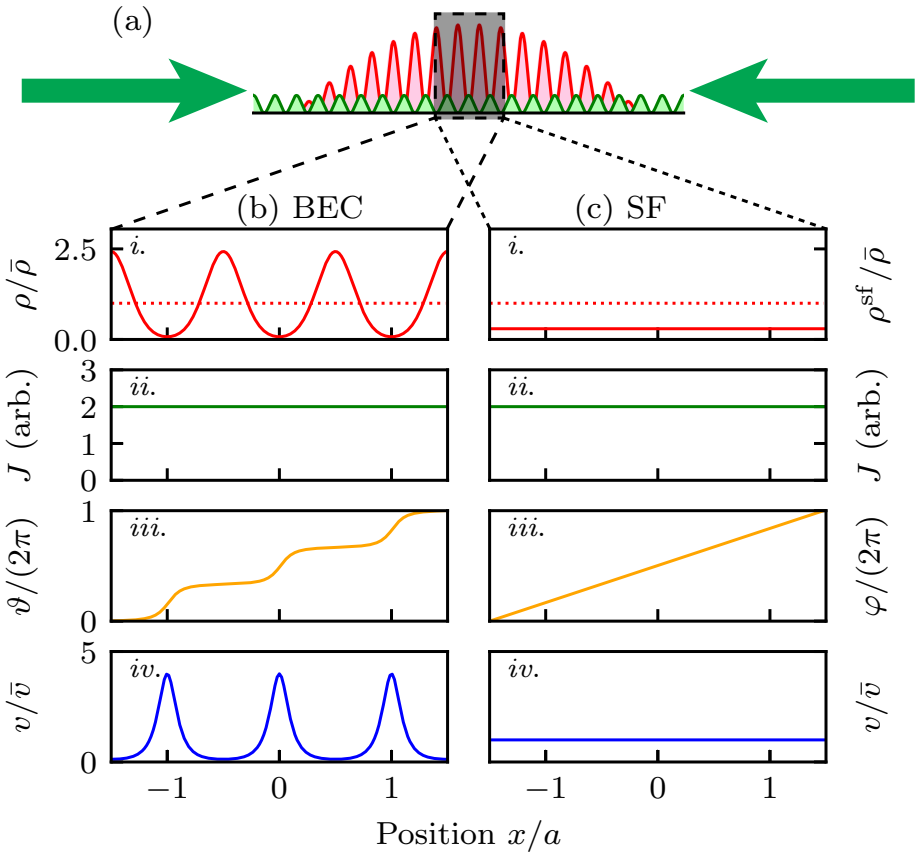

Figure 7.1: Concept. (a) A BEC is confined in a harmonic trap superimposed with a 1D optical lattice (along $\mathbf{e}_x$, green), spatially modulating the condensate density (red). The dashed and dotted lines call out a region of nominally constant mean density and the left and right columns indicate the (b) state of the condensate and (c) SF in the presence of a current. These were computed for a $5E_{\mathrm{r}}$ deep lattice and plot: *i.* density (red), *ii.* current (green), *iii.* phase (orange), and *iv.* local velocity (blue). The red dashed line plots the mean density $\bar{\rho}$.

In a 3D system, the current $J_i = \rho^{\mathrm{sf}}_{ij}\,[\hbar\partial_j\varphi/m]$ is derived from an SF density tensor (having employed the Einstein summation convention). Provided that the condensate phase can be expressed as $\vartheta(\mathbf{r}) = \vartheta_x(x) + \vartheta_y(y) + \vartheta_z(z)$, the argument above in conjunction with 3D continuity equation implies that ρ^{sf}_{ij} is diagonal, and the analogs to Eq. (7.1) for each of the three elements use the 1D density integrated along the transverse directions [2]. In the more general

[2]Time reversal symmetry is also necessary so that each component—such as $\psi_x(x)$—has no nodes and can be made real valued [111].

context where mean field theory [such as the Gross-Pitaveskii equation (GPE)] is inapplicable or the condensate phase cannot be separated as above, the Leggett expression for $\rho^{\rm sf}$ is an upper bound for the SF density [101]; in later work Leggett also found a lower bound [111]. Using the Legget expression, this implies that the superfluid density is only reduced along the direction of the optical lattice, so $\rho^{\rm sf}_{yy} = \rho^{\rm sf}_{zz} = \bar{\rho}$.

7.3 Superfluid Hydrodynamics

In this section, we will first derive the equation of motion from Hamiltonian mechanics. Then we will coarse-grain the external potential and derive a long-wavelength GPE that describes the superfluid dynamics where the Leggett bound is recovered. And finally, we can obtain the dependence of the collective mode on the superfluid density.

7.3.1 Hamiltonian fluid mechanics

We begin by deriving Leggett's bound from the mean-field energy functional and arrive at the superfluid hydrodynamic equations and an effective long-wavelength GPE. We approach this problem using the mean-field energy functional

$$\begin{aligned} E[\psi,\psi^*] &= \int d^3\mathbf{r}\left[-\psi^*\frac{\hbar^2}{2m}\partial_j\partial_j\psi + V(\mathbf{r})|\psi|^2 + \frac{g}{2}|\psi|^4 - \mu|\psi|^2\right] \\ &= \int d^3\mathbf{r}\left[\frac{\hbar^2}{2m}(\partial_j\psi^*)(\partial_j\psi) + V(\mathbf{r})|\psi|^2 + \frac{g}{2}|\psi|^4 - \mu|\psi|^2\right], \end{aligned}$$

which integrates the local energy density $\mathcal{E}$ over all space. V is the external potential and the interaction constant $g = 4\pi\hbar^2 a_s/m$ is proportional to the s-wave scattering length a_s. We

integrated by parts to obtain the second expression with the assumption that the wavefunction is vanishing at the boundary.

GPE: The GPE can be directly obtained by using $E[\psi, \psi^*]$ as a classical Hamiltonian and considering $\psi^*(\mathbf{r})$ and $i\hbar\psi^*(\mathbf{r})$ as fields of canonical positions q and momenta p. Taking the functional derivative of Eq. (7.2) leads to a pair of dynamical equations

$$d_t q = \partial_p E \to d_t \psi = \frac{1}{i\hbar}\left[-\frac{\hbar^2}{2m}\partial_j\partial_j + V(\mathbf{r}) + g|\psi|^2 - \mu\right]\psi. \tag{7.2}$$

$$d_t p = -\partial_q E \to i\hbar d_t \psi^* = -\left[-\frac{\hbar^2}{2m}\partial_j\partial_j + V(\mathbf{r}) + g|\psi|^2 - \mu\right]\psi^*. \tag{7.3}$$

These expressions are a complex conjugate pair, both of which recover the time-dependent GPE.

Phase-amplitude: Dynamics can also be obtained in the phase-amplitude picture

$$\begin{aligned} E &= \int d^3\mathbf{r}\left\{\frac{\hbar^2}{2m}\left|i\partial_j\vartheta + \frac{1}{2\rho}\partial_j\rho\right|^2\rho + \left[\frac{g}{2}\rho + V - \mu\right]\rho\right\} \\ &= \int d^3\mathbf{r}\left\{\left[\frac{\hbar^2}{2m}\left(\partial_j\vartheta\right)^2 + \frac{\hbar^2}{2m}\frac{1}{4\rho^2}\left(\partial_j\rho\right)^2 + \frac{g}{2}\rho + V - \mu\right]\rho\right\}. \end{aligned} \tag{7.4}$$

using $\psi = \rho^{1/2}\exp(i\vartheta)$. Dynamics are again generated as in Hamiltonian mechanics, here by identifying the canonical "momentum" $p \to \hbar\vartheta$ and "position" $q \to \rho$. We therefore have

$$\partial_t\rho(\mathbf{r}) = \frac{\delta E}{\delta(\hbar\vartheta)} = \frac{1}{m}\int d^3\mathbf{r}'\rho\partial_j(\hbar\vartheta)\partial_j\delta(\mathbf{r}-\mathbf{r}') = -\frac{\hbar}{m}\partial_j(\rho\partial_j\vartheta) \tag{7.5}$$

$$\partial_t\hbar\vartheta(\mathbf{r}) = -\frac{\delta E}{\delta(\rho)} = -g\rho - V + \mu - \frac{\hbar^2}{2m}\left[\left(\partial_j\vartheta\right)^2 - \frac{1}{4\rho^2}\left(\partial_j\rho\right)^2 - \partial_j\frac{1}{2\rho}\partial_j\rho\right] \tag{7.6}$$

$$= -g\rho - V + \mu - \frac{\hbar^2}{2m}\left[\left(\partial_j\vartheta\right)^2 - \frac{1}{\rho^{1/2}}\partial_j^2\rho^{1/2}\right] \tag{7.7}$$

where we included $\mathbf{r}$ in places to clarify the action of δ-functions. This recovers the usual superfluid hydrodynamics.

7.3.2 Coarse Graining

We now turn to the case where the potential can be expressed as a sum $V(\mathbf{r}) = V_{\rm s}(\mathbf{r}) + V_{\rm r}(\mathbf{r})$ of slowly and rapidly varying components. In our experiments $V_{\rm r}(\mathbf{r})$ will be a lattice potential and $V_{\rm s}(\mathbf{r})$ will be the external trap. The coarse graining strategy is to find a long wavelength energy density

$$\mathcal{E}_{\rm eff} = \frac{\hbar^2}{2m} f_{ij}^{\rm sf} (\partial_i \xi^*)(\partial_j \xi) + V_{\rm eff}(\mathbf{r})|\xi|^2 + \frac{g_{\rm eff}}{2}|\xi|^4 - \mu_{\rm eff}|\xi|^2 \tag{7.8}$$

equal to the unit-cell averaged energy density

$$\bar{\mathcal{E}} = \frac{1}{L^3}\int_{\rm UC} d^3\mathbf{r} \left[\frac{\hbar^2}{2m}(\partial_i \psi^*)(\partial_i \psi) + V(\mathbf{r})|\psi|^2 + \frac{g}{2}|\psi|^4 - \mu|\psi|^2\right] \tag{7.9}$$

of the full theory in Eq. (7.4). Here $\bar{\rho}$ and φ are the unit-cell averaged density and phase giving the coarse grained GPE wavefunction $\xi = \bar{\rho}\exp(i\varphi)$; and L^3 is the unit cell's volume.

We now proceed term by term in order of increasing complexity, beginning with the chemical potential to illustrate the approach:

$$\mu_{\rm eff}\bar{\rho} = \int_{\rm UC} \frac{d^3\mathbf{r}'}{L^3}\mu\rho(\mathbf{r}') = \mu\bar{\rho}, \qquad \text{so} \qquad \mu_{\rm eff} = \mu. \tag{7.10}$$

Thus, the chemical potential is unchanged. The terms leading to the effective potential

$$V_{\text{eff}}\bar{\rho} = \int_{\text{UC}} \frac{d^3\mathbf{r}'}{L^3}\left[\frac{\hbar^2}{2m}(\partial_i\psi^*)(\partial_i\psi) + V_{\text{r}}(\mathbf{r}')\rho(\mathbf{r}') + V_{\text{s}}(\mathbf{r}')\rho(\mathbf{r}')\right] \tag{7.11}$$

$$\approx \int_{\text{UC}} \frac{d^3\mathbf{r}'}{L^3}\left[\frac{\hbar^2}{2m}(\partial_i\psi^*)(\partial_i\psi) + V_{\text{r}}(\mathbf{r}')\rho(\mathbf{r}')\right] + V_{\text{s}}\bar{\rho} \tag{7.12}$$

include a contribution from the kinetic energy. The resulting effective potential

$$V_{\text{eff}} = \int_{\text{UC}} \frac{d^3\mathbf{r}'}{L^3}\frac{\hbar^2}{2m}\frac{(\partial_i\psi^*)(\partial_i\psi)}{\bar{\rho}} + \int_{\text{UC}} \frac{d^3\mathbf{r}'}{L^3}V_{\text{r}}(\mathbf{r}')\frac{\rho(\mathbf{r}')}{\bar{\rho}} + V_{\text{s}} \tag{7.13}$$

contains the expected contribution from the slowly varying potential, the average of $V_{\text{r}}(\mathbf{r}')$ weighted by the normalized density distribution, and the kinetic energy associated with the rapidly varying wavefunction.

The interaction coefficient is slightly changed according to

$$g_{\text{eff}}\bar{\rho}^2 = g\int_{\text{UC}} \frac{d^3\mathbf{r}'}{L^3}\rho^2(\mathbf{r}'), \qquad \text{so} \qquad g_{\text{eff}} = g\int_{\text{UC}} \frac{d^3\mathbf{r}'}{L^3}\left[\frac{\rho(\mathbf{r}')}{\bar{\rho}}\right]^2. \tag{7.14}$$

This describes the increase in interaction energy resulting from confining atoms into the individual lattice sites.

The kinetic energy term is difficult to work with directly, so we instead focus on the continuity equations, which result from the kinetic energy density. Averaging over a single unit cell leads to an equality

$$\partial_j J_j^{\text{sf}} = \int_{\text{UC}} \frac{d^3\mathbf{r}'}{L^3}\partial_j J_j = \sum_j \frac{J_j^{\perp}(\mathbf{r} + L\mathbf{e}_j) - J_j^{\perp}(\mathbf{r})}{L} \approx \partial_j J_j^{\perp} \tag{7.15}$$

stating that the change in coarse-grained density must be equal in both descriptions. Here we introduce the current $J_j = \hbar\rho\partial_j\vartheta/m$ and its coarse-grained counterpart $J_j^{\rm sf} = \hbar\bar{\rho}f_{jk}^{\rm sf}\partial_k\varphi/m$. In the second equality we evaluated the integral along the j-direction and introduced the transverse averaged currents $J_j^{\perp}$ and density $\rho^{(\perp,j)}$, for example $J_x^{\perp} = \int dydz J_x/L^2$ and $\rho^{(\perp,x)} = \int dydz\rho/L^2$, where the integrals is over a face of the unit cell. In the long-wavelength limit we replace the finite difference with a derivative, leading to the conclusion $J_j^{\rm sf} = J_j^{\perp}$ and therefore

$$\bar{\rho}f_{jk}^{\rm sf}\partial_k\varphi = \int \frac{d^2\mathbf{r}'_{\perp}}{L^2}\rho\partial_j\vartheta = \rho^{(\perp,j)}\partial_j\vartheta_j. \tag{7.16}$$

In the second equality we assumed the mean field wavefunction phase can be written in a separable form, implying $\vartheta = \vartheta_x(x) + \vartheta_y(y) + \vartheta_z(z)$. Since φ is the unit-cell average of ϑ it can be written in the same way. Integrating Eq. (7.16) then leads to

$$f_{jk}^{\rm sf} = \delta_{jk}\left[\frac{1}{L}\int dr_j \frac{\bar{\rho}}{\rho^{(\perp,j)}}\right]^{-1} \tag{7.17}$$

and recovers Leggett's bound as an equality. This completes the job of deriving the coarse-grained GPE

$$i\hbar d_t\xi = \left[-\frac{\hbar^2}{2m}f_{ij}^{\rm sf}\partial_i\partial_j + V_{\rm eff}(\mathbf{r}) + g_{\rm eff}|\xi|^2 - \mu\right]\xi \tag{7.18}$$

An interesting point is that this GPE describes the dynamics of the coarse grained GPE wavefunction ξ not the superfluid order parameter, since $|\xi|^2 = \bar{\rho}$, rather than $\rho_{ij}^{\rm sf}$. However, its phase φ is the phase of the superfluid order parameter and leads to the superfluid density via $\rho_{ij}^{\rm sf} = \bar{\rho}f_{ij}^{\rm sf}$.

7.3.3 Coarse-grained superfluid hydrodynamics

We now continue by obtaining a long-wavelength hydrodynamic description of the coarse-grained GPE in Eq. (7.18). In this case, the number current density and angular momentum density are

$$J_i = \frac{\hbar}{2mi} f_{ij}^{\mathrm{sf}} \left(\xi^* \partial_j \xi - \xi \partial_j \xi^*\right) = \frac{\hbar}{m} \bar{\rho} f_{ij}^{\mathrm{sf}} \partial_j \varphi \quad \text{and} \quad \Pi_z = x J_y - y J_x = \frac{\hbar}{m} \bar{\rho} f_{yy}^{\mathrm{sf}} x \partial_y \varphi - \frac{\hbar}{m} \bar{\rho} f_{xx}^{\mathrm{sf}} y \partial_x \varphi \tag{7.19}$$

respectively In the phase-amplitude picture with $\xi = \sqrt{\bar{\rho}} e^{i\varphi}$, the GPE transforms into the anisotropic hydrodynamic equations

$$\partial_t \bar{\rho} + \frac{\hbar}{m} \partial_i \left(\bar{\rho} f_{ij}^{\mathrm{sf}} \partial_j \varphi\right) = 0 \qquad \text{and} \qquad -\hbar \partial_t \varphi = \frac{\hbar^2}{2m} f_{ij}^{\mathrm{sf}} \partial_i \varphi \partial_j \varphi + g_{\mathrm{eff}} \bar{\rho} + V_{\mathrm{eff}} - \mu. \tag{7.20}$$

In what follows, we focus on the case of a lattice aligned along $\mathbf{e}_x$ or $\mathbf{e}_y$, making $f_{\mathrm{ij}}^{\mathrm{sf}}$ diagonal.

7.3.3.1 Collective modes

Now we can find the collective modes by making small perturbations about the equilibrium state,

$$\bar{\rho} \to \bar{\rho} + \delta\bar{\rho}$$

$$\varphi \to \varphi + \delta\varphi$$

$$V_{\mathrm{eff}} \to V_{\mathrm{eff}} + \delta V$$

$$\begin{cases} \partial_t \delta\bar{\rho} + \frac{\hbar}{m} f_{ij}^{\rm sf} \left[\partial_i \delta\bar{\rho} \partial_j \varphi + \partial_i \bar{\rho} \partial_j \delta\varphi + \delta\bar{\rho} \partial_i \partial_j \varphi + \bar{\rho} \partial_i \partial_j \delta\varphi\right] = 0 \\ -\hbar \partial_t \delta\varphi = \frac{\hbar^2}{2m} f_{ij}^{\rm sf} \left[\partial_i \varphi \partial_j \delta\varphi + \partial_i \delta\varphi \partial_j \varphi\right] + \delta V + g_{\rm eff} \delta\bar{\rho} \end{cases}$$

Because of the initial state satisfies $\varphi = 0$ and $g\bar{\rho} = \mu - \frac{1}{2} m\omega_i^2 x_i^2$,

$$\begin{cases} \partial_t \delta\bar{\rho} + \frac{\hbar}{m} f_{ij}^{\rm sf} \left[\partial_i \bar{\rho} \partial_j \delta\varphi + \bar{\rho} \partial_i \partial_j \delta\varphi\right] = 0 \\ -\hbar \partial_t \delta\varphi = \delta V + g_{\rm eff} \delta\bar{\rho} \end{cases}$$

We take

$$\delta\varphi = \delta\varphi_x x + \delta\varphi_y y$$

to derive the dipole oscillation frequencies. Let $\delta V = 0$, $\delta\bar{\rho} \to \delta\bar{\rho} e^{-i\omega t}$ and $\delta\varphi \to \delta\varphi e^{-i\omega t}$, and collect coefficients before both linear terms x and y, one calculates the eigenmodes of

$$\begin{pmatrix} \omega^2 - f_{xx}^{\rm sf} \omega_x^2 & 0 \\ 0 & \omega^2 - f_{yy}^{\rm sf} \omega_y^2 \end{pmatrix}$$

The dipole mode frequencies are decoupled and are given by $\omega_{j,d}^2 = f_{jj}^{\rm sf} \omega_j^2$.

The scissors mode is one of the quadratic modes, and we suppose

$$\delta\varphi = \delta\varphi_{xx} x^2 + \delta\varphi_{yy} y^2 + \delta\varphi_{xy} xy$$

and collect coefficients of all three quadratic terms giving the matrix

$$\begin{pmatrix} \omega^2 - 3\omega_x^2 f_{xx}^{\rm sf} & -\omega_x^2 f_{yy}^{\rm sf} & -2\omega_x^2 f_{xy}^{\rm sf} \\ -f_{xx}^{\rm sf}\omega_y^2 & \omega^2 - 3\omega_y^2 f_{yy}^{\rm sf} & -2\omega_y^2 f_{xy}^{\rm sf} \\ -2\omega_y^2 f_{xy}^{\rm sf} & -2\omega_x^2 f_{xy}^{\rm sf} & \omega^2 - \left(f_{xx}^{\rm sf}\omega_x^2 + f_{yy}^{\rm sf}\omega_y^2\right) \end{pmatrix}.$$

When $f_{xy}^{\rm sf} = 0$, $f_{xx}^{\rm sf} \neq f_{yy}^{\rm sf}$ this reduces to

$$\begin{pmatrix} \omega^2 - 3f_{xx}^{\rm sf}\omega_x^2 & -f_{yy}^{\rm sf}\omega_x^2 & 0 \\ -f_{xx}^{\rm sf}\omega_y^2 & \omega^2 - 3f_{yy}^{\rm sf}\omega_y^2 & 0 \\ 0 & 0 & \omega^2 - f_{xx}^{\rm sf}\omega_x^2 - f_{yy}^{\rm sf}\omega_y^2 \end{pmatrix}.$$

The scissors mode frequency obeys $\omega_{sc}^2 = f_{xx}^{\rm sf}\omega_x^2 + f_{yy}^{\rm sf}\omega_y^2$, while the quadruple mode frequencies are

$$\omega_{\rm quad}^2 = \frac{3\bar{\omega}^2 \pm \sqrt{9\bar{\omega}^4 - 32 f_{xx}^{\rm sf} f_{yy}^{\rm sf}\omega_x^2\omega_y^2}}{2}$$

with $\bar{\omega} = \omega_{sc}$.

It can be easily seen from the matrix that the scissor mode decouples from the other two quadrupole modes. This generalizes to 3D, where there are three decoupled scissors modes xy, yz, zx. Thus, although our system is actually 3D, the xy scissors mode frequency is given by the 2D result derived here. This procedure easily generalizes to $f_{xy}^{\rm sf} \neq 0$.

7.3.3.2 Rotational properties of the scissors mode

Following the above section

$$\Pi_z = xJ_y - yJ_x = \frac{\hbar}{m}\bar{\rho}f_{yy}^{\mathrm{sf}}x\partial_y\varphi - \frac{\hbar}{m}\bar{\rho}f_{xx}^{\mathrm{sf}}y\partial_x\varphi, \tag{7.21}$$

and plug in the second hydrodynamics equation

$$\partial_t\Pi_z = x\partial_t J_y - y\partial_t J_x = -x\partial_j T_{jy} + y\partial_j T_{jx} - x\bar{\rho}\partial_y(f_{yy}^{\mathrm{sf}}\frac{V_{\mathrm{eff}}}{m}) + y\bar{\rho}\partial_x(f_{xx}^{\mathrm{sf}}\frac{V_{\mathrm{eff}}}{m}). \tag{7.22}$$

where we define $T_{jk} \equiv \bar{\rho}v_j v_k - \sigma_{jk}$ and $\sigma_{jk} \equiv -\frac{1}{2}f_{jk}^{\mathrm{sf}}g_{\mathrm{eff}}\frac{\bar{\rho}^2}{m} + (\frac{\hbar}{2m})^2\bar{\rho}f_{jl}^{\mathrm{sf}}f_{kn}^{\mathrm{sf}}\partial_l(\frac{\partial_n\bar{\rho}}{\bar{\rho}})$. Those are the counterparts of the classical momentum flux and stress tensor. More generally, this equation actually follows from

$$\partial_t J_k = -\partial_j T_{jk} - \frac{\bar{\rho}}{m}f_{jk}^{\mathrm{sf}}\partial_j V_{\mathrm{eff}}. \tag{7.23}$$

Equation (7.23) provides the important dynamic equation for the quantum anisotropic superfluid, in analogy to the classical Navier–Stokes equation. (It can be derived from the GPE without any approximation. We omit the derivation here to avoid distraction.)

Integrating over all space generates the torque

$$\tau = \int dxdy(f_{xx}^{\mathrm{sf}}\omega_x^2 - f_{yy}^{\mathrm{sf}}\omega_y^2)\bar{\rho}xy = (f_{xx}^{\mathrm{sf}}\omega_x^2 - f_{yy}^{\mathrm{sf}}\omega_y^2)\langle xy\rangle$$

where the stress tensor terms in the equation (7.22) vanish after integration by parts:

$$\int d^3r\epsilon^{ik}r_i\partial_j T_{jk} = \int d^3r\partial_j\left(\epsilon^{ik}r_i T_{jk}\right) - \int d^3r\epsilon^{ik}T_{jk}\partial_j r_i = 0$$

because T_{jk} is symmetric tensor.

A cloud rotated by a small angle θ experiences a torque

$$\tau = (f^{\rm sf}_{xx}\omega_x^2 - f^{\rm sf}_{yy}\omega_y^2)\langle x'^2 - y'^2\rangle\theta \tag{7.24}$$

where $\langle x'^2 - y'^2\rangle = \int d^3\mathbf{r}'\rho(x'^2 - y'^2)$ depends only on the initial Thomas-Fermi distribution. This leads to an equation describing harmonic motion

$$\tau = \partial_t L_z \equiv I\ddot{\theta}$$

where I is the moment of inertia; I can be obtained from

$$\frac{I}{I_c} = \frac{-\tau/\theta}{I_c\omega_{sc}^2} = -\frac{(f^{\rm sf}_{xx}\omega_x^2 - f^{\rm sf}_{yy}\omega_y^2)\langle x^2 - y^2\rangle}{\langle x^2 + y^2\rangle\,\omega_{sc}^2}$$

in terms of the oscillation frequency ω_{sc} and the classical moment of inertia $I_c = \langle x^2 + y^2\rangle$.

In the ground state of the harmonically trapped condensate which has a Thomas-Fermi density distribution, we have

$$\frac{\langle x^2\rangle}{\langle y^2\rangle} = \frac{\omega_y^2}{\omega_x^2}$$

where ω_x and ω_y are the trap frequencies along e_x and e_y directions. Hence the moment of inertia

is

$$\frac{I}{I_c} = \frac{(f_{xx}^{\mathrm{sf}}\omega_x^2 - f_{yy}^{\mathrm{sf}}\omega_y^2)(\omega_x^2 - \omega_y^2)}{(\omega_x^2 + \omega_y^2)\,\omega_{sc}^2}.$$

7.3.3.3 Moment of inertia

The moment of inertia can also be derived from its definition

$$I = \lim_{\Omega \to 0} \frac{\partial \langle L_z \rangle}{\partial \Omega}.$$

We calculate this derivative respectively in the cases of (i) static lattice and (ii) rotating lattice.

The main difference between case (i) and (ii) is the order of two operations: the projection into the lowest band of the lattice and rotating frame transformation that makes the trap potential time invariant. In a rotating trap but static lattice, we first project the dynamics to the lowest band, and then the time dependent potential can be transformed away and one derives additional terms with the angular frequency Ω,

$$\begin{cases} \partial_i \left(\frac{\hbar}{m} \bar{\rho} f_{ij}^{\mathrm{sf}} \partial_j \varphi \right) - \nabla \cdot (\bar{\rho} \vec{\Omega} \times \vec{r}) = 0 \\ \frac{\hbar^2}{2m^2} f_{ij}^{\mathrm{sf}} \partial_i \varphi \partial_j \varphi + \frac{V_{\mathrm{eff}}}{m} + \frac{g_{\mathrm{eff}} \bar{\rho}}{m} - \frac{\hbar}{m} \nabla \varphi \cdot (\vec{\Omega} \times \vec{r}) = \frac{\mu}{m} \end{cases} \tag{7.25}$$

Here we use the ansatz $\varphi = \frac{m}{\hbar} \alpha x y$. Since the μ in the second equation is spatial independent, and under the $\Omega \to 0$ limit, we obtain

$$\frac{y \partial_x \bar{\rho}}{x \partial_y \bar{\rho}} = \frac{\omega_x^2}{\omega_y^2},$$

where the terms of α and Ω are neglected. The first equation gives

$$\frac{y\partial_x\bar{\rho}}{x\partial_y\bar{\rho}} = \frac{\Omega - f_{yy}^{\mathrm{sf}}\alpha}{\Omega + f_{xx}^{\mathrm{sf}}\alpha}.$$

Therefore we obtain

$$\alpha = -\Omega\frac{\omega_x^2 - \omega_y^2}{f_{xx}^{\mathrm{sf}}\omega_x^2 + f_{yy}^{\mathrm{sf}}\omega_y^2}, \tag{7.26}$$

and the total angular momentum becomes

$$\langle L_z\rangle = \left\langle \vec{r}\times\vec{J}\right\rangle = \alpha\left\langle f_{yy}^{\mathrm{sf}}x^2 - f_{xx}^{\mathrm{sf}}y^2\right\rangle = \frac{\omega_x^2 - \omega_y^2}{f_{xx}^{\mathrm{sf}}\omega_x^2 + f_{yy}^{\mathrm{sf}}\omega_y^2}\left\langle f_{xx}^{\mathrm{sf}}y^2 - f_{yy}^{\mathrm{sf}}x^2\right\rangle\Omega$$

$$\frac{I}{I_c} = \frac{1}{I_c}\frac{\partial\langle L_z\rangle}{\partial\Omega} = \frac{\omega_x^2 - \omega_y^2}{\omega_x^2 + \omega_y^2}\frac{f_{xx}^{\mathrm{sf}}\omega_x^2 - f_{yy}^{\mathrm{sf}}\omega_y^2}{f_{xx}^{\mathrm{sf}}\omega_x^2 + f_{yy}^{\mathrm{sf}}\omega_y^2} \tag{7.27}$$

where I_c is moment of inertia a classical mass distribution $I_c = \langle x^2 + y^2\rangle$. One can verify that the scissors mode frequency is given by

$$\omega_{sc} = \sqrt{\frac{-\tau}{I\theta}} = \sqrt{f_{xx}^{\mathrm{sf}}\omega_x^2 + f_{yy}^{\mathrm{sf}}\omega_y^2} \tag{7.28}$$

the same as derived from the collective mode section.

The most striking observation from the result is that the moment of inertia can go negative when the superfluid density along one axis is suppressed below a critical value determined by the trap frequencies. This behavior is purely quantum mechanical and has no counterpart in classical physics as we know of. From a hydrodynamics view, the reason for this zero-crossing is that the angular momentum density always has co-rotating and counter-rotating parts in a quantum gas,

due to the irrotational nature of the order parameter. Without the lattice, however, the co-rotating part always exceeds the counter-rotating part, thus leading to positive moment of inertia. But with the anisotropic lattice present the relative contribution of them can be re-tuned by varying the lattice depth.

Next we consider the case (ii) with a rotating lattice synchronized with the rotating harmonic trap. In this case, the projection operation into the lowest band needs to be taken after the rotating frame transformation. The equation (7.25) then needs to modified as

$$\begin{cases} \partial_i \left(\frac{\hbar}{m} \bar{\rho} f_{ij}^{\mathrm{sf}} \partial_j \varphi \right) - \nabla \cdot (\bar{\rho} \vec{\tilde{\Omega}} \times \vec{r}) = 0 \\ \frac{\hbar^2}{2m^2} f_{ij}^{\mathrm{sf}} \partial_i \varphi \partial_j \varphi + \frac{V_{\mathrm{eff}}}{m} + \frac{g_{\mathrm{eff}} \bar{\rho}}{m} - \frac{\hbar}{m} \nabla \varphi \cdot (\vec{\tilde{\Omega}} \times \vec{r}) = \frac{\mu}{m} \end{cases} \tag{7.29}$$

where the $\tilde{\Omega}$ is selected to be $\tilde{\Omega} = \Omega(f_{xx}^{\mathrm{sf}}, f_{yy}^{\mathrm{sf}})$. This can be seen from the fact that the kinetic energy part is modified by the superfluid fraction tensor, so is the current operator. One arrives at similar to the equation (7.26)

$$\alpha = -\Omega \frac{f_{xx}^{\mathrm{sf}} \omega_x^2 - f_{yy}^{\mathrm{sf}} \omega_y^2}{f_{xx}^{\mathrm{sf}} \omega_x^2 + f_{yy}^{\mathrm{sf}} \omega_y^2} \tag{7.30}$$

and

$$\frac{I^{sf}}{I_c} = \frac{(f_{xx}^{\mathrm{sf}} \omega_x^2 - f_{yy}^{\mathrm{sf}} \omega_y^2)^2}{(f_{xx}^{\mathrm{sf}} \omega_x^2 + f_{yy}^{\mathrm{sf}} \omega_y^2)(\omega_x^2 + \omega_y^2)} \tag{7.31}$$

This is the superfluid contribution to the moment of inertia, because only the superfluid flow can be derived from the coarse-graining process that assumes lowest band dynamics. Equation (7.31) aligns very well with the simulation result which is calculated from the gradients of the coarse-grained superfluid phase $\vartheta(\mathbf{r})$, confirming the self-consistent superfluid description. Note that it is strictly positive and rather different from the equation (7.27), due to the different order of

rotating frame transformation and coarse graining.

However, the rest part of the moment of inertia is contributed by the normal fluid indeed. The normal fluid current can be written as

$$J^n = (-\rho^n_{xx} y, \rho^n_{yy} x)\Omega \tag{7.32}$$

which can be derived from the transverse current definition

$$I = \lim_{\mathbf{q}\to 0} \sum_{n\neq 0} \frac{|\langle 0|\hat{L}_z e^{i\mathbf{q}\cdot\mathbf{r}}|n\rangle|^2 + |\langle 0|\hat{L}_z e^{-i\mathbf{q}\cdot\mathbf{r}}|n\rangle|^2}{E_n - E_0}, \tag{7.33}$$

and it gives rise to

$$\frac{I^n}{I_c} = \frac{f^{\mathrm{n}}_{xx}\omega_x^2 + f^{\mathrm{n}}_{yy}\omega_y^2}{\omega_x^2 + \omega_y^2} \tag{7.34}$$

This result is also checked with the simulation by calculating the subtraction of the superfluid from the total moment of inertia.

7.3.3.4 GPE simulations of rotating systems

We performed 2D GPE simulations of rotating harmonically trapped systems where : (i) the lattice co-rotates with the confining potential or (ii) it is static in the lab frame (as in scissors mode experiments). In both cases we use the coarse graining defined in section IA to obtain the superfluid density and phase. In this way we compute the total moment of inertia I from $\psi(\mathbf{r}, t)$, the superfluid component I^{sf} from $\phi(\mathbf{r}, t)$, and we define the normal component as the difference $I^{\mathrm{n}} = I - I^{\mathrm{sf}}$.

Case (i): the angular momentum density is strictly positive [Fig. 7.2(b)] for both lattice

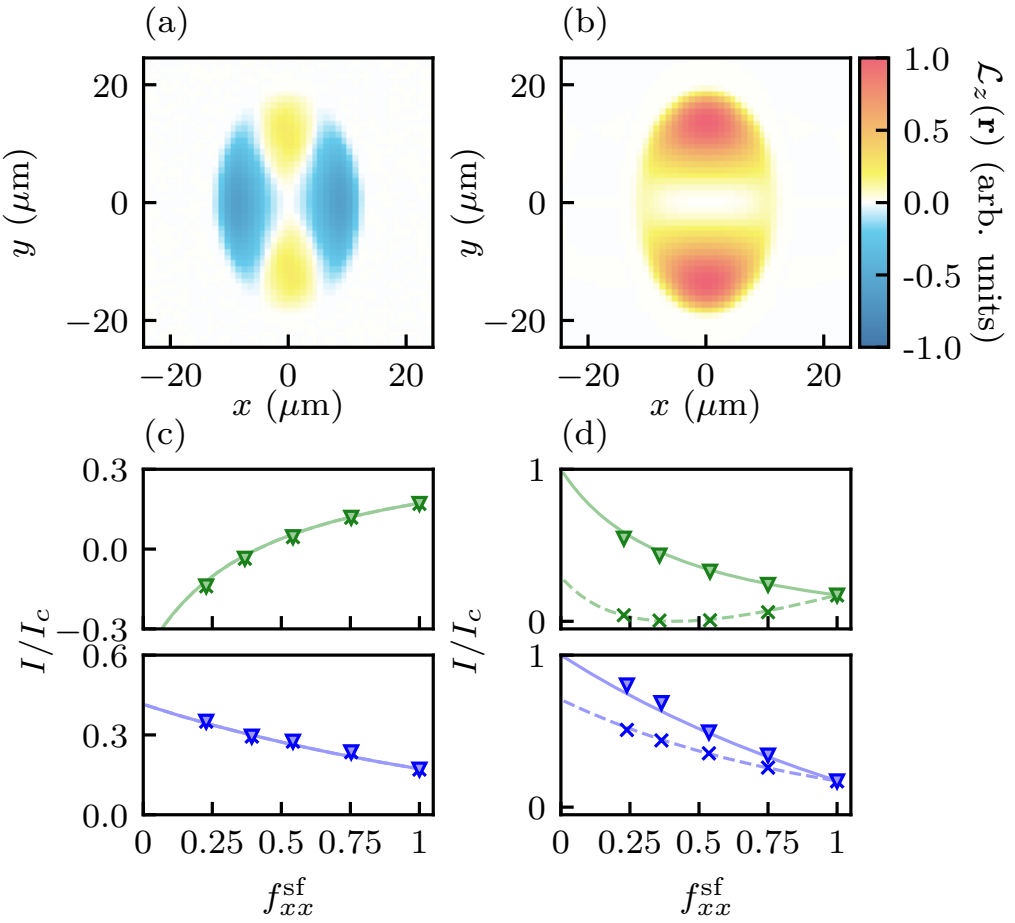

Figure 7.2: Moment of inertia in rotating systems computed using 2D GPE simulations. The left column (a, c) indicates simulations in which the lattice is static while in the right column (b, d) the lattice co-rotates with the confining potential. (a, b) Angular momentum density for trap frequencies $2\pi\times$(56,36) and $U_0 = 10E_{\mathrm{r}}$. The colormap ranges from negative to positive, by normalizing to the largest absolute angular momentum density. (c, d) Total momentum of inertia in traps with frequencies $2\pi\times$(56,36) (top, green) and $2\pi \times (36, 56)$ Hz (bottom, blue). In (c) and (d), the cross markers are GPE simulated results of superfluid contribution to the moment of inertia I^{sf}/I_c. This is identified by calculating the gradient of phase coarse-grained across a unit cell. The triangle makers are GPE simulated results of the total moment of inertia I/I_c including the normal and superfluid contributions. Dashed curves plot I^{sf}/I_c and the solid curve plots I/I_c both analytically derived from the superfluid hydrodynamics formalism.

orientations and I/I_c increases with lattice depth [Fig. 7.2(d)]. In this case the normal fluid co-rotates with the trap giving the current $J^n = (-\rho^{\rm n}_{xx} y, \rho^{\rm n}_{yy} x)\dot{\theta}$. The total I/I_c is then the sum of the superfluid and normal contribution

$$\frac{I}{I_c} = \frac{(f^{\rm sf}_{xx}\omega_x^2 - f^{\rm sf}_{yy}\omega_y^2)^2}{(f^{\rm sf}_{xx}\omega_x^2 + f^{\rm sf}_{yy}\omega_y^2)(\omega_x^2+\omega_y^2)} + \frac{f^{\rm n}_{xx}\omega_x^2 + f^{\rm n}_{yy}\omega_y^2}{\omega_x^2+\omega_y^2}. \tag{7.35}$$

This result, along with our 2D GPE simulations, is plotted in Fig. 7.2(d). The dashed curve plots the superfluid contribution to $I^{\rm sf}/I_c$ in agreement with the coarse-grained GPE (crosses). The solid curve and the triangles plot the corresponding total moment of inertia, in excess of the SF contribution. This implies the appearance of normal fluid flow.

This agreement confirms that the superfluid contribution derives from gradients of the coarse-grained phase φ, while the normal contribution stems from variations of ϑ within each lattice site.

Case (ii): in contrast, as in our 1D thought experiment only the SF component responds. Then although $\nabla\varphi$ is manifestly irrotational, because $\rho^{\rm sf}_{xx} \neq \rho^{\rm sf}_{yy}$ the superfluid current can be rotational. In this case, the relative magnitude of the co- and counter-rotating contributions vary with the lattice depth, leading to regions of negative angular momentum density $\mathcal{L}(\mathbf{r})$ along the BEC's semi-minor axis [Fig. 7.2(a)]. The superfluid moment of inertia computed from these simulations [Fig. 7.2(c)] is in full agreement with the scissor mode simulation, and as expected for a static lattice $I^{\rm sf} = I$ (no normal flow).

When the lattice is along the semi-minor axis, as pictured in (a) and the green curve in (c), the counter-rotating contribution increases with U_0, until the dipole mode frequencies along $\mathbf{e}_x$ and $\mathbf{e}_y$ invert, after which point, $I/I_{\rm c}$ becomes negative. The reverse is the case when the lattice

is along the semi-major axis and I/I_c increases monotonically.

The superfluid current can be decomposed into $\mathbf{J} = \mathbf{J}_+ + \mathbf{J}_-$, a sum of irrotational ($\mathbf{J}_+$) and rotational ($\mathbf{J}_-$) components with

$$\mathbf{J}_\pm = \frac{\hbar\bar{\rho}}{m}\frac{f_{xx}^{\mathrm{sf}} \pm f_{yy}^{\mathrm{sf}}}{2}\left(\mathbf{e}_x\partial_x \pm \mathbf{e}_y\partial_y\right)\varphi.$$

In conventional isotropic SFs the rotational term $\mathbf{J}_- = 0$, implying irrotational current flow and non-negative I/I_c. For anisotropic superfluids, $\mathbf{J}_-$ need not be zero, and introduces an anomalous contribution $\propto (f_{xx}^{\mathrm{sf}} - f_{yy}^{\mathrm{sf}})(\omega_x^2 - \omega_y^2)$ to I/I_c that can be positive or negative. This decomposition is not unique since one can introduce irrotational terms $\pm\mathbf{J}'_+$ to $\mathbf{J}_\pm$ that sum to zero in $\mathbf{J}$. We selected the natural convention for which $\mathbf{J}_-$ is zero for isotropic SFs.

7.4 Superfluid sum-rule and sound velocity

In this section we will first show the superfluid density is related to the speed of sound from the Josephson sum-rule. Then we follow the route of the coarse-grained hydrodynamics to see that the speed of sound is dependent on the superfluid density tensor.

7.4.1 Josephson sum-rule

The superfluid density is explicitly related to Green function of the many-body Hamiltonian via the Josephson sum-rule [112]. Here we derive the sum-rule and relate it to the anisotropic sound velocities. We consider the variation of the condensate wavefunction $\psi(x) = |\psi|\exp[i\phi(\mathbf{r})]$ from a perturbation Hamiltonian $H' = -\int d\mathbf{r}\psi(\mathbf{r})\zeta(\mathbf{r})$, where $\zeta(\mathbf{r}) = \zeta\exp[i(\mathbf{k}\cdot\mathbf{r} - \omega t)]$.

According to linear response theory

$$\delta\langle\psi(\mathbf{r})\rangle = \zeta e^{i\mathbf{k}\cdot\mathbf{r}} \int_{-\infty}^{\infty} d\omega' \frac{\mathbf{A}(\mathbf{k},\omega')}{\omega + i\eta - \omega'}, \tag{7.36}$$

where $A(\boldsymbol{k},\omega) = \int d\mathbf{r} e^{-i\boldsymbol{k}\cdot(\boldsymbol{r}-\boldsymbol{r}')} \int_{-\infty}^{\infty} dt e^{i\omega(t-t')} \left\langle \left[\psi(\boldsymbol{r},t), \psi^{\dagger}(\boldsymbol{r}',t')\right]\right\rangle$ is the spectral density, and is related to the retarded one-body Green function

$$A(\mathbf{k},\omega) = i\hbar \int d(\mathbf{r}-\mathbf{r}') e^{-i\mathbf{k}(\mathbf{r}-\mathbf{r}')} \int_{-\infty}^{\infty} d(t-t') e^{i\omega(t-t')} G^{\mathrm{ret}}(\mathbf{r},t;\mathbf{r}',t').$$

Similarly, the variation of the current operator $\mathbf{J}(\mathbf{r}) = \rho\mathbf{v}$ is

$$\delta\langle\mathbf{J}(r)\rangle = e^{i\mathbf{k}\cdot\mathbf{r}-i\omega t}\zeta \int d\omega' \frac{\mathbf{\Gamma}(\mathbf{k},\omega')}{\omega + i\eta - \omega'} \tag{7.37}$$

with $\Gamma(k,\omega) = \int d\mathbf{r}dt e^{-i\omega(t-t')+ik(r-r')} \langle \left[J(r,t), \psi^{\dagger}(r',t')\right]\rangle$. In the next we first take $\omega \to 0$ limit, and then take $\mathbf{k} \to 0$.

We want to relate $\delta\langle\mathbf{J}(\mathbf{r})\rangle$ to $\delta\langle\psi(\mathbf{r})\rangle$, as to define the superfluid density. To do that, one observes from the continuity equation $-i\mathbf{k}\cdot\mathbf{J} = \partial_t\rho$ so that

$$\mathbf{J}(\mathbf{r},t) = \int d\mathbf{k}\mathbf{J}(\mathbf{k},t)e^{ik\cdot r} = \int d\mathbf{k}d\mathbf{r}' e^{ik(r-r')} \frac{i\vec{k}}{k^2} \partial_t\rho(r',t).$$

Plug it back to equation 7.37, and after some algebra

$$\begin{aligned}\Gamma(\mathbf{k},\omega) &= \int d\mathbf{r}dt e^{-i\omega(t-t')+ik(r-r')} \int d\mathbf{k}'d\mathbf{r}'' e^{ik'(r-r'')} \frac{i\vec{k'}(-i\omega)}{k'^2} \langle \left[\rho(r'',t), \psi^{\dagger}(r',t')\right]\rangle \\ &= \int dt e^{-i\omega(t-t')} \int d\mathbf{r}'' e^{ik(r''-r')} \frac{\mathbf{k}\omega}{k^2} \langle \left[\rho(r''t), \psi^{\dagger}(r't')\right]\rangle\end{aligned} \tag{7.38}$$

Hence

$$\begin{aligned}
\delta\langle \mathbf{J}(\mathbf{r},t)\rangle &= \int d\omega' \frac{\mathbf{\Gamma}\left(k,\omega'\right)}{-\omega'} e^{i\mathbf{k}r}\zeta \\
&= -\int d\omega e^{i\mathbf{k}r}\zeta \int dt e^{-i\omega(t-t')} \int d\mathbf{r} e^{ik\cdot(r-r')} \frac{\vec{k}}{k^2} \langle \left[\rho(r,t), \psi^\dagger\left(r',t'\right)\right]\rangle \\
&= -e^{i\mathbf{k}r}\zeta \int d\mathbf{r} e^{i\mathbf{k}\cdot(r-r')} \frac{\vec{k}}{k^2} \left\langle \left[\rho(rt), \psi^\dagger\left(r't\right)\right]\right\rangle \\
&= -e^{ik\cdot r}\zeta \frac{k}{k^2} \left\langle \psi^\dagger(r,t)\right\rangle
\end{aligned} \tag{7.39}$$

In the last equality we used $\left[\rho(r), \psi^\dagger\left(r'\right)\right] = \left[\psi^\dagger(r)\psi(r), \psi^\dagger\left(r'\right)\right] = \psi^\dagger(r)\delta\left(r-r'\right)$.

For a superfluid system, $\langle\psi(\mathbf{r})\rangle = \psi_0 + \delta\langle\psi(\mathbf{r})\rangle = e^{i\theta(\mathbf{r})}\psi_0$ where we have defined the superfluid phase $\theta(\mathbf{r})$. With the periodic modulation of density introduced by the optical lattice, we take $\psi(\mathbf{r}) \to \bar{\psi}(\mathbf{r}) = a_x a_y a_z \int_{\mathrm{UC}} d\mathbf{r}'\psi(\mathbf{r}')$.[113] Now we have

$$\begin{aligned}
\delta\langle\bar{\mathbf{J}}\rangle &= -e^{i\mathbf{k}\cdot r}\zeta \frac{\mathbf{k}}{k^2}\left\langle\bar{\psi}^\dagger\right\rangle \\
\delta\langle\bar{\psi}\rangle &= -e^{i\mathbf{k}\cdot r}\zeta \int d\omega \frac{A(k,\omega)}{\omega} \\
\frac{m}{\hbar}\delta\langle\bar{\mathbf{J}}\rangle &= \rho^{sf}\nabla\theta = \rho^{sf}\nabla\frac{\delta\langle\bar{\psi}\rangle}{i\bar{\psi}_0} = \rho^{sf}_{\hat{k}}\mathbf{k}\frac{\delta\langle\bar{\psi}\rangle}{\bar{\psi}_0}
\end{aligned}$$

and take $\mathbf{k}\to 0$

$$\rho^{sf}_{\hat{k}} = m\lim_{\mathbf{k}\to 0}\frac{\bar{\psi}_0^*\bar{\psi}_0}{k^2\int_{-\infty}^{+\infty}d\omega\frac{\mathbf{A}(k,\omega)}{\omega}} \tag{7.40}$$

where $\rho^{sf}_{\hat{k}} = \rho^{sf}_{ij}\hat{\mathbf{k}}_j$. For a homogeneous weakly interacting Bose gas at $T=0$, the Bogoliubov theory gives $\mathbf{A}(\mathbf{k},\omega) = \frac{mc}{2k}[\delta(\omega-ck)-\delta(\omega+ck)]$ as $k\to 0$, which leads to $\rho^{sf}_{\hat{k}} = |\psi_0|^2$. For anisotropic systems, the poles of $\mathbf{A}(\mathbf{k},\omega)$ i.e. the sound velocities along different directions will determine the anisotropic superfluid density.

The modification of the phonon spectrum by the presence of a shallow optical lattice is

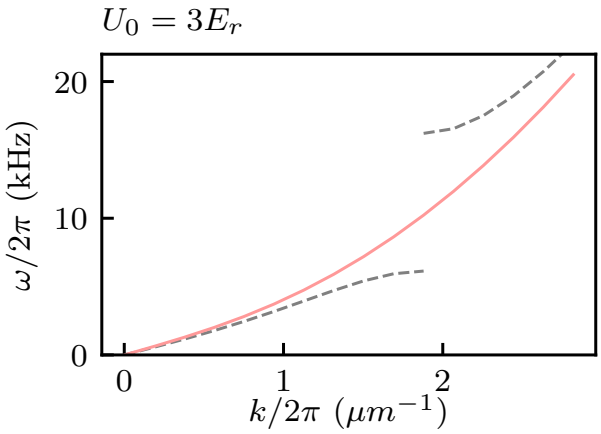

Figure 7.3: Modification of the phonon spectrum by the $a = 266$ nm optical lattice via BdG calculation. $U_0 = 3E_r$. Dashed black and solid red curves mark excitations created along $\mathbf{e}_x$ and $\mathbf{e}_y$ respectively.

numerically computed through the Bogoliubov-de-Gennes equations applied upon the mean-field ground state found by a 2D GPE imaginary time simulation. The lattice changes the sound velocity ratio while opening a gap at the Brillouin zone edge, as in Fig. 7.3.

7.4.2 Speed of sound from the superfluid hydrodynamics

In an isotropic system, the speed of sound C can be expressed as

$$C = \sqrt{\frac{\partial P}{\partial \rho}}, \tag{7.41}$$

where P is the pressure and ρ is the density. In case of anisotropic superfluid, the stress tensor can be deduced from the coarse-grained hydrodynamics, i.e.,

$$\sigma_{jk} \equiv -\frac{1}{2} f^{\mathrm{sf}}_{jk} g_{\mathrm{eff}} \frac{\bar{\rho}^2}{m} + (\frac{\hbar}{2m})^2 \bar{\rho} f^{\mathrm{sf}}_{jl} f^{\mathrm{sf}}_{kn} \partial_l (\frac{\partial_n \bar{\rho}}{\bar{\rho}}), \tag{7.42}$$

where the second term is the quantum pressure, and for the case of phonon it is negligible due to long-wavelength limit. So, the speed of sound is determined by the first term, where the anisotropic pressure becomes $P_{jk} = \frac{1}{2} f_{jk}^{\mathrm{sf}} g_{\mathrm{eff}} \frac{\bar{\rho}^2}{m}$. Then under the principal axis system, where P_{jk} is diagonal, we have

$$C_j = \sqrt{\frac{\partial P_{jj}}{\partial \bar{\rho}}} = \sqrt{f_{jj} g_{\mathrm{eff}} \frac{\bar{\rho}}{m}}. \tag{7.43}$$

Then in our 1D lattice case, the direction without density modulation should have pure superfluid fraction, and the superfluid density drop in the direction with density modulation is proportional to the reduction of the square of the speed of sound, i.e.,

$$\left(\frac{C_j}{C_0}\right)^2 = f_{jj}, \quad C_0 = \sqrt{g_{\mathrm{eff}} \frac{\bar{\rho}}{m}}. \tag{7.44}$$

7.5 Experiments

7.5.1 Bragg Spectroscopy

We used $^{87}\mathrm{Rb}$ BECs with $N \approx 2 \times 10^5$ atoms in the $|F = 1, m_F = 1\rangle$ hyperfine ground state. A $1064\ \mathrm{nm}$ trapping laser with an elliptical cross section traveling along $\mathbf{e}_x$ provided strong vertical confinement with frequency $\omega_z/(2\pi) = 220\ \mathrm{Hz}$; the in-plane frequencies, from $\omega_{x,y}/(2\pi) = (34, 51)\ \mathrm{Hz}$ to $(56, 36)\ \mathrm{Hz}$, were optimized for our different experiments. We created a 1D optical lattice using a retro-reflected $\lambda = 532\ \mathrm{nm}$ laser traveling along $\mathbf{e}_x$, giving an $a = 266\ \mathrm{nm}$ lattice period, comparable to the $\xi = 170(20)\ \mathrm{nm}$ minimum healing length. The optical lattice was linearly ramped on in $100\ \mathrm{ms}$ to a final depth $\leq 10\ E_{\mathrm{r}}$, with single

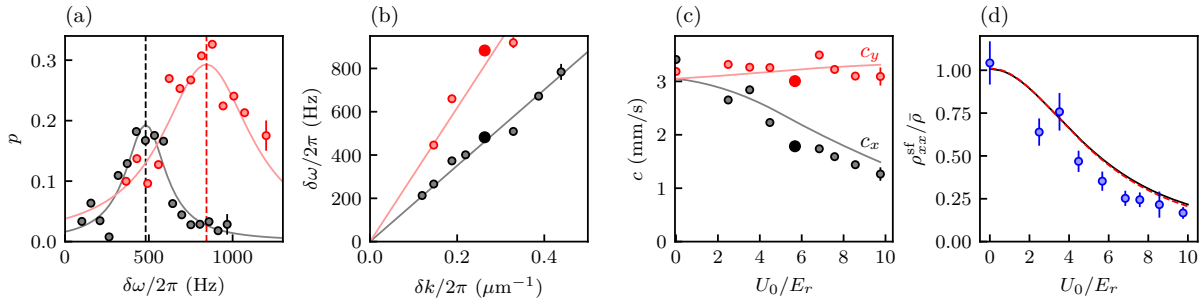

Figure 7.4: Bragg spectroscopy. Black and red symbols mark excitations created along $\mathbf{e}_x$ and $\mathbf{e}_y$ respectively. (a) Transferred population fraction p as a function of frequency difference $\delta\omega$ with wavevetor $\delta k/2\pi = 0.26\ \mu\mathrm{m}^{-1}$ and lattice depth $U_0 = 5.7E_\mathrm{r}$. The solid curve is a Lorentzian fit, giving the resonance frequency marked by the vertical dashed line. (b) Phonon dispersion obtained from Bragg spectra. The bold symbols resulted from (a) and the linear fit (with zero intercept) gives the speed of sound. (c) Anisotropic speed of sound. The bold symbols are derived from (b) and the solid curves are from BdG simulations (no free parameters [3]). (d) SF density obtained from speed of sound measurements (blue markers, error bars mark single-sigma statistical uncertainties). We compare with two models: the red dashed curve plots a homogeneous gas BdG calculation, and the solid black curve plots the result of Eq. (7.1). The simulations used our calibrated experimental parameters. In (a)-(c) each point has uncertainty as shown in the last point.

photon recoil energy and momentum $E_\mathrm{r} = \hbar^2 k_\mathrm{r}^2/(2m)$, and $\hbar k_\mathrm{r} = 2\pi\hbar/\lambda$ respectively [3]. For Bragg experiments the final state was measured using resonant absorption imaging after a 15 ms time of flight (TOF); scissors mode measurements were performed in-situ using partial transfer absorption imaging [115].

The speed of sound for diagonal $\rho^{\rm sf}_{ij}$ obeys the hydrodynamic relation [84] $c_i^2 = f^{\rm sf}_{ii}/(\kappa m)$ in terms of the compressibility $\kappa = \bar{\rho}^{-1}\,(\partial\bar{\rho}/\partial\mu)$, the chemical potential μ, and with density reduced by the superfluid fractions $f^{\rm sf}_{ij} = \rho^{\rm sf}_{ij}/\bar{\rho}$. This reduces to the well-known value $c^2 = \mu/m$ for an isotropic homogeneous system (See [3] for the full dispersion beyond the linear approximation).

[3] We calibrated the lattice depth U_0 by suddenly applying the lattice potential and fitting the resulting Kaptiza-Dirac scattering [114].

The sound speed ratio

$$\frac{c_x^2}{c_y^2} = \frac{\rho_{xx}^{\rm sf}}{\rho_{yy}^{\rm sf}} = f_{xx}^{\rm sf}, \tag{7.45}$$

provides direct access to the different components of the superfluid density [see [3] for a Josephson sum rule argument]. Because the density is y-independent, Eq. (7.1) implies $\rho_{yy}^{\rm sf} = \bar{\rho}$.

We performed Bragg scattering using a weak sinusoidal potential with reciprocal lattice vector δk slowly moving with velocity v by patterning a laser beam with a digital micro-mirror device (DMD [79]) and measured the scattered fraction p. This results from what are effectively two interfering laser beams driving two-photon transitions with difference-wavevector δk and angular frequency $\delta\omega = \delta k\ v$. We applied this potential for ≈ 5 ms. Bragg transitions ensued when the difference energy and momentum were resonant with the BEC's Bogoliubov dispersion, and Fig. 7.4(a) shows data in the linear regime. The width of this spectral feature is limited by our BEC's inhomogeneous density profile; the resonance (vertical dashed line) obtained from a Lorentzian fit (solid curve) therefore reflects an average speed of sound [4]. The reduced Bragg signal at small $\delta\omega$ results from the vanishing of the static structure factor in the phonon spectrum as $\delta\omega$ goes to zero [116].

A series of such fits lead to phonon dispersion relations with Bragg-lattice period from $2.25\ \mu$m to $8.5\ \mu$m. Representative dispersions taken along $\mathbf{e}_x$ and $\mathbf{e}_y$ are shown in Fig. 7.4(b), and we obtain the phonon speed of sound using linear fits. Figure 7.4(c) summarizes these data showing the speed of sound decreasing along the lattice direction $\mathbf{e}_x$, but slightly increasing

[4] In high-elongated quasi-1D BECs, the longitudinal speed of sound is reduced by a factor of $\sqrt{2}$ from $\sqrt{\mu/m}$. We expect a related reduction from our tight confinement along $\mathbf{e}_z$, but for the Bragg spectra to exhibit inhomogeneous broadening from the nearly isotropic Thomas-Fermi profile in the $\mathbf{e}_x$-$\mathbf{e}_y$ plane.

along $\mathbf{e}_y$ (resulting from the increased atomic density in the individual lattice sites). Finally Fig. 7.4(d) shows our main result: the normalized superfluid density obtained from these data using Eq. (7.45) decreases as a function of U_0.

We compared these data to GPE simulations in two ways, we: (1) used the Bogoliubov-de Gennes (BdG) equations [84] to obtain c_x and c_y and (2) directly evaluated Eq. (7.1) from the GPE ground state density. The solid curves in Fig. 7.4(c) plot the sound speed obtained from solving the 1D BdG [5], and the red dashed curve in (d) is the ratio of these speeds. To compare with Leggett's prediction, we found the ground state of the 2D GPE for our experimental parameters and evaluated Eq. (7.1) throughout our inhomogeneous system. The black curve in (d) plots the resulting weighted average. Remarkably the BdG results are in near-perfect agreement with Leggett's expression.

7.5.2 Scissors mode

The direct connection between the SF phase gradient and the velocity field greatly impacts rotational properties such as the moment of inertia I. For a highly anisotropic harmonic trap, the scissors mode [117, 118] describes a fixed density distribution pivoting by a small angle θ about an axis traversing trap center with frequency ω_{sc}. Scissors mode experiments are in spirit reminiscent of, though different in detail from, torsional balance experiments in $^4\mathrm{He}$, which give access to the non-classical rotational inertia [102, 103].

[5] To make k a good quantum number we modeled untrapped systems with periodic boundary conditions. The chemical potential was selected to give the observed $3\ \mathrm{mm/s}$ speed of sound without the lattice present.

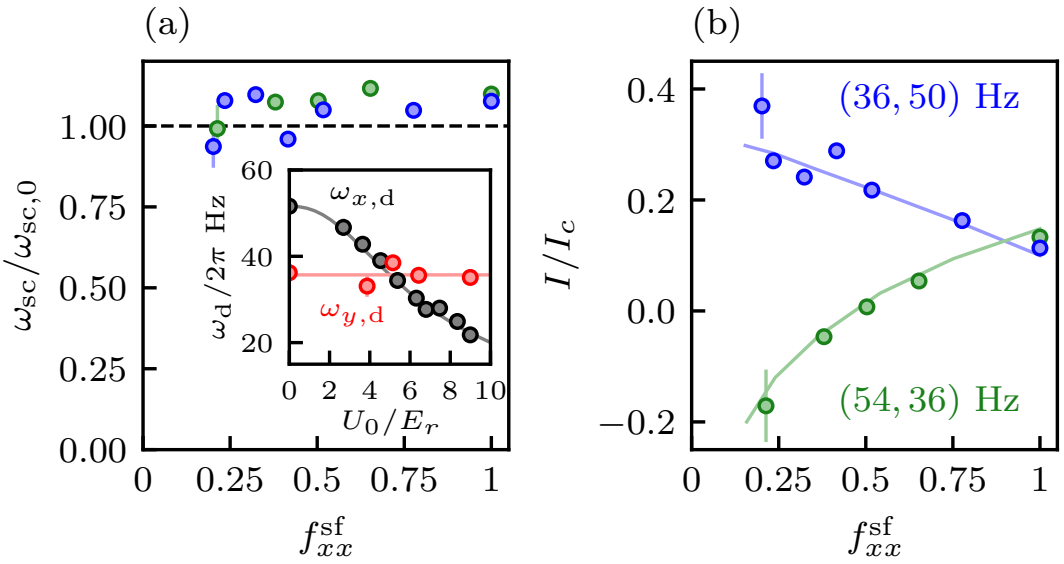

Figure 7.5: Moment of inertia from scissors mode. (a-inset) Measured dipole mode frequencies (circles) along with fits (curves) where the bare trap frequency is the only free parameter for each curve. (a) Normalized scissors mode frequency. Blue and green correspond to $U_0 = 0$ trap frequencies $(34, 51)$ Hz and $(54, 36)$ Hz respectively. (b) Moment of inertia in units of I_c. In (a) and (b) each point has uncertainty as shown on the first point. Symbols are the data computed as described in the text, and the solid curves are GPE predictions.

We describe the scissors mode in terms of the angular momentum density

$$\Pi_z = m(xJ_y - yJ_x) = \hbar\bar{\rho}\left(xf_{yy}^{\rm sf}\partial_y\varphi - yf_{xx}^{\rm sf}\partial_x\varphi\right) \tag{7.46}$$

of the initial density distribution $\bar{\rho}(\mathbf{r})$ oscillating by a small angle $\theta(t)$. Integrating Π_z over the system yields the total angular momentum L_z, then taking the derivative with respect to time gives the torque

$$\tau = \int d^3\mathbf{r}\partial_t\Pi_z = -g\int d^3\mathbf{r}\bar{\rho}\left[xf_{yy}^{\rm sf}\partial_y\delta\rho - yf_{xx}^{\rm sf}\partial_x\delta\rho\right],$$

where g is the GPE interaction strength, and we used the linearized long-wavelength hydrodynamic kinetic equation $0 = \hbar\partial_t\varphi + g\delta\rho$ to describe small changes in the density $\delta\rho$. Assuming an initial

Thomas-Fermi distribution for $\bar{\rho}$, the small-θ density difference $\delta\rho \approx -m\theta\left(\omega_x^2 - \omega_y^2\right) xy/g$ gives the torque

$$\tau = \frac{m\theta}{N}\left(\omega_x^2 - \omega_y^2\right)\left(\langle x^2\rangle f_{yy}^{\mathrm{sf}} - \langle y^2\rangle f_{xx}^{\mathrm{sf}}\right). \tag{7.47}$$

In this case, the equation of motion $\tau = I\ddot{\theta}$ describes the scissors mode oscillations and thus connects the scissors mode frequency ω_{sc} to the moment of inertia

$$\frac{I}{I_c} = \frac{\left(\omega_x^2 - \omega_y^2\right)\left(\omega_x^2 f_{xx}^{\mathrm{sf}} - \omega_y^2 f_{yy}^{\mathrm{sf}}\right)}{\omega_{\mathrm{sc}}^2(\omega_x^2 + \omega_y^2)} \tag{7.48}$$

in terms of the classical moment of inertia I_{c}. This expression is in agreement with Ref. [117] when $f_{xx}^{\mathrm{sf}} = f_{yy}^{\mathrm{sf}} = 1$. Therefore, we expect ω_{sc}, in conjunction with the superfluid density will give I/I_c as a function of lattice depth.

The inset to Fig. 7.5(a) plots the observed dipole mode frequencies $\omega_{x,\mathrm{d}}$ and $\omega_{y,\mathrm{d}}$ for a trap with bare (i.e., $U_0 = 0$) frequencies $(\omega_x, \omega_y) = (54, 36)$ Hz. The dipole frequency $\omega_{x,\mathrm{d}}$ decreases with increasing U_0; similarly to the sound speed, this is related to ρ^{sf} via $f^{\mathrm{sf}} = (\omega_{x,\mathrm{d}}/\omega_x)^2$ along the lattice direction. This ratio can also be expressed in terms of an increased effective mass m^*, with $f^{\mathrm{sf}} = m/m^*$ [119]; this converges to the predictions of the single-particle band structure [120] when the lattice period falls below the healing length; in our case the value computed perturbatively from the GPE differs by about $20\ \%$ from the band structure prediction. The result of this modeling is shown by the solid curves.

We excited the scissors mode using our DMD to tilt the harmonic potential by 50 to 140 mrad for ≈ 1 ms (shorter than the trap periods) and let the BEC evolve in the original trap for

a variable time. We measured the resulting dynamics in-situ and extracted the angle by fitting the resulting density profile to a rotated Gaussian. Figure 7.5(a) shows the scissors mode frequency normalized to the expected frequency [38] of $\omega_{\mathrm{sc},0}^2 = f_{xx}^{\mathrm{sf}}\omega_x^2 + f_{yy}^{\mathrm{sf}}\omega_y^2$ for a trap elongated either along $\mathbf{e}_x$ [with frequencies $(56, 36)$ Hz, blue] or along $\mathbf{e}_y$ [with frequencies $(36, 50)$ Hz, green]. In both cases ω_{sc} appears to be about $5\ \%$ in excess of the simple prediction, perhaps from finite temperature or anharmonicities in the optical dipole trap.

We combine these observations in Fig. 7.5(b) to obtain I/I_{c}; the data (symbols) and our 2D GPE simulations (curves, with moment of inertia computed using $I = \lim_{\Omega\to 0} \partial_\Omega L_z$, with angular frequency $\Omega = \dot{\theta}$) are in agreement [6]. For traps elongated along $\mathbf{e}_x$ (green), I/I_c surprisingly changes sign when $\omega_{x,\mathrm{d}} = \omega_{y,\mathrm{d}}$. To understand the physical origin of this effect, we now turn our attention to rotating systems.

7.5.3 Rotation

Our discussion so far has focused on the superfluid density and avoided questions about any associated normal fluid flow. We can deduce the existence of a normal fluid component by considering two thought experiments each a 1D ring geometry (with radius R) and in each case consider the resulting angular momentum. In case (i), we consider a lattice along the azimuthal direction that is very slowly accelerated [121] to a final angular velocity Ω; this is best understood by transforming into the frame co-rotating with the lattice. This leads to a lab frame angular momentum $L_z/\hbar = 2\pi R(\bar{\rho} - \rho^{\mathrm{sf}})$ that we interpret as a result of the normal fluid co-moving with the lattice. In case (ii), we consider a complementary configuration with a static lattice and slowly insert a single quantum of "synthetic" magnetic flux (see Ref. [122] for a proposal using artificial

[6] Numerically we selected Ω to be small enough that I did not depend on further changes in Ω.

gauge fields to provide "synthetic" magnetic flux). The process is equivalent to imprinting a 2π phase winding (of the type discussed on page 1), giving angular velocity $\Omega = \hbar/(mR^2)$ and angular momentum $L_z/\hbar = 2\pi R\rho^{\rm sf}$.

We confirm this picture of the existence of a normal fluid using 2D numerical simulations of rotating trapped systems with a 1D lattice where: (i) the lattice co-rotates with the confining potential; or (ii) it is static in the lab frame (as in scissors mode experiments). In (i), the current results from a sum of normal and superfluid flow. The former co-rotates with the lattice and the trap, while the latter derives from the SF phase gradient. In (ii) there is no normal fluid flow, but as with our scissors mode observations, I/I_c changes sign.

Chapter 8: Conclusion and Outlook

8.1 Conclusion

In this dissertation, I investigate superfluid properties of atomic Bose-Einstein condensates (BECs) including laminar flow experiments that probe the superfluid density and turbulent flow experiments that explore connections to Kolmogorov theory .

Laminar flow properties such as the superfluid denisty can be measured via indirect probes, such as the speed of sound measurement in Chap. 7. On the other hand, the irregular flow pattern such as turbulent flow necessitates direct measurement of the velocity field. To this end, I developed a velocimetry method, similar to particle image velocimetry using spinor impurities as tracers to measure the velocity field in a spatially resolved way, discussed in Chap. 5. This enables the first observation of velocity structure functions (VSFs) in BECs, turbulent or otherwise. The observed VSFs reveal that superfluid turbulence in BECs conforms to Kolmogorov theory, including the so-called intermittency evident in both higher-order VSFs and the distribution of velocity increments, discussed in Chap. 6.

8.2 Outlook

Looking ahead, the Kolmogorov scaling law stands as the primary benchmark for understanding any form of turbulence, and this research has indeed found indications of Kolmogorov scaling within atomic Bose-Einstein condensates (BECs).

While Kolmogorov's theory traditionally deals with turbulence that's uniform and the same in all directions (homogeneous and isotropic), real-world turbulence often doesn't follow these simple conditions—it can vary in density and direction (be inhomogeneous and anisotropic). A promising direction for future work would be to apply the velocity structure function (VSF) measurement technique used here to systems like BECs in harmonic traps or other environments.

On the technical side, analyzing scaling laws poses a challenge, especially when the entire system we're studying spans just on the order of $10\,\mu\mathrm{m}$. Expanding the size of the BEC by a factor of 10 could significantly enhance our ability to study turbulence in these systems.

Exploring turbulence involving more than one type of spinor species opens another intriguing avenue of research, particularly phenomena like Rayleigh-Taylor and Kelvin-Helmholtz turbulence [123]. Despite their theoretical significance, these types of instabilities haven't yet been explored experimentally within the atomic BEC field.

The technique I've developed for measuring the velocity field offers a powerful tool for investigating various flows within atomic BECs. Observing the superflow around an airfoil would be fascinating [124]. Moreover, analyzing how tracers diffuses in BECs could provide a novel way to measure temperature field within the system, adding another layer of understanding to our studies of atomic BECs.

Appendix A: List of Publications

A.1 List of Peer-Reviewed Publications

1. Tao, Junheng, **Mingshu Zhao**, and I. B. Spielman. ”Observation of anisotropic superfluid density in an artificial crystal.” *Physical Review Letters* 131, no. 16 (2023): 163401.

2. **Zhao, M.**, A. Restelli, J. Tao, Q. Liang, and I. B. Spielman. ”A 20 A bipolar current source with 140 μA noise over 100 kHz bandwidth.” *AIP Advances* 13, no. 6 (2023).

3. Liang, Q-Y., Dimitris Trypogeorgos, Ana Valdés-Curiel, Junheng Tao, **Mingshu Zhao**, and Ian B. Spielman. ”Coherence and decoherence in the Harper-Hofstadter model.” *Physical Review Research* 3, no. 2 (2021): 023058.

4. Anderson, R. P., D. Trypogeorgos, A. Valdés-Curiel, Q-Y. Liang, J. Tao, **M. Zhao**, Tomas Andrijauskas, Gediminas Juzeliūnas, and I. B. Spielman. ”Realization of a deeply subwavelength adiabatic optical lattice.” *Physical review research* 2, no. 1 (2020): 013149.

A.2 Manuscripts in Preparation

1. **Mingshu Zhao**, Tao, Junheng, and I. B. Spielman. ”Velocity structure function of a turbulent Bose-Einstein condensate.” (2024)

2. Tao, Junheng, E. M. Gutierrez, **Mingshu Zhao**, and I. B. Spielman. "Imaginary gauge potentials in a non-Hermitian spin-orbit coupled quantum gas." (2024)

Bibliography

[1] Francisco Salces Cárcoba. *Microscopy of elongated superfluids*. PhD thesis, University of Maryland, College Park, 2020.

[2] Duncan Cramer. *Fundamental statistics for social research: step-by-step calculations and computer techniques using SPSS for Windows*. Routledge, 2003.

[3] See online SM, which includes Refs. [112, 113, 125].

[4] Ann E Gargett. Ocean turbulence. *Annual Review of Fluid Mechanics*, 21(1):419–451, 1989.

[5] John C Wyngaard. Atmospheric turbulence. *Annual Review of Fluid Mechanics*, 24(1):205–234, 1992.

[6] Ye Zhou, WH Matthaeus, and P Dmitruk. Colloquium: Magnetohydrodynamic turbulence and time scales in astrophysical and space plasmas. *Reviews of Modern Physics*, 76(4):1015, 2004.

[7] Nuno F Loureiro and Stanislav Boldyrev. Role of magnetic reconnection in magnetohydrodynamic turbulence. *Physical Review Letters*, 118(24):245101, 2017.

[8] Sergei F Shandarin and Ya B Zeldovich. The large-scale structure of the universe: Turbulence, intermittency, structures in a self-gravitating medium. *Reviews of Modern Physics*, 61(2):185, 1989.

[9] George Greenstein. Superfluid turbulence in neutron stars. *Nature*, 227(5260):791–794, 1970.

[10] WF Vinen and JJ Niemela. Quantum turbulence. *Journal of low temperature physics*, 128:167–231, 2002.

[11] Emanuel Alves Lima Henn, Jorge Amin Seman, Giacomo Roati, Kilvia Mayre Farias Magalhaes, and Vanderlei Salvador Bagnato. Emergence of turbulence in an oscillating bose-einstein condensate. *Physical review letters*, 103(4):045301, 2009.

[12] Nir Navon, Alexander L Gaunt, Robert P Smith, and Zoran Hadzibabic. Emergence of a turbulent cascade in a quantum gas. *Nature*, 539(7627):72–75, 2016.

[13] Katepalli R Sreenivasan. Fluid turbulence. *Reviews of Modern Physics*, 71(2):S383, 1999.

[14] Lucas Madeira, Mônica Andrioli Caracanhas, FEA dos Santos, and Vanderlei Salvador Bagnato. Quantum turbulence in quantum gases. *Annual Review of Condensed Matter Physics*, 11:37–56, 2020.

[15] Geoffrey Ingram Taylor. The spectrum of turbulence. *Proceedings of the Royal Society of London. Series A-Mathematical and Physical Sciences*, 164(919):476–490, 1938.

[16] Ronald J Adrian and Chung-Sheng Yao. Pulsed laser technique application to liquid and gaseous flows and the scattering power of seed materials. *Applied optics*, 24(1):44–52, 1985.

[17] KJ Thompson, GG Bagnato, Gustavo Deczka Telles, Mônica Andrioli Caracanhas, FEA Dos Santos, and Vanderlei Salvador Bagnato. Evidence of power law behavior in the momentum distribution of a turbulent trapped bose–einstein condensate. *Laser Physics Letters*, 11(1):015501, 2013.

[18] Andrei Nikolaevich Kolmogorov. The local structure of turbulence in incompressible viscous fluid for very large reynolds numbers. *Proceedings of the Royal Society of London. Series A: Mathematical and Physical Sciences*, 434(1890):9–13, 1991.

[19] Andrej Nikolaevich Kolmogorov. On degeneration (decay) of isotropic turbulence in an incompressible viscous liquid. In *Dokl. Akad. Nauk SSSR*, volume 31, pages 538–540, 1941.

[20] Andrei Nikolaevich Kolmogorov. Dissipation of energy in the locally isotropic turbulence. *Proceedings of the Royal Society of London. Series A: Mathematical and Physical Sciences*, 434(1890):15–17, 1991.

[21] Caroline Nore, Malek Abid, and ME Brachet. Kolmogorov turbulence in low-temperature superflows. *Physical review letters*, 78(20):3896, 1997.

[22] Steven R Stalp, L Skrbek, and Russell J Donnelly. Decay of grid turbulence in a finite channel. *Physical review letters*, 82(24):4831, 1999.

[23] Andrey Nikolaevich Kolmogorov. A refinement of previous hypotheses concerning the local structure of turbulence in a viscous incompressible fluid at high reynolds number. *Journal of Fluid Mechanics*, 13(1):82–85, 1962.

[24] Isidor Isaac Rabi. Space quantization in a gyrating magnetic field. *Physical Review*, 51(8):652, 1937.

[25] Anatole Abragam. *The principles of nuclear magnetism*. Number 32. Oxford university press, 1961.

[26] Christopher J Foot. *Atomic physics*, volume 7. OUP Oxford, 2004.

[27] Daniel A Steck. Quantum and atom optics. 2007.

[28] Daniel A Steck. Rubidium 87 d line data. 2001.

[29] Harold J Metcalf and Peter Van der Straten. *Laser cooling and trapping*. Springer Science & Business Media, 1999.

[30] Steven Chu, Leo Hollberg, John E Bjorkholm, Alex Cable, and Arthur Ashkin. Three-dimensional viscous confinement and cooling of atoms by resonance radiation pressure. *Physical review letters*, 55(1):48, 1985.

[31] Eric L Raab, Mara Prentiss, Alex Cable, Steven Chu, and David E Pritchard. Trapping of neutral sodium atoms with radiation pressure. *Physical review letters*, 59(23):2631, 1987.

[32] Paul D Lett, Richard N Watts, Christoph I Westbrook, William D Phillips, Phillip L Gould, and Harold J Metcalf. Observation of atoms laser cooled below the doppler limit. *Physical review letters*, 61(2):169, 1988.

[33] Jean Dalibard and Claude Cohen-Tannoudji. Laser cooling below the doppler limit by polarization gradients: simple theoretical models. *JOSA B*, 6(11):2023–2045, 1989.

[34] Wolfgang Ketterle and NJ Van Druten. Evaporative cooling of trapped atoms. In *Advances in atomic, molecular, and optical physics*, volume 37, pages 181–236. Elsevier, 1996.

[35] Eugene P Gross. Structure of a quantized vortex in boson systems. *Il Nuovo Cimento (1955-1965)*, 20(3):454–477, 1961.

[36] Lev P Pitaevskii. Vortex lines in an imperfect bose gas. *Sov. Phys. JETP*, 13(2):451–454, 1961.

[37] N Bogoliubov. On the theory of superfluidity. *J. Phys*, 11(1):23, 1947.

[38] Lev Pitaevskii and Sandro Stringari. *Bose-Einstein condensation and superfluidity*, volume 164. Oxford University Press, 2016.

[39] Nikolay N Bogoljubov, Vladimir Veniaminovic Tolmachov, and DV Širkov. A new method in the theory of superconductivity. *Fortschritte der physik*, 6(11-12):605–682, 1958.

[40] Osborne Reynolds. Xxix. an experimental investigation of the circumstances which determine whether the motion of water shall be direct or sinuous, and of the law of resistance in parallel channels. *Philosophical Transactions of the Royal society of London*, (174):935–982, 1883.

[41] Claude-Louis Navier. Navier stokes equation. *Paris: Chez Carilian-Goeury*, 1838.

[42] Adolph Fick. V. on liquid diffusion. *The London, Edinburgh, and Dublin Philosophical Magazine and Journal of Science*, 10(63):30–39, 1855.

[43] Lewis Fry Richardson. Atmospheric diffusion shown on a distance-neighbour graph. *Proceedings of the Royal Society of London. Series A, Containing Papers of a Mathematical and Physical Character*, 110(756):709–737, 1926.

[44] Osborne Reynolds. Iv. on the dynamical theory of incompressible viscous fluids and the determination of the criterion. *Philosophical transactions of the royal society of london.(a.)*, (186):123–164, 1895.

[45] Maurizio Carbone and Andrew D Bragg. Is vortex stretching the main cause of the turbulent energy cascade? *Journal of Fluid Mechanics*, 883:R2, 2020.

[46] Andreĭ Monin. *Statistical fluid mechanics, volume II: mechanics of turbulence*.

[47] Hussein Aluie. Scale decomposition in compressible turbulence. *Physica D: Nonlinear Phenomena*, 247(1):54–65, 2013.

[48] A Favre. The equations of compressible turbulent gases. *Annual Summary Report AD0622097*, 1965.

[49] Hussein Aluie. Compressible turbulence: the cascade and its locality. *Physical review letters*, 106(17):174502, 2011.

[50] Jianchun Wang, Yipeng Shi, Lian-Ping Wang, Zuoli Xiao, XT He, and Shiyi Chen. Scaling and statistics in three-dimensional compressible turbulence. *Physical review letters*, 108(21):214505, 2012.

[51] Pyotr Kapitza. Viscosity of liquid helium below the λ-point. *Nature*, 141(3558):74–74, 1938.

[52] John F Allen and AD Misener. Flow of liquid helium ii. *Nature*, 141(3558):75–75, 1938.

[53] Mike H Anderson, Jason R Ensher, Michael R Matthews, Carl E Wieman, and Eric A Cornell. Observation of bose-einstein condensation in a dilute atomic vapor. *science*, 269(5221):198–201, 1995.

[54] KW Schwarz. Three-dimensional vortex dynamics in superfluid he 4: Line-line and line-boundary interactions. *Physical Review B*, 31(9):5782, 1985.

[55] Tomohiro Tanogami. Theoretical analysis of quantum turbulence using the onsager ideal turbulence theory. *Physical Review E*, 103(2):023106, 2021.

[56] WF Vinen, Makoto Tsubota, and Akira Mitani. Kelvin-wave cascade on a vortex in superfluid h e 4 at a very low temperature. *Physical review letters*, 91(13):135301, 2003.

[57] J Maurer and P Tabeling. Local investigation of superfluid turbulence. *Europhysics Letters*, 43(1):29, 1998.

[58] Russell J Donnelly. An introduction to experiments on superfluid turbulence. In *Quantized vortex dynamics and superfluid turbulence*, pages 17–35. Springer, 2001.

[59] Henry Edgar Hall and William Frank Vinen. The rotation of liquid helium ii i. experiments on the propagation of second sound in uniformly rotating helium ii. *Proceedings of the Royal Society of London. Series A. Mathematical and Physical Sciences*, 238(1213):204–214, 1956.

[60] Gregory P Bewley, Daniel P Lathrop, and Katepalli R Sreenivasan. Visualization of quantized vortices. *Nature*, 441(7093):588–588, 2006.

[61] Matthew S Paoletti, Michael E Fisher, Katepalli R Sreenivasan, and Daniel P Lathrop. Velocity statistics distinguish quantum turbulence from classical turbulence. *Physical review letters*, 101(15):154501, 2008.

[62] Enrico Fonda, David P Meichle, Nicholas T Ouellette, Sahand Hormoz, and Daniel P Lathrop. Direct observation of kelvin waves excited by quantized vortex reconnection. *Proceedings of the National Academy of Sciences*, 111(supplement_1):4707–4710, 2014.

[63] Genevieve Comte-Bellot. Hot-wire anemometry. *Annual review of fluid mechanics*, 8(1):209–231, 1976.

[64] William K George and John L Lumley. The laser-doppler velocimeter and its application to the measurement of turbulence. *Journal of Fluid Mechanics*, 60(2):321–362, 1973.

[65] Ronald J Adrian and Jerry Westerweel. *Particle image velocimetry*. Number 30. Cambridge university press, 2011.

[66] Marek Kowalczyk. Laser speckle velocimetry. *Optical Velocimetry*, 2729:139–145, 1996.

[67] MH Fizeau. Sur les hypothèses relatives à l'éther lumineux, et sur une expérience qui parait démontrer que le mouvement des corps change la vitesse avec laquelle la lumière se propage dans leur intérieur. *SPIE milestone series*, 28:445–449, 1991.

[68] Augustin Jean Fresnel. Sur l'influence du mouvement terrestre dans quelques phenomenes d'optique: lettre de m. fresnel a m. arago. *Ann. Chim. Phys.*, 9:57–66, 1818.

[69] Iacopo Carusotto, Maurizio Artoni, Giuseppe Carlo La Rocca, and Franco Bassani. Transverse fresnel-fizeau drag effects in strongly dispersive media. *Physical Review A*, 68(6):063819, 2003.

[70] Zilong Chen, Hong Ming Lim, Chang Huang, Rainer Dumke, and Shau-Yu Lan. Quantum-enhanced velocimetry with doppler-broadened atomic vapor. *Physical Review Letters*, 124(9):093202, 2020.

[71] DR Meacher, Denis Boiron, Harold Metcalf, Christophe Salomon, and Gilbert Grynberg. Method for velocimetry of cold atoms. *Physical Review A*, 50(3):R1992, 1994.

[72] M Zhao, A Restelli, J Tao, Q Liang, and IB Spielman. A 20 a bipolar current source with 140 μa noise over 100 khz bandwidth. *AIP Advances*, 13(6), 2023.

[73] Ben Duncan. *High Performance Audio Power Amplifiers*. Elsevier, 1996.

[74] Paul Horowitz and Winfield Hill. *The art of electronics*. Cambridge university press Cambridge, 2002.

[75] Markus Greiner, Immanuel Bloch, Theodor W Hänsch, and Tilman Esslinger. Magnetic transport of trapped cold atoms over a large distance. *Physical Review A*, 63(3):031401, 2001.

[76] M-LOOP Documentation. M-loop documentation. `https://m-loop.readthedocs.io/en/latest/`, 2024. Accessed: [insert date here].

[77] Dana Dudley, Walter M Duncan, and John Slaughter. Emerging digital micromirror device (dmd) applications. In *MOEMS display and imaging systems*, volume 4985, pages 14–25. SPIE, 2003.

[78] Jinyang Liang, Rudolph N Kohn Jr, Michael F Becker, and Daniel J Heinzen. 1.5% root-mean-square flat-intensity laser beam formed using a binary-amplitude spatial light modulator. *Applied optics*, 48(10):1955–1962, 2009.

[79] Li-Chung Ha, Logan W Clark, Colin V Parker, Brandon M Anderson, and Cheng Chin. Roton-maxon excitation spectrum of bose condensates in a shaken optical lattice. *Phys. Rev. Lett.*, 114(5):055301, 2015.

[80] Yifan Peng, Suyeon Choi, Jonghyun Kim, and Gordon Wetzstein. Speckle-free holography with partially coherent light sources and camera-in-the-loop calibration. *Science advances*, 7(46):eabg5040, 2021.

[81] Anand Ramanathan, Sérgio R Muniz, Kevin C Wright, Russell P Anderson, William D Phillips, Kristian Helmerson, and Gretchen K Campbell. Partial-transfer absorption imaging: A versatile technique for optimal imaging of ultracold gases. *Review of Scientific Instruments*, 83(8), 2012.

[82] Dallin S Durfee and Wolfgang Ketterle. Experimental studies of bose-einstein condensation. *Optics Express*, 2(8):299–313, 1998.

[83] OM Marago, SA Hopkins, J Arlt, E Hodby, G Hechenblaikner, and CJ Foot. Observation of the scissors mode and evidence for superfluidity of a trapped bose-einstein condensed gas. *Physical review letters*, 84(10):2056, 2000.

[84] L. Pitaevsiii and S. Stringari. *Bose-Einstein Condensation*. Clarendon Press, 2003.

[85] Alessio Recati, Francesca Zambelli, and Sandro Stringari. Overcritical rotation of a trapped bose-einstein condensate. *Physical Review Letters*, 86(3):377, 2001.

[86] Subhasis Sinha and Yvan Castin. Dynamic instability of a rotating bose-einstein condensate. *Physical Review Letters*, 87(19):190402, 2001.

[87] Katepalli R Sreenivasan, Kartik P Iyer, and Ashvin Vinodh. Asymmetry of velocity increments in turbulence. *Physical Review Research*, 4(4):L042002, 2022.

[88] Kartik P Iyer, Katepalli R Sreenivasan, and PK Yeung. Scaling exponents saturate in three-dimensional isotropic turbulence. *Physical Review Fluids*, 5(5):054605, 2020.

[89] Julien Salort, Benoît Chabaud, Emmanuel Lévêque, and P-E Roche. Energy cascade and the four-fifths law in superfluid turbulence. *Europhysics Letters*, 97(3):34006, 2012.

[90] AW Baggaley and CF Barenghi. Quantum turbulent velocity statistics and quasiclassical limit. *Physical Review E*, 84(6):067301, 2011.

[91] Ran Yang, Daniel W Apley, Jeremy Staum, and David Ruppert. Density deconvolution with additive measurement errors using quadratic programming. *Journal of Computational and Graphical Statistics*, 29(3):580–591, 2020.

[92] Martin Andersen, Joachim Dahl, and Lieven Vandenberghe. Cvxopt: Convex optimization. *Astrophysics Source Code Library*, pages ascl–2008, 2020.

[93] Ahmet Celikoglu and Ugur Tirnakli. Skewness and kurtosis analysis for non-gaussian distributions. *Physica A: Statistical Mechanics and its Applications*, 499:325–334, 2018.

[94] Carlos M Jarque and Anil K Bera. Efficient tests for normality, homoscedasticity and serial independence of regression residuals. *Economics letters*, 6(3):255–259, 1980.

[95] Michikazu Kobayashi and Makoto Tsubota. Kolmogorov spectrum of superfluid turbulence: Numerical analysis of the gross-pitaevskii equation with a small-scale dissipation. *Physical review letters*, 94(6):065302, 2005.

[96] J. R. Ensher, D. S. Jin, M. R. Matthews, C. E. Wieman, and E. A. Cornell. Bose-einstein condensation in a dilute gas: Measurement of energy and ground-state occupation. *Phys. Rev. Lett.*, 77:4984–4987, Dec 1996.

[97] Franco Dalfovo, Stefano Giorgini, Lev P. Pitaevskii, and Sandro Stringari. Theory of bose-einstein condensation in trapped gases. *Rev. Mod. Phys.*, 71(3):463–512, April 1999.

[98] V. F. Sears, E. C. Svensson, P. Martel, and A. D. B. Woods. Neutron-scattering determination of the momentum distribution and the condensate fraction in liquid ^{4}He. *Phys. Rev. Lett.*, 49:279–282, Jul 1982.

[99] V. L. Berezinskii. Destruction of long-range order in one-dimensional and two-dimensional systems possessing a continuous symmetry group. ii. quantum systems. *Sov. Phys. JETP*, 34:610–616, 1972.

[100] J. M. Kosterlitz and D. J. Thouless. Ordering, metastability and phase-transitions in 2 dimensional systems. *J. Phys. C*, 6:1181–1203, 1973.

[101] Anthony J Leggett. Can a solid be" superfluid"? *Phys. Rev. Lett.*, 25(22):1543, 1970.

[102] E. L. Andronikashvili. *Zh. Eksp. Teor. Fiz. 16, 780.*, 1946.

[103] G. B. Hess and W. M. Fairbank. Measurements of angular momentum in superfluid helium. *Phys. Rev. Lett.*, 19:216–218, Jul 1967.

[104] Massimo Boninsegni and Nikolay V. Prokof'ev. Colloquium: Supersolids: What and where are they? *Rev. Mod. Phys.*, 84:759–776, May 2012.

[105] L Tanzi, JG Maloberti, G Biagioni, A Fioretti, C Gabbanini, and G Modugno. Evidence of superfluidity in a dipolar supersolid from nonclassical rotational inertia. *Science*, 371(6534):1162–1165, 2021.

[106] Matthew A Norcia, Claudia Politi, Lauritz Klaus, Elena Poli, Maximilian Sohmen, Manfred J Mark, Russell N Bisset, Luis Santos, and Francesca Ferlaino. Two-dimensional supersolidity in a dipolar quantum gas. *Nature*, 596(7872):357–361, 2021.

[107] Fabian Böttcher, Jan-Niklas Schmidt, Matthias Wenzel, Jens Hertkorn, Mingyang Guo, Tim Langen, and Tilman Pfau. Transient supersolid properties in an array of dipolar quantum droplets. *Phys. Rev. X*, 9:011051, Mar 2019.

[108] M. P. A. Fisher, P. B. Weichman, G. Grinstein, and D. S. Fisher. Boson localization and the superfluid-insulator transition. *Phys. Rev. B*, 40:546–570, 1989.

[109] Markus Greiner, Olaf Mandel, Tilman Esslinger, Theodor W Hänsch, and Immanuel Bloch. Quantum phase transition from a superfluid to a mott insulator in a gas of ultracold atoms. *Nature*, 415(6867):39–44, 2002.

[110] Michael E Fisher, Michael N Barber, and David Jasnow. Helicity modulus, superfluidity, and scaling in isotropic systems. *Phys. Rev. A*, 8(2):1111, 1973.

[111] A. J. Leggett. On the superfluid fraction of an arbitrary many-body system at t=0. *Journal of Statistical Physics*, 93(3):927–941, 1998.

[112] Roger Corthan Clark and Graham Holbrook Derrick. *Mathematical Methods in Solid State and Superfluid Theory: Scottish Universities' Summer School*. Springer, 2013.

[113] Cord A Müller. Josephson relation for disordered superfluids. *Phys. Rev. A*, 91(2):023602, 2015.

[114] J. H. Huckans, I. B. Spielman, B. Laburthe Tolra, W. D. Phillips, and J. V. Porto. Quantum and classical dynamics of a bose-einstein condensate in a large-period optical lattice. *Phys. Rev. A*, 80(4):043609, 2009.

[115] Anand Ramanathan, Sérgio R Muniz, Kevin C Wright, Russell P Anderson, William D. Phillips, Kristian Helmerson, and Gretchen K Campbell. Partial-transfer absorption imaging: A versatile technique for optimal imaging of ultracold gases. *Review of Scientific Instruments*, 83(8):083119–083119–9, 2012.

[116] J. Steinhauer, R. Ozeri, N. Katz, and N. Davidson. Excitation spectrum of a bose-einstein condensate. *Phys. Rev. Lett.*, 88:120407, Mar 2002.

[117] D Guéry-Odelin and S Stringari. Scissors mode and superfluidity of a trapped bose-einstein condensed gas. *Phys. Rev. Lett.*, 83(22):4452, 1999.

[118] O. M. Maragò, S. A. Hopkins, J. Arlt, E. Hodby, G. Hechenblaikner, and C. J. Foot. Observation of the scissors mode and evidence for superfluidity of a trapped bose-einstein condensed gas. *Phys. Rev. Lett.*, 84(10):2056–2059, March 2000.

[119] G Chauveau, C Maury, F Rabec, C Heintze, G Brochier, S Nascimbene, J Dalibard, J Beugnon, SM Roccuzzo, and S Stringari. Superfluid fraction in an interacting spatially modulated bose-einstein condensate. *arXiv:2302.01776*, 2023.

[120] K. Jiménez-García and I. B. Spielman. *Annual review of cold atoms and molecules: Volume 2*, pages 145–191. World Scientific, 2013.

[121] A. Browaeys, H. Häffner, C. McKenzie, S. L. Rolston, K. Helmerson, and W. D. Phillips. Transport of atoms in a quantum conveyor belt. *Phys. Rev. A*, 72:053605, Nov 2005.

[122] Nigel R. Cooper and Zoran Hadzibabic. Measuring the superfluid fraction of an ultracold atomic gas. *Phys. Rev. Lett.*, 104(3):030401, January 2010.

[123] Dmitry Kobyakov, A Bezett, Emil Lundh, Mattias Marklund, and Vitaliy Bychkov. Turbulence in binary bose-einstein condensates generated by highly nonlinear rayleigh-taylor and kelvin-helmholtz instabilities. *Physical Review A*, 89(1):013631, 2014.

[124] Seth Musser, Davide Proment, Miguel Onorato, and William TM Irvine. Starting flow past an airfoil and its acquired lift in a superfluid. *Physical review letters*, 123(15):154502, 2019.

[125] M Krämer, L Pitaevskii, and S Stringari. Macroscopic dynamics of a trapped bose-einstein condensate in the presence of 1d and 2d optical lattices. *Phys. Rev. Lett.*, 88(18):180404, 2002.